For Uncle Ian

UNIVERSITY OF SOUTHAMPTON

A Numerical Study of Laminar to Turbulent Evolution and Free-Surface Interaction of a Vortex Ring

by

Philip John Archer

Thesis for consideration of PhD

School of Engineering Sciences
Aerodynamics and Flight Mechanics Group

June 2008

ABSTRACT

A numerical study of laminar to turbulent evolution and free-surface interaction of a vortex ring

by Philip John Archer

Direct numerical simulation was used to study various aspects of vortex ring evolution and interaction with a free surface. An investigation of a single unbounded vortex ring at various Reynolds numbers and core thicknesses showed qualitative differences between the evolution of thin- and thick-core rings, leading to a correction factor to the classical equation for the ring translational velocity. The obtained linear modal growth rates were compared with previous work, highlighting the role of the wake in triply periodic numerical simulations. The transition from a laminar to a turbulent ring is marked by the rearrangement of the outer core vorticity into a clearly defined secondary structure. The onset of the fully turbulent state is associated with shedding of the structure in a series of hairpin vortices. A Lagrangian particle analysis was performed to determine the ring entrainment and detrainment properties and to investigate the possibility of an axial flow being generated around the circumference of the core region prior to the onset of turbulence.

The orthogonal interaction of laminar, transitional and turbulent rings with an initially undesturbed free surface was investigated. At small depths, the expanding ring is unstable to the Crow instability but its dominant mode is predetermined by the prior development of the Widnall instability. The presence of opposite-signed vorticity, due to surface curvature, affects the ring dynamics at the surface. The interaction of a transitional ring modifies the surface displacements, reflecting the structure of the ring below. The secondary structure associated with a transitional ring reconnects to the surface in addition to the inner core. In the presence of the surface, the turbulent ring finds greater coherency of the core due to stretching and aligning of vorticity filaments. The addition of a planar surface wave field modified the ring interaction greatly due to the higher surface curvature and associated surface vorticity. The ring expands asymmetrically and even rebounds locally if sufficient opposite-signed vorticity is generated. The ring diffracts the surface wave field and the generation of secondary small-amplitude waves was noted.

Acknowledgements

Nothing worth having comes without hard work, determination and a little help from your friends and to this end I have many people to thank for their contribution to my work both directly and indirectly.

Thanks must first and foremost go to my supervisors Dr Gary Coleman and Dr Glyn Thomas, both of whom I have really enjoyed working with and without whom this thesis would contain 134 blank pages. The lessons that I have learned from them both, have been invaluable and have gone far past the confines of mere Fluid Dynamics text books. In particular I would like to thank Gary for his enthusiasm, knowledge, organisational skills, cheery anecdotes (especially the one about the monkey, without which I am sure this thesis would remain an unfinished symphony) and of course his mastery of the dark art of grammar! I would like to thank Glyn in particular for his expansive knowledge of physics and computers, his ability to pull me out a muddle when I was a bit lost and for finding time for me when a thousand and one things seemed to be going on.

Special thanks also goes to Dr Karim Shariff, who visited Southampton in the early days of my PhD and infected me with his enthusiasm for the field. Also special thanks go to my fellow Matlab supporter Dr John Redford for always being there to bounce ideas off, Chris Yorke for his comparative simulations, Robert Hornby at DSTL for his visits and P.O.A.L Davies for his video tapes of the secondary ring structure. I would also like to thank my old physics teachers Mrs Price and Mr Thomas for interesting me in the subject many years ago.

I would also like to thank my sponsors DSTL and EPSRC for their financial support and the UK Turbulence consortium for computational time on the HPCx system.

I don't think I would have made it through without surfing and music and to this end I give special thanks to all my surfing buddies who shared the love, of note, Rob Archer, Koen, Rob Amy, Mick Fanning, Matt, Gaz, Jed, Ollie, John, Bish

and Mike, Nick, Claire Baglin, Andy, Rich Murray, Alex, Ash, Claire O'Sullivan, Francesca, Rachel, Janan and all the new skool surfers that have the old skool spirit. Music softens even the savage beast and for this I must thank John, Koen and Rich for our sunset jam sessions, Sam Callear for her eclectic taste (and PhD chats), Sublime, Pepper, Smerins Anti Social Club, The Cat Empire, Xavier Rudd, Rise Against and the list could go on and on.

Working (very) part-time at the talking heads was a great way to break up three years of a PhD with some live music, friendly staff, lock-ins and locals and special thanks must go out to all the main players especially the Spanish contingent Maria and Christina, but also Nick, Joel, Mel, Sarah, Mark, Simon, Henty, Jo, Jess and Bob.

Special thanks also goes to Lizzie Phillips for seeing me through to the end of my PhD with fine dining, de-stressing massages, support and much much more.

A problem shared is a problem halved and with this in mind I would like to thank all my fellow PhD students and Post Docs and lecturers who made me feel like I was part of a team and that I was not going through it all alone, especially Max and all my office buddies through the years, but also the AFM football team and all those who turn up to practice week in week out.

Special thanks also to my 'old old' friends who always make me smile, Jim, Haz, Aatin, Remy, Nim, Cian, Adam, Shutty, Powrie, Hannah, Roz, Sarah, Josh, Dave, Wykes, Jez, Ed, Wan, Caz and M.

It is not possible to finish without thanking my family for all their considerable support: Mum, Dad, brothers Rob and Tom, sister Rosie, all the Masseys and attachments, all the Meads and Granny and Grandpa and the memories of Uncle Ian, little granny and Rory.

Although this PhD has often been difficult and stressful I've enjoyed it immensely.

Contents

List of Figures

List of Tables

Nomenclature

Symbol	Description
a	amplitude
a_1	distance from core centre to maximum tangential velocity
a_e	speed-effective measure of the core radius
$\mathbf{A}$	far-field velocity potential
A, B, C	constants
b	core separation distance
c	celerity
d	depth
$\tilde{d}$	trim length
$\widehat{d}$	dimensionless cut-off length (proportional to core diameter)
D	diameter
e	strain rate
E	energy
F	force
F_K	flux of kinetic energy
g	gravitational acceleration
h	surface height
H	sum of convective and diffusive terms
I	unit tensor
I_f	interpolation factor
I_R	radius limit before interpolation
II	second invariant of the velocity gradient tensor
k	wavenumber
K	kinetic energy
$\widehat{k}$	dimensionless wavenumber
L_x, L_y, L_z	box lengths

Symbol	Description
l	length
m	azimuthal flow type
M^s	stable manifold
M^u	unstable manifold
n	modal number
N_x, N_y, N_z	number of grid cells in the x, y and z-directions
$\mathbf{n}$	unit normal vector
p	pressure
P	impulse
q	tangential velocity
Q	momentum flux
r	radial coordinate
R	ring radius
R_θ	ring radius measure weighted by ω_θ
R_Ω	ring radius measure weighted by enstrophy
$\widehat{R}$	distance from the ring centreline to the peak core vorticity
S	sloping surface area
t	time
t_e	evolving time
t^*	sampling initiation time
u, v, w	Cartesian velocity components
u_r, u_θ, u_z	cylindrical velocity components
u^*	provisional velocity
U	ring propagational velocity
$\widetilde{w}$	velocity induced by periodic image rings
W	inflow velocity
x, y, z	Cartesian coordinates

Greek Symbols

Symbol	Description
α	growth rate
β	slenderness ratio measure ($= a_1/R$)
δ	core radius
δ_θ	integral measure of core radius
δ_{ij}	Kronecker delta
ϵ	slenderness ratio ($= \delta/R$)
ϵ_θ	slenderness ratio ($= \delta_\theta/R_\theta$)
ϵ_K	dissipation
ϕ	scalar field
γ	radial growth rate
κ	radius of curvature
λ	wavelength
ν	kinematic viscosity
θ	azimuthal coordinate
ρ	density
σ	over-relaxation parameter
ς	perturbation amplitude
τ	shear stress
ω	vorticity
$\|\omega\|$	magnitude of vorticity
$\omega_{x,y,z}$	Cartesian components of vorticity
$\omega_{r,\theta,z}$	cylindrical components of vorticity
ξ	distance between periodic image rings
ψ	stream function
Δt	time step
$\Delta x, y, z$	grid size in x, y and z-directions
Γ	circulation
Ω	enstrophy

Subscripts

Symbol	Description
$\{\}_0$	initial condition
$\{\}_b$	block
$\{\}_D$	diameter
$\{\}_p$	processor
$\{\}_P$	piston
$\{\}_{max}$	maximum value
$\{\}_{WT}$	relating to the theory of Widnall & Tsai (1977)
$\{\}_{Sha}$	relating to the theory of Shariff *et al.* (1994)
$\{\}_{Sha}$	relating to the experiments of Dazin *et al.* (2006*a*)
$\{\}_S$	quantity value at the surface
$\{\}_{i,j,k,l,m,n}$	indices for Cartesian tensor notation

Subscripts

Symbol	Description
$\{\}^c$	corrected value
$\{\}^{i,j,k,l,m,n}$	indices for Cartesian tensor notation

Abbreviations

Symbol	Description
DNS	Direct Numerical Simulation
PIV	Particle Image Velocimetry
Re	Reynolds number
Fr	Froude number
We	Webber number
2D	two-dimensional
FTLE	finite-time Lyapunov exponent
LCS	Lagrangian coherent structures
RB-SOR	successive-over-relaxation
RAM	Random Access Memory
CFL	Courant-Friedrichs-Lewy number

Symbols

Symbol	Description
∇	Gradient operator
$\bigtriangledown.$	Divergence operator
$\nabla\times$	Curl operator
∞	infinity

Chapter 1

Introduction

Vortices and vortex filaments have been the fascination of engineers and physicists for more than a century. Their importance is due not only to their abundance in nature but also through their presence in engineering flows and turbulence. Organised vortical structures in the form of loops, hairpins, rings and lines have been recognised in turbulent flow in both numerical and experimental studies. Understanding the stability of these structures, their fundamental properties, and how they propagate and interact, is crucial to aid our understanding of turbulence.

In this report we focus on a single vortex ring, both its instability and breakdown as well as its interaction with a free surface. This is because it embodies a prototypical turbulent flow and its interaction with a deformable free surface has practical implications. Considering engineering and biological flows, vortex rings are principally generated by three methods. The method most commonly employed in laboratory experiments is to accelerate fluid through an orifice or pipe into an ambient fluid. The force required to accelerate the fluid through the orifice is usually delivered by a piston or a loud speaker (see Maxworthy (1972), Glezer & Coles (1990)(piston), Naitoh *et al.* (2002) and Dziedic & Leutheusser (1996)(loudspeaker) to name but a few. Upon entering the ambient fluid the accelerated fluid forms a vortex sheet which rolls up into a vortex ring a short distance downstream of the generator exit. The same method of vortex ring generation is also found in nature for jellyfish, which utilise momentum exchange by pulsing out vortex rings to propel themselves (Dabiri *et al.*, 2005).

A second method commonly employed to investigate vortex ring motion is to allow droplets of fluid to free fall onto a pool of fluid; see for example Rodriguez & Mesler (1988), Peck & Sigurdson (1994) and Peck & Sigurdson (1995). The impact of the

droplet on the surface of the pool causes a vortex sheet to form in the pool which rolls up to form a vortex ring, which then propagates down away from the surface.

A third method of vortex ring generation is brought about by the development of the Crow instability on a pair of line vorticies (Crow, 1970). The elliptical long wave Crow instability (see § 2.2.1) causes a stationary sinusoidal wave to grow on the vortex pair. As the waves grow, localised regions of the line vorticies are brought into close proximity to one another. Eventually both line vorticies disconnect locally and reconnect with the opposing line vortex to form a series of vortex rings. Line vorticies are produced by lifting surfaces of aircraft but also, more relevant to this study, by submarines (Lloyd & Hanson, 1985). It has been shown that such vortex pairs reconnect to form rings in the Direct Numerical Simulations (DNS) of Garten *et al.* (2001) whilst traveling through an ambient stratified flow. It has also been shown that turbulent wakes will develope into vortex ring-like structures far downstream of their production in either a stratified or non stratified flow (Gourlay *et al.*, 2001).

The decay of vortex pairs in a stratified ambient fluid is of relevance to submarine wake development. If a submarine or other submersible vehicle undergoes a diving manoeuvre, negative lift is generated by the aerofoil sections causing a pair of line vorticies to propagate through the stratified ocean toward the surface. The pair of line vorticies are subject to the Crow instability and thus are likely to create a series of vortex rings with a long-lived structure. The vortex rings will then continue to propagate towards the surface under their own self induced velocity, with the possibility of reaching the surface if the ocean stratification and turbulence levels allow. The region directly below the surface of the sea is an unstratified mixed layer consisting of varying turbulent intensities and scales largely dependent upon atmospheric conditions. It is here where we pick up the vortex ring story and simulate numerically its free-surface interaction. The interaction not only covers interesting vortex ring dynamics but will cause disturbance to surface waves (Cerda & Lund, 1993) and temperature distribution (Smith *et al.*, 2001) which may allow for tracing by remote sensing apparatus. The condition of the vortex ring when it reaches the free surface is largely unknown, although one can postulate that it will be either laminar, transitional, or in some state of turbulence. We thus first aim to understand the temporal developement of the unbounded vortex ring before the free-surface interaction is studied.

This thesis contains the results from a numerical investigation into a single unbounded vortex ring and the interaction with a bounding surface. It is based on

results from DNS of these two cases and organised into the following chapters. In Chapter 2, we review the relevant literature, focusing on general vortex ring characteristics, instability, and surface interactions. Drawing on the lessons learnt from previous investigations we then present our project aims in Chapter 3. The mathematical and implementational framework of our numerical codes are layed out in Chapter 4. Chapter 5 discusses various initialisation techniques to provide starting conditions for our simulations. The following three chapters present the results of vortex ring motion within an unbounded (Chapter 6) and bounded domain, where the bounding surface is initially undisturbed (Chapter 7) and wavy (Chapter 8). We summarise our findings and their importance in Chapter 9 and finally make some suggestions for future work in Chapter 10.

Chapter 2

Literature review

We first define the vortex ring and assess the current understanding of its fundamental properties, how it develops with time, and how it interacts with a free surface.

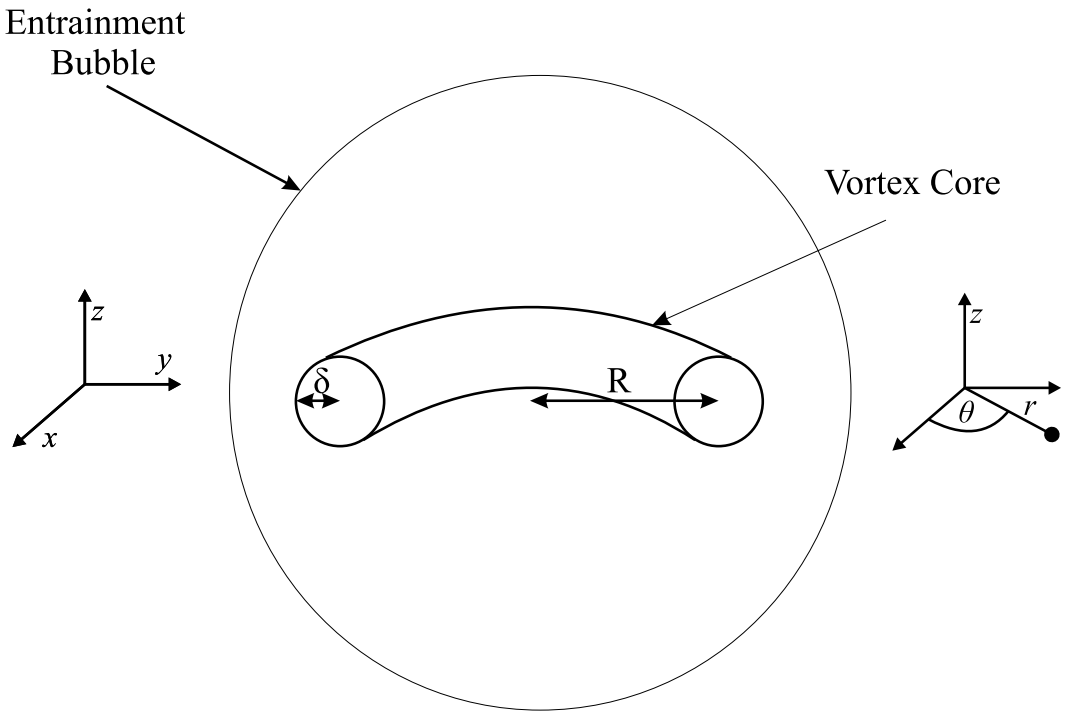

FIGURE 2.1: Schematic diagram of a vortex ring, sliced through its centre.

2.1 Vortex ring characteristics

In a co-moving reference frame, a laminar vortex ring can be regarded as a toroidal vortex core of radius, δ, which is surrounded by a co-moving mass of rotating fluid, known as the entrainment bubble (see figure 2.1). The ring has a radius R, usually defined by experimentalists as the distance from the ring centreline to the core centre. The slenderness ratio ϵ is defined as the ratio of core to ring radii, δ/R. The core region has a distribution of azimuthal vorticity ω_θ that in the limit of $\epsilon \to 0$ tends to a Gaussian profile. The circulation Γ and the impulse P of the ring are defined as

$$\Gamma = \int \omega_\theta \mathrm{d}r\mathrm{d}z \quad \text{and} \quad P = \pi \int r^2 \omega_\theta \mathrm{d}r\mathrm{d}z. \tag{2.1}$$

The classical expression for the self-induced propagation velocity U of a laminar vortex ring is

$$U = \frac{\Gamma}{4\pi R}\left(\ln\left(\frac{8R}{\delta}\right) + C\right), \tag{2.2}$$

where the constant C is a function of the shape of the vorticity distribution across the core region. For a uniform vorticity distribution $C = -1/4$ (Lamb, 1932). Saffman (1970) showed that if a Gaussian distribution of vorticity was specified, to first order of ϵ, $C = -0.558$. A comparison of the theoretical prediction of propagation velocity for a Gaussian core ring was made with the experimental rings of Dziedic & Leutheusser (1996). They concluded that $C = -0.558$ could be used for both laminar and turbulent rings, however due to the lack of flow data (a hot-wire probe was used to measure ring velocities), quantities such as Γ and R had to be modeled.

Recently experimentalists have used Particle Image Velocimetry (PIV) techniques to measure Γ, R and the core vorticity distribution directly from the flowfield. Dabiri & Gharib (2004), Cater *et al.* (2004) and Dazin *et al.* (2006*a*) all show mildly non-Gaussian core profiles, with a sharper drop in vorticity toward the outer edge of the core compared to the ring centre-line. Cater *et al.* (2004) also note that the distribution of vorticity, and indeed subsequent ring dynamics and instability growth rate are highly effected by the precise method of ring generation. They found that a piston/cylinder ring generator produced a secondary ring at the piston head with the same sign vorticity as the primary ring but of

lower circulation. The two rings were found to quickly merge, consistent with the leapfrogging experiments of Lim (1997) with the resultant combined ring being of higher circulation and velocity but more unstable. The generation of the secondary piston ring could be prevented by ceasing the motion of the piston a distance of two orifice diameters from the orifice exit.

We adopt a Reynolds number based on ring circulation unless otherwise stated, with $\mathrm{Re} = \Gamma_0/\nu$, where the subscript '0' relates to the initial conditions and ν is kinematic viscosity. A number of different definitions of Reynolds numbers also exist in the literature: piston Reynolds number, $\mathrm{Re}_P = U_P D_e/\nu$, where U_p is the average piston speed and D_e is the exit diameter; Reynolds number based on ring diameter, $\mathrm{Re}_D = UD/\nu$, where D is the ring diameter; and a 'Saffman' Reynolds number, $\mathrm{Re}_S = ea_1^2/\nu$, where e is the strain rate experienced by the core, an estimate of which is given by Saffman (1978) as

$$e = \frac{3\Gamma}{16\pi R^2}\left[\ln\left(\frac{8R}{a_e}\right) - \frac{17}{12}\right], \tag{2.3}$$

and a_1 and a_e are measures of the core radius, defined below. A comprehensive method for estimating corresponding piston parameters given Reynolds number and core measures is documented by Shariff *et al.* (1994).

In previous numerical and experimental work the core thickness has usually been specified by either the speed-effective core thickness, a_e, or the distance from the core centre to the point of maximum tangential velocity, a_1. The speed-effective core radius is the projected core radius of an equivalent vortex ring propagating at identical speed with a uniform distribution of vorticity. For a Gaussian core $a_e = 1.3607\delta$ and $a_1 = 1.1214\delta$ (Shariff *et al.*, 1994).

Vortex rings can be collated into two groups; laminar and the turbulent (see figure 2.2). The structure and stability of laminar rings was investigated experimentally by Maxworthy (1972) and Widnall & Sullivan (1973). They found that for the Reynolds numbers tested, the rings began in a laminar state, characterised by smooth concentric streamlines and a relatively weak wake (left side of figure 2.2(b)). Maxworthy showed that below a Reynolds number Re_D of 600 a stable laminar ring was formed and propagated under the influence of viscosity ν, which diffused the core until the ring eventually became completely dissipated into the ambient fluid. The core diffusion for laminar rings with a Gaussian distribution of vorticity is given by Saffman (1970) as

$$\delta^2 = \delta_0^2 + 4\nu t. \tag{2.4}$$

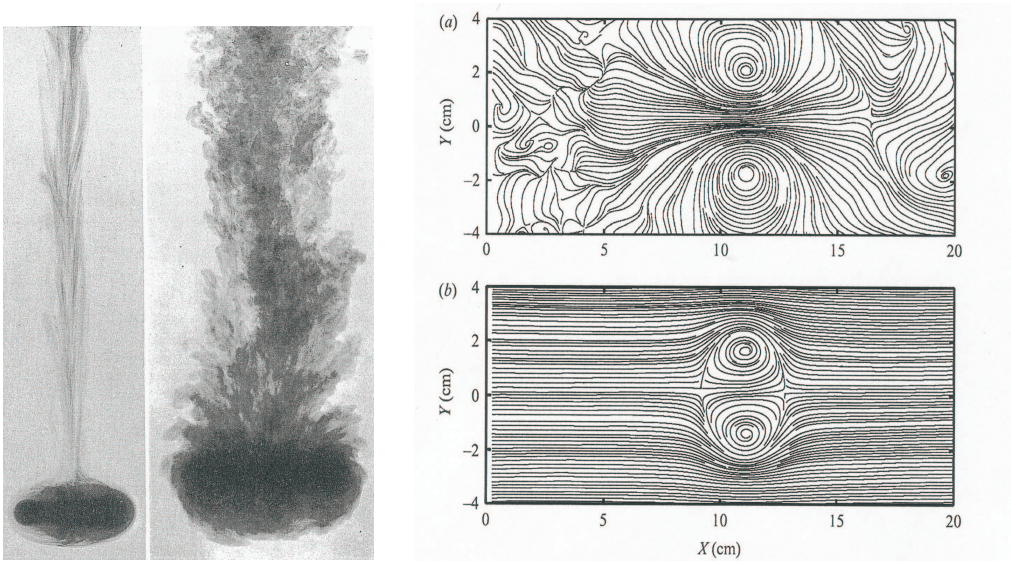

(a) (b)

FIGURE 2.2: Vortex ring behaviour. (a) Dye visualisation of laminar and turbulent vortex rings, from Glezer & Coles (1990). (b) Streamlines for a laminar vortex ring, from Dabiri & Gharib (2004); laboratory frame (upper), Lagrangian frame (lower).

At $\mathrm{Re}_D > 1000$ stationary azimuthal instability waves develope on the core region which eventually break down, signaling transition from a laminar to a turbulent state. A turbulent ring, visualised on the right side of 2.2(a), is characterised by a chaotic vortical bubble structure and a core region of relatively high vorticity. The turbulent ring ejects a considerably larger amount of circulation into its wake than the laminar ring does. Experimental investigations into the turbulent vortex rings have been performed either by evolving a laminar ring through the natural instability to a turbulent state (Maxworthy, 1974) (Wiegand & Gharib, 1994) or by creating the vortex ring at sufficiently high Re_P (Glezer & Coles, 1990). The experiments of Wiegand & Gharib (1994) tracked vortex rings at an initial Reynolds number (based on circulation) of 7500 through the laminar regime into the turbulent state via the natural azimuthal instability. Their results also showed that during transition and throughout the turbulent regime vortical structures were generated in the periphery of the ring. The vortex core however was maintained as a definite coherent structure. The ring then relaminarised when the loss of ring circulation had decreased the Reynolds number to 2300. Vortex shedding into the wake was attributed to the peripheral vortical structures. The loss of organised structure lead to a staircase like decay in circulation and velocity, the velocity lagging the circulation by a small phase shift. Recently Glezer & Coles (1990)

also noted the vortical structures, inferring that they are likely to be vortex tubes of alternating sign wrapped around the main core, with their presence influencing the local entrainment and detrainment dynamics.

The process of detrainment results in wake formation, visualised in figure 2.2(a), and is caused by diffusion of vorticity across the bubble interface into the ambient fluid which is left behind the vortex bubble in a wake. Under certain conditions it has been shown that the circulation shed by a vortex ring into its wake can be a significant proportion. The inviscid numerical study of Nitsche (2001) considered the roll up of a spherical vortex sheet into a vortex ring which shed 30% of its initial vorticity into a wake. The wake subsequently rolled up into a secondary vortex ring whose subsequent circulation loss caused the roll up of a tertiary ring in its wake, with the process repeating itself in a self-similar manner. This self-similar wake roll up has not been seen in previous experiments.

A key property of a vortex ring is that it is surrounded by a co-moving mass of rotational fluid, known as the entrainment bubble. The bubble surface separates rotational fluid associated with the ring from the irrotational fluid in which it moves. The vortex ring dynamics and physical parameters (bubble size, ring radius and core radius) are not constant and their rate of change is defined by the balance between entrainment and detrainment. Maxworthy (1972) proposed a model for diffusive entrainment, whereby the thin layer of irrotational fluid by the entrainment bubble is contaminated by vorticity diffusing away from the ring. A proportion of this fluid is then entrained through the rear of the bubble into the vortex ring and the remainder ejected into the wake. Power-law ratios were given for the decay of both the overall ring velocity and circulation, but these power laws were found not to be universal by Dabiri & Gharib (2004), who considered two distinct rings propagating into both an ambient fluid and an oncoming flow of uniform velocity. They were, however, able to confirm part of Maxworthy's entrainment model, showing that vorticity is diffused across the vortex bubble and is present in the wake. Note that the existence of the wake implies that the vortex ring loses both circulation and impulse, although in a control volume containing both the ring and the (entire) wake, the total impulse is invariant.

The ability of a ring to directly entrain fluid has also been studied by Glezer & Coles (1990), who used an assumed streamfunction in similarity coordinates to predict net entrainment of particles for the case of a fully turbulent ring. The concept of fluid entrainment and detrainment has been further refined by the application of stable and unstable manifolds of dynamical systems theory to the Lagrangian

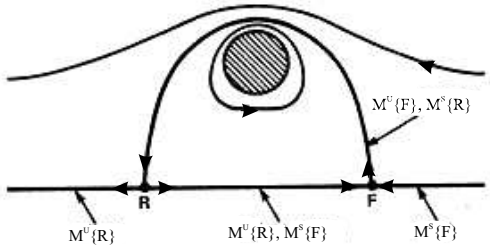

FIGURE 2.3: Sketch of streamlines and manifolds for a steadily translating vortex ring, taken from Shariff *et al.* (2006). The hatched region depicts the vortex core.

surface of the vortex ring entrainment boundary. Let us consider the case of an inviscid ring propagating at a steady velocity with constant ring and core radii to illustrate the ideas behind the theory (figure 2.3). In a co-moving reference frame the velocity field is time independent, hence for this case the streamlines represent particle trajectories. The vortex ring possesses two stagnation points or *hyperbolic* fixed points, F and R, fore and aft of the ring respectively, where hyperbolic refers to a point in the flow through which two or more streamlines can be drawn. Stable manifolds M^s are defined as the particle trajectories that asymptote toward a hyperbolic fixed point as time goes to infinity. Unstable manifolds M^u are defined as particle trajectories that asymptote toward a hyperbolic fixed point as time goes to negative infinity. The stable and unstable manifolds of F and R are displayed in figure 2.3. For the case of the steadily translating vortex ring the stable and unstable manifolds coexist forming a boundary between the rotational inner fluid and the irrotational flow that passes round it. Connections such as the trajectory $\vec{FR}$ that join two stagnation points are known as *heteroclinic* trajectories. Introducing a perturbation that is periodic in time has been shown to break such a connection, splitting apart the stable and unstable manifolds of the front and rear stagnation points. The result is that the manifolds meander progressively around each other as they approach the opposing stagnation point. The intersections between the manifolds are called *lobes* (see figure 2.4(a)).

Shariff *et al.* (2006) produced a numerical simulation to do exactly this by simulating a vortex ring with an elliptical core region that rotated around the core centre inducing a periodic oscillation on the ring velocity. Time periodic systems such as this can be viewed via a *Poincaré* map. In a Poincaré map time is introduced as an extra direction in physical space. It is created by taking a particle a small radial distance away from a hyperbolic fixed point and mapping it forward one period. The position of the particle before and after the time period defines

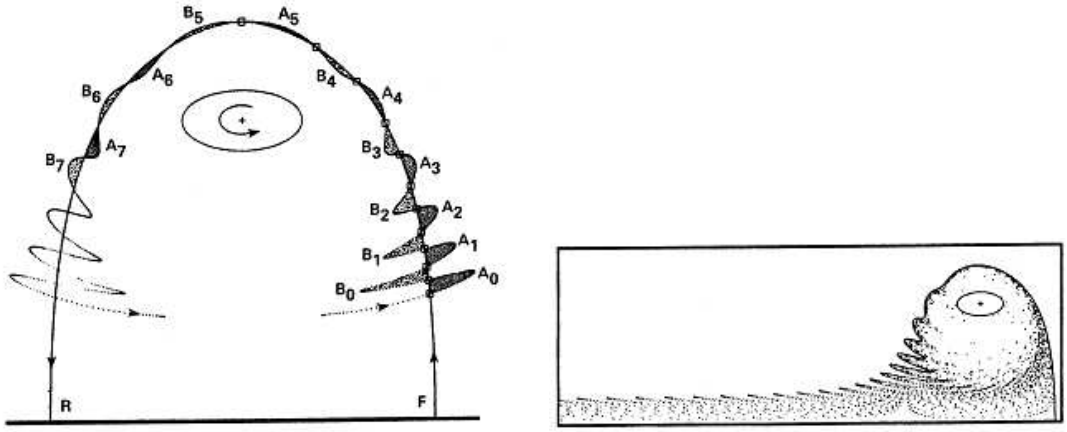

(a) (b)

FIGURE 2.4: Abridged portions of the stable and unstable manifolds showing fluid entrainment and detrainment over a number of time periods, taken from Shariff *et al.* (2006).

the two end points of a segment. The manifold is then built by iterating a large number of neighbouring particles forward by one period. The neighbouring particles converge to the manifold from both sides so the fact that the first particle may not be exactly on the manifold is irrelevant. The unstable manifold of the rear stagnation point is then obtained by symmetry since if time were reversed the vortex would rotate counter clockwise and the rear stagnation point would become the front stagnation point. A section of the resulting Poincaré map is shown in figure 2.4(a). One must not interpret the figure as a snap shot in time but as a history of the movement of the lobes A_0 and B_0. In one time period the lobe A_0 moves to A_1 and B_0 moves to B_1, then in the next time period from A_1 to A_2 and B_1 moves to B_2 and so on. Each manifold (the dividing line between the lobe and the exterior flow) is *invariant*, hence flow cannot cross the boundary and flow inside the lobe remains inside the lobe. If we consider the final destination of A_0 on the Poinicaré map it lies inside the vortex ring bubble and so is considered to be a lobe of entrainment. The lobe B_0 on the other hand consisted of fluid inside the bubble but by the rear stagnation point is outside the bubble and is thus a lobe of detrainment. The unstable manifold of the front stagnation point moves to infinity downstream of the vortex ring in a spiky pattern, as shown in figure 2.4(b). A similar spiky pattern is seen in typical dye visualisations of turbulent vortex rings, causing Shariff *et al.* (2006) to postulate that lobe dynamics may play an important role in explaining entrainment and detrainment of turbulent vortex rings.

Shadden *et al.* (2006) also used dynamical systems analysis to determine the fluid transport characteristics of laminar piston-generated vortex rings. The piston-generated vortex rings present a slightly more complicated problem as the velocity field is aperiodic, thus a Poinicaré map cannot be constructed to investigate the lobe dynamics. The aim of their analysis was to find *finite-time hyperbolic manifolds* which are analogous to the stable and unstable manifold of the periodic analysis above. These finite-time hyperbolic manifolds are called *Lagrangian Coherent Structures* or LCS for short. They are found by constructing finite-time Lyapunov exponent (FTLE) fields. The FTLE field measures the maximum exponential divergence, at a given time and space within the flow, of nearby trajectories over a finite time interval. For the vortex ring the maximum divergence of particle paths occurs at the entrainment bubble boundary, since it separates fluid that moves with the ring from the outside flow that will increasingly separate with time downstream of the ring. The FTLE field thus picks out the LCS corresponding to the Lagrangian entrainment boundary. By calculating the FTLE field forwards in time the LCS corresponding to the stable manifold is uncovered and by integrating backwards in time the LCS corresponding to the unstable manifold is revealed. By over plotting the LCS for the front and rear stagnation points it was found that lobe dynamics were present, causing entrainment and detrainment patterns similar to those found by Shariff *et al.* (2006). The development of lobes on the laminar ring requires a perturbation to be present on the dynamics of the vortex ring. Such a perturbation was found by Kumar *et al.* (1995), who produced vortex rings over a range of Reynolds numbers. By taking measurements at close time intervals they found that the propagation velocity of the vortex ring oscillated in time. The velocity oscillations cause oscillation of the position of the front and rear stagnation point, in a Lagrangian view, which would be sufficient to create the lobe dynamics.

Shariff *et al.* (2006) compared the growth rate of the cross-sectional area of the Lagrangian surface with previous Eulerian streamline analysis of Dabiri & Gharib (2004). They found that the growth trends were very similar, corresponding to net entrainment for both analysis techniques. A net entrainment suggests that the entrainment bubble must grow with time and conversely a net detrainment demands a reduction in the entrainment bubble mass. The growth of the bubble is likely to manifest itself in a change in the ring dynamics. Maxworthy (1977) measured the radial growth rate, γ, of turbulent rings in a stationary ambient fluid reporting a range of values, with fatter turbulent cores producing higher radial growth rates. Rusakov (2001) showed experimentally that a concurrent flow

increased γ for turbulent rings and that a counter flow decreased γ, which take a negative value (radial contraction) if the retarding flow is of sufficient strength.

2.2 Vortex ring instability

2.2.1 Linear Phase

The discovery of the presence of unstable azimuthal waves on a vortex ring is attributed to Krutzsch (1939) in a paper overlooked by the scientific community until a similar instability was discovered by Crow (1970) in aircraft wakes. Maxworthy (1972) performed a series of experiments to investigate the structure and stability of laminar and turbulent vortex rings, discovering that the initially toroidal core was distorted into a sinusoidal wave, of wavenumber five, around the ring circumference. Subsequent experiments by the same author (Maxworthy, 1974, 1977) showed that the growth and subsequent wave breaking marked the transition from a laminar to a turbulent vortex ring. The waves were stationary and grew in a conical plane at an angle of 45° to the axis of ring propagation; Shariff *et al.* (1994) later corrected the angle to 42°. Crow (1970) had already witnessed a similar long-wavelength instability that grew at a 48° angle to the horizontal for a pair of trailing vortices generated by aircraft. Through a linear stability analysis he showed that the vortices are unstable to both symmetric and antisymmetric waves. The symmetric waves are present in the form of either short- or long-waves, depending on the external perturbations on the vortices. The most amplified wavelength, the growth rate and the plane in which the perturbation grew were found to depend on the ratio $\widehat{d}/\widehat{k}$ of dimensionless cut-off length (proportional to core diameter) to dimensionless wavenumber. With the approximation of a constant vorticity profile in the core region, Crow showed that

$$\widehat{d}/\widehat{k} = 0.3210D/b, \tag{2.5}$$

where D is the core diameter and b is the separation distance between the vortex cores. For an elliptically loaded wing, $\widehat{d}/\widehat{k} = 0.063$, the most unstable wavelength $\lambda_{max} = 8.6b$, the growth rate $\alpha = 1.21(2\pi b^2/\Gamma_0)$[1], and the fixed plane in which perturbations develop was 48° to horizontal, for the long-wave symmetric mode. According to the linear theory, both short-wave symmetric and antisymmetric modes

[1] where $(2\pi b^2/\Gamma_0)$ is the time taken for the vortices to move down a distance b under their own induction

are also unstable; however since atmospheric turbulence preferentially drives the long-wave symmetric mode, it is the only instability seen in the atmosphere (Crow, 1970).

Widnall & Sullivan (1973) investigated the ring instability experimentally, showing that the number of waves observed was a function of ϵ. Inspired by the experimental evidence, Widnall *et al.* (1974) considered both a rectilinear vortex and a vortex ring subjected to a strain field and showed that the azimuthal disturbances are associated with bending waves. They went on to show that the second radial mode of bending was unstable if the waves had no self-induced rotational velocity and that the instability grew along a conical surface at 45° to the axis of ring-propagation. Further analysis by Moore & Saffman (1975) and Tsai & Widnall (1976) supported this idea and also gave equations for the growth rate of a perturbation. Widnall & Tsai (1977) then rigorously proved that a ring with uniform core vorticity distribution was unstable, with analysis up to $O(\epsilon^2)$. They found that the critical wavenumber values, k, for the non-rotating second and third radial modes are $k = 2.51$ and 4.35 respectively. The lower-order second radial mode is more unstable and hence grows preferentially. Shariff *et al.* (1994) also showed that, for a more realistic Gaussian profile, the critical wavenumber for the second and third radial modes become $k = 2.26$ and 3.96 respectively. Their revisions were inspired by Saffman (1978), who noted that the number of waves on the ring was dependent on the vorticity profile, with his estimates of wave number showing good agreement to experimental observations. The ring circumference can only support an integer number of waves n, where n is estimated as $n = kR/a_1$ (Shariff *et al.*, 1994). The theoretical analysis of Widnall & Tsai (1977) also yielded an expression for the inviscid growth rate α_{WT} of the instability,

$$\alpha_{WT} = \frac{\Gamma}{4\pi R^2}\left[(0.856\ln\left(\frac{8R}{a}\right) - 0.9102)^2 - 0.4535\right]^{1/2}, \tag{2.6}$$

where a is some measure of the core radius[2].

The ring or *Widnall* instability was investigated numerically by Shariff *et al.* (1994), who solved the three-dimensional Navier-Stokes equations for a single ring, simulated in a triply periodic domain. The simulations support the theory presented in Widnall & Tsai (1977), showing an integer number of waves growing around the ring excited by the lower radial bending modes. A viscous correction

[2]Note the last term is corrected from its original form in Widnall & Tsai (1977) to correct a typo as documented in Shariff *et al.* (1994)

to α_{WT} was also developed for the inviscid growth rate, given by

$$\alpha_{Sha}(\beta) = \alpha_{WT}(\beta)\left(1 - \frac{\alpha_1(\beta)}{\mathrm{Re}_S}\right), \tag{2.7}$$

where $\beta = a_1/R$ and α_1 is a constant of value between 19.7 and 22.8. This correction has recently been called into question by the experiments of Dazin *et al.* (2006*a*), who suggest that it is too small. They cite amongst other things, that the Shariff *et al.* prediction is only valid for purely Gaussian cores. However, this takes no account of the fact that in the DNS the initially Gaussian distribution quickly equilibrates to a skewed pseudo-Gaussian profile similar to that found in the experiments.

The viscous-correction growth rate α_{Sha} is consistent with the behaviour of the two-dimensional elliptical streamline flow investigated by Landman & Saffman (1987), where a low wavelength cut off was deduced for the two-dimensional viscous growth rate given by

$$\alpha_{2D} = \frac{9}{16}e - \nu k^2 \tag{2.8}$$

where k is again the wavenumber. Equation (2.8) shows that in the presence of viscosity the low wavenumber modes grow faster than the higher wavenumber modes(lower wavelength modes). Landman & Saffman were following work by Pierrehumbert (1986) and Bayly (1986) who showed that an unbounded uniform two dimensional vortex with elliptic streamlines in a straining field was linearly unstable to three-dimensional perturbations.

The similarity between the instability growth of vortex rings, vortex lines and two-dimensional vortices in strained fields became apparent, and it is now acknowledged that all are due to the elliptical instability. A review of the elliptical instability is given by Kerswell (2002).

2.2.2 Nonlinear phase

The preferential instability growth of a small number of azimuthal modes n, which typifies the linear phase, is followed by a nonlinear phase, during which the dominant azimuthal modes interact with one another. The nonlinear phase has been investigated experimentally by Dazin *et al.* (2006*a*,*b*), who used PIV and novel

flow visualisations. The study confirmed the earlier numerical results by Shariff *et al.* (1994), showing that the nonlinear phase is heralded by the exponential growth of higher-order harmonics of the most unstable linear modes. The nonlinear interaction of competing modes also causes rapid growth of the $n = 1$ mode, which corresponds to asymmetry in wave growth around the ring circumference. This is followed by the rapid growth of the $n = 0$ mode in the azimuthal energy component, corresponding to a mean 'axial' or 'swirling' flow, accompanied by the development of vortical structures on the (outer) periphery of the ring, leading to ejection of vorticity into the wake. (Following Maxworthy, the term 'axial' will be used to indicate the circumferential axis of the vortex core.) The notion of an axial flow is supported by the experiments of Naitoh *et al.* (2002) and the numerical study of Shariff *et al.* (1994), the latter showing that it takes the form of opposing streams, necessary to conserve angular momentum. Subsequently, vortical structures grew on the interior of the ring before the breakdown to turbulence, causing the authors to infer that the peripheral vortical structures are wrapped progressively around the core in a series of loops; this is consistent with the vorticity tubes observed in the experiments of Schneider (1980) during the latter stages of transition.

Recently Bergdorf, Koumoutsakos & Leonard (2007) numerically investigated the vortical structures, suggesting that they originate from locally stretched regions of the deformed core. Their ring parameters were chosen to match the experiments of Wiegand & Gharib (1994), which tracked vortex rings at an initial Reynolds number (based on ring circulation Γ) of 7500 through the laminar into the turbulent regime. Qualitative agreement was found between the two studies, which showed that the turbulent ring sheds vortical structure into the wake in a series of hairpin vortices leading to the 'staircase-like' decay in time of circulation and velocity mentioned above.

The nonlinear modal growth ends in saturation of the azimuthal modes and the breakdown of the stationary azimuthal wave. Lack of spatial resolution prevented Shariff *et al.* (1994) from investigating further than the early nonlinear phase, however Maxworthy (1977) inferred from smoke visualisations that immediately prior to breakdown the stationary waves begin to rotate out of the conical 45°-plane. The waves then break preferentially around the azimuth, leading to a net ('swirling') flow in the form of a solitary wave propagating along the circumferential axis of the turbulent ring. No experimental or numerical work has yet been able to confirm or deny convincingly Maxworthy's inferences. A net swirling flow in the core region was induced by the experiments of Naitoh *et al.* (2002), however

this was only in cases where the ring had been created through an orifice with a wavy exit cross section.

2.3 Surface Interactions

The key parameters associated with the interactions of a vortex ring with a free surface are Froude number, $\mathrm{Fr} = \Gamma/\sqrt{gR^3}$ (where g is the gravitational acceleration), angle of propagation toward the surface, ϕ, the presence of surface contaminants, Reynolds number (as defined earlier) and to a lesser extent the Weber number, We. The ring-surface interactions can be grouped into the following sections: normal interaction of a vortex ring; oblique interaction of a vortex ring; and vortex-pair interaction.

2.3.1 Normal interaction of vortex rings

Experimental work by Song *et al.* (1992) outlines the key stages of the interaction between a vortex ring and a 'clean' free surface. Here 'clean' describes a surface which has been treated to remove surfactants. They focused on two of their experimental rings to explain the interaction, which we label S1 and S2. S1 featured a Froude number $\mathrm{Fr} = 0.287$ and Reynolds number $\mathrm{Re} = 15100$, while S2 had $\mathrm{Fr} = 0.988$ and $\mathrm{Re} = 64700$. Measurements were initiated when the vortex ring was well formed and a distance of $2.5R_0$ below the free surface.

As both rings propagate from a depth of $2.5R_0$ to approximately $1R_0$ below the surface the radius and velocity remain approximately constant. The interaction then differed for the two cases. At depths of less than $1R_0$, the rings begin to interact more strongly with their virtual image above the surface. For Case S1 the ring approaches the surface as an axisymmetric toroid. As it moves closer to the surface its radius expands until it reaches a depth the order of the core thickness. At this point the ring propagates parallel to the surface, expanding radially at constant depth. When the core is at a small depth, its dynamics and strain field are dominated by its image vortex above the surface. The ring locally approximates a pair of line vortices and the core is susceptible to the Crow instability. Subsequently at a ring radius of $3.2R_0$, a wavy core structure developes [3] around the azimuth of the ring and continues to grow until the ring reconnects with the

[3] referred to by Song *et al.* (1992) as 'three dimensionality'.

free surface in a series of U-shaped vortex filaments. This is consistent with the experiments of Lim & Nickels (1992), who investigated the head-on collision between two vortex rings. In their experiments the free surface and virtual image is replaced by a real ring, which reconnects with the original ring in a similar fashion. Lim & Nickels (1992) also found that in some of their experiments a short-wavelength instability occurred, sometimes coexisting but not 'interacting noticeably' with the long-wavelength instability. The short-wavelength instability is also predicted by the linear stability analysis of Crow (1970), discussed above, and its presence is likely to be due to the absence of background turbulence. Recall that Crow (1970) proposed that background turbulence favours the long-wave symmetric mode above the short-wave symmetric and antisymmetric modes.

For Case S2, the observed 'three dimensionality' occurred far earlier, almost as soon as the ring started to expand radially and at a depth of $0.5R_0$. The radial expansion that followed occurred at a far slower rate and a greater depth than for Case S1. Song *et al.* (1992) attributed this to the size of the respective cores, however it could also be due to the generation of opposite signed vorticity. Longuet-Higgins (1998) showed that in any viscous flow, as tangential stress goes to zero, the vorticity parallel to a surface is given by

$$\omega_s = -2\kappa_s q, \tag{2.9}$$

where κ_s is the radius of curvature (negative for a convex surface) and q is the tangential velocity. (See Lundgren & Koumoutsakos (1999) for a discussion of vorticity generation at a free surface). The surface curvature is far greater for Case S2, thus one would expect the generation of significantly more opposite signed surface vorticity. Case S2 also reconnected to the surface but in a slightly different fashion, as described below.

The free surface response depends heavily on the Froude number. The approach of the rings toward the surface induced a bulge directly above the ring. As the rings expanded in a plane parallel to the surface, the bulge dropped and a depression formed just outboard of the ring. For the high Fr Case S2, the deformation to the surface was approximately 20 times larger; furthermore, the collapse of the initial bulge generated outwardly radiating surface waves. The surface depression propagated outward, following the expansion of the rings and striations were seen to form on the surface perpendicular to the depression (and hence vortex core). For Case S2, small circular indentions formed around the depression corresponding to regions of reconnection. Both rings eventually reconnected with the surface

and consequentially the depression disappeared, replaced by a number of small circular indentions corresponding to attachment zones of the U-shaped vortex filaments. The reconnection of vorticity filaments to the surface generated outwardly radiating short waves. The waves were significantly larger for Case S2.

Song *et al.* (1992) also performed a numerical study with the ring parameters matching their experimental rings. They used a vortex/boundary integral method, where the flow was assumed axisymmetric, inviscid, incompressible, and irrotational except for the ring. The numerical study matched the experimental results well at early times but the differences increased as the ring developed three dimensional structure (earlier for the high Froude number case). A similar numerical method was employed by Ye & Chu (1997), whose simulations featured a wide range of Fr and We. They found that at sufficiently high Fr and We it was possible for the ring to become trapped inside the surface bulge. As for the numerical study of Song *et al.* (1992), no surface reconnection occurred, however this is not unexpected as reconnection is a viscous process (Ashurst & Meiron, 1987). Wu *et al.* (1995) performed an axisymmetric investigation by direct numerical simulation of the Navier-Stokes equations and found that high Fr cases, with Fr = 7.07, generate significant surface vorticity, causing rebounding of the primary vortex ring. For a moderate Froude number, 0.707, the results of Wu *et al.* (1995) mirrored that of Song *et al.* (1992) except once more for the absence of surface reconnection. The absence of surface reconnection is due to the assumption of axisymmetry which prevents the Crow instability from appearing.

An alternative experimental study can be found in Chu *et al.* (1993), with surface interactions investigated at lower Re, from 900 to 2350, and in the presence of surfactants. Free-surface experiments were conducted, at Froude numbers around 0.45, and a solid wall, with similarities and contrasts commented upon. Qualitatively both rings behaved in the same way. As the ring approaches both barriers there is a period of vortex stretching. The induced field of the ring then forms opposite signed vorticity at the barrier, which rolls up to form a secondary ring outboard of the primary ring. Both the secondary and primary rings rebound, before propagating again toward the respective barrier producing a relatively weak tertiary vortex ring. The major differences between the solid wall and free surface interactions were the amount of opposite signed vorticity generated, with the free surface producing around a fifth of that of the solid wall, and the radial increase of the ring, $2.5R_0$ for the free surface and $1.8R_0$ for the solid wall. For the free surface interaction the opposite signed vorticity is generated from a mixture of sources. Surface curvature generates vorticity, as described above, however the

presence of surfactants causes surface tension gradients which drive a surface flow that tends to diminish the gradients (Sarpkaya, 1996). Comparing the free surface deformation to that observed by Song *et al.* (1992), both studies report a significant surface bulge on the ring approach and the generation of outwardly radiating surface waves as the ring begins to expand radially. However a large difference appears as the rings expand as the Chu *et al.* (1993) ring rebounds and the Song *et al.* (1992) ring continues to expand until reconnection. This can be attributed to the presence of surfactants in the experiments of Chu *et al.* (1993).

In contrast to these findings, Boyovintrev *et al.* (1997), in a paper scant on detail, observed that for weaker vortex rings, with $\mathrm{Re}_D < 5000$, the rings collapsed in the vicinity of the surface. For 5000 $<\mathrm{Re}_D <$ 10,000, the ring was reflected and traveled downwards away from the surface. At $\mathrm{Re}_D >$ 13,000, the ring collapsed on impact with the surface. The collapse at higher Re was said to be 'explosive' with fluid ejected above the surface. The paper makes no comment on the degree of surface contamination or the value of the Froude number. Comparing these results with Song *et al.* (1992) the differences can be attributed to the unknown concentration of surfactants. The paper is less focused on surface interaction and more focused on showing that the turbulent vortex rings could travel up to 35 ring diameters vertically towards the surface.

2.3.2 Oblique vortex-ring interaction with a free surface

The process of disconnection and reconnection of vortex filaments has been investigated by propagating rings at oblique angles toward a free surface. In the experiments of Gharib & Wiegand (1996) and subsequent numerical calculations by Zhang *et al.* (1999), laminar vortex rings were propagated at varying angles toward an undisturbed free surface with Fr = 0.47. As the ring approaches the surface, the surface develops a curved bulge above the core region. The associated surface curvature creates opposite signed vorticity (Longuet-Higgins, 1998) downstream of the approaching ring. If the surface was not purposefly cleaned, the secondary vorticity had significantly higher circulation, due to the upwelling of clean fluid in the surface bulge, which creates high concentrations of surfactants on either side. The resultant surface strain causes a subsurface boundary layer which adds to the secondary vorticity due to curvature. Zhang *et al.* (1999) showed that the secondary vorticity stretches the rear section of the core which then reconnects to the surface to form a single U-shaped vorticity filament (figure 2.5d). Under the action of its self-induced flow the legs of the U-loop move apart and the lower re-

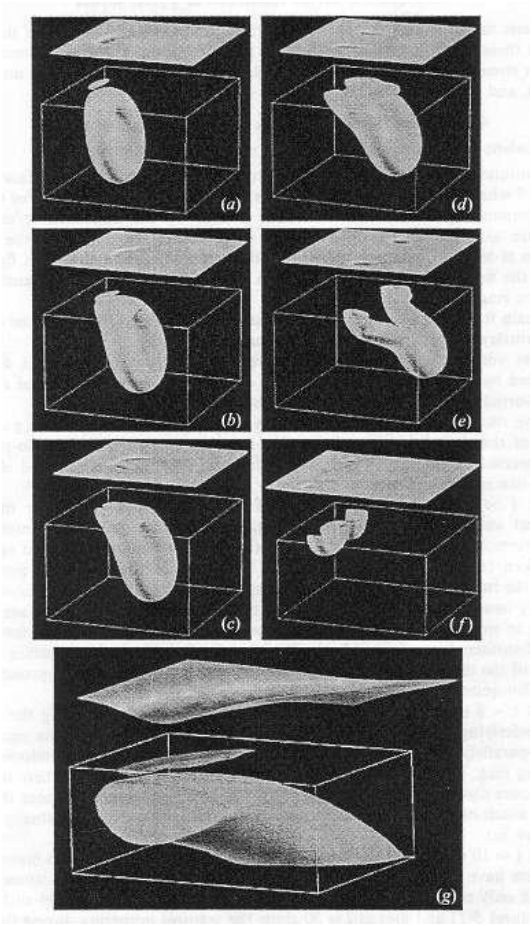

FIGURE 2.5: The oblique interaction of a vortex ring with a free surface, taken from Zhang *et al.* (1999).

gion moves toward the surface. It too reconnects with the surface resulting in two separate smaller U-shaped vorticity filaments in a process known as 'bifurcation' (figure 2.5f). Bifurcation did not occur for the contaminated surface.

The generation of vorticity flux is explored in the numerical calculations of Zhang *et al.* (1999). In their discussion they focus on two sectors of the flow: the viscous layer, a region very close to the surface caused by the boundary condition of zero tangential stress; and a blockage layer stretching further down into the fluid resulting from the kinematic boundary condition. They showed that inside the blockage layer, the surface-normal component of vorticity ω_z increases due to vortex stretching and vortex turning from the surface-parallel component ω_y. The normal component ω_z is then transported across the viscous layer to the surface by diffusion, which increases the vorticity in the plane of the surface.

Prior to Zhang *et al.* (1999), Ohring & Lugt (1996) also performed a DNS of the oblique ring interaction with a free surface. The simulations explored rings with

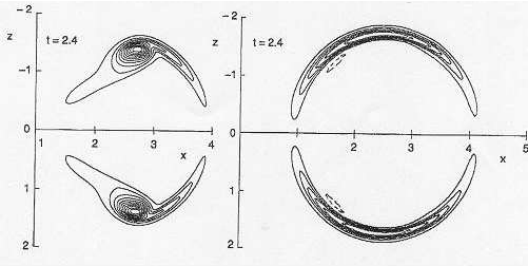

FIGURE 2.6: Surface normal vorticity for a reconnected obliquely propagating vortex ring, taken from Ohring & Lugt (1996).

propagation angles of 20° to 45° to the surface and Re = 100 → 200, including the effect of surface tension. Higher surface tension dampens the surface response while changing the angle of attack modifies the vorticity profile of the reconnection zones (figure 2.6).

The oblique interaction was investigated experimentally at different stages of the ring lifetime, laminar, transitional and turbulent by Wiegand & Gharib (1995) and Wiegand (1996). Laminar rings were generated with initial Reynolds numbers Re = 7500 and allowed to develop the Widnall instability prior to their contact with the surface. The transitional rings produced a new type of reconnection known as *trifurcation*, involving three reconnected vorticity filaments. The ring initially reconnects into a single U-shaped vorticity filament, followed by bifurcation into two U-hoops as the lower section of the ring was propelled toward the surface. Unlike the laminar interaction, however, the bifurcated vorticity filaments simultaneously became turbulent. Associated with the transition process is the ejection of elongated vorticity structures into the wake (likely to be in the form of hairpins; see above (Bergdorf *et al.*, 2007)), which spontaneously form a third reconnected site at the surface. The interaction produced normal waves which propagate downstream of the ring, whereas upstream, the radiated waves bear resemblance to waves emitted by two point sources.

The interaction of the fully turbulent ring is characterised by the same bifurcation process, but with the superposition of small-scale activity causing multiple reconnections. The circulation measurements for the turbulent case showed that only 70% of the intial circulation is present in the reconnected hoops. By tracking the small-scale interactions it was found that the surface interaction involved pairing

and splitting of reconneted vorticity filaments. Pairing of opposite-signed vorticity filaments caused cancellation of circulation.

2.3.3 Interaction between a pair of vortex lines and a free surface

Hirsa & Willmarth (1994) investigated the normal interaction of a pair of vortex lines with a free surface and Willert & Gharib (1997) investigated the same process with a sinusoidally deformed pair of vortex lines. The interaction was found to be strongly dependent upon the degree of surface contamination. For clean surfaces a series of circular depressions formed, located above the underlying sinusoidal peaks of the vortex pair. PIV measurements showed that the depressions corresponded to surface reconnection of the vortex pair, which form a series of U-shaped vorticity filaments. The paper concluded that it is necessary for the flow kinematics to force the core region into close contact with the surface in order for connection to occur. If the vortex pair is separated by a distance greater than twice the amplitude of the induced instability wave, no surface reconnection was observed. When surface reconnection was achieved, it was shown that the increased circulation on the surface plane is directly balanced by the loss of surface-normal vorticity from the vortex pair. In the presence of a contaminated surface layer the upwelling of clean fluid caused a surface bulge with high concentrations of contaminants either side, known as a *Reynolds ridge*. The shear forces produced, and the associated subsurface boundary layer generated, a large quantity of opposite-signed vorticity which prevent surface reconnection and cause rebounding of the vortex pair. This was also shown by Hirsa & Willmarth (1994) for an initially undisturbed vortex pair.

2.3.4 Surface Waves

No previous numerical or experimental studies could be found on the vortex ring interaction with a wavy free surface. However, a number of related studies, such as Umeki & Lund (1997), Coste *et al.* (1999), Coste & Lund (1999) and Vivanco & Melo (2004), have considered the wave interaction with a vertical vortex. Umeki & Lund (1997) constructed a differential equation governing the behaviour of sound waves during their interaction with a steady vortex flow at low Mach number and small wavelength. Solutions corresponding to spiral waves were found and shown

to rotate in the opposite direction to the vortex. Appealing to the analogies between the interaction and the Aharonov-Bohn effect (Berry *et al.*, 1980) and between water waves and sound waves, they showed that the equation also permitted the existence of dislocated surface waves over shallow water. Both scattered spiral waves and dislocations were also shown by the analytical solutions of Coste *et al.* (1999), Coste & Lund (1999) and then experimentally by Vivanco & Melo (2004). The degree to which the waves were scattered and whether dislocations occurred were found to be a function of the vortex circulation, and the wave amplitude, frequency and wavelength. A critical case was also found in which the wave remained continuous (no dislocations), but a spiral scatter was introduced downstream of the vortex. Vivanco & Melo (2004) considered a vortex dipole and found that if the dipole is located perpendicular to the wave field the wavefront exhibits a phase shift proportional to the total dipole circulation. The symmetry of the oncoming wave is maintained and the wave phase is restored as the wave moves away from the vortex. It was also shown that arranging the vortex dipole parallel to the wave front has negligible impact on the wave train. The impact of a progressive surface wave field on an underlying weakly turbulent flow was investigated numerically by Teixeira & Belcher (2002) using a rapid-distortion model. The waves modified the turbulent Reynolds stresses and tilted vertical vorticity into the horizontal plane through Stokes drift, forming elongated streamwise vortices which subsequently dominate the flow.

Chapter 3

Project aims

The motivation behind this study is to investigate the temporal development of a vortex ring as it propagates from an arbitrary depth toward and interacts with a free surface. The structure of the ring as it approaches the surface is dependent upon how it has developed during its ascent. The first task is therefore to investigate the temporal development of a ring in an unbounded fluid. Once this has been quantified and understood, the knowledge gained can be used to investigate the free-surface interaction for different characteristic structures. Finally, we seek to address how the presence of a surface wavefield modifies the interaction. The different topics of research are explored further below.

3.1 Investigation of vortex ring evolution from a laminar to a turbulent state

3.1.1 Laminar phase

The first task facing the laminar investigation is to determine the best way of initialising a coherent ring which exhibits the intended characteristics. The key questions that the laminar investigation seeks to answer are how the vortex ring geometry, velocity, integral parameters (impulse and circulation), and entrainment/detrainment characteristics develop with time. By investigating the effects of slenderness ratio and Reynolds number we also hope to address the differences in the linear growth rates recorded by Shariff *et al.* (1994) and Dazin *et al.* (2006*a*).

3.1.2 Transitional phase

Prior to the onset of turbulence the ring undergoes a period of nonlinear wave growth and structural change, which we refer to as the transitional phase. The recent studies of Dazin *et al.* (2006*a*,*b*) and Bergdorf *et al.* (2007) point to the development of secondary peripheral structure which we intend to investigate and determine its role on the transition to turbulence. We also seek to address the experimental observations of instability wave rotation and axial flow prior to the onset of turbulence. Finally we aim to investigate the effect of the transitional phase on the entrainment/detrainment characteristics.

3.1.3 Turbulent phase

In the interest of meeting our other objectives, we confine our investigation to the early turbulent ring regime, considering the development of the structure and geometry of the ring.

3.2 Interaction of a vortex ring with a free surface

We limit the investigation to the normal ring interaction as it encompasses the physics discussed in the literature review, featuring vortex stretching, instability growth, reconnection and wave generation. The normal interaction is also arguably the most challenging, which is probably why at present no DNS exists of the non-axisymmetric problem. As the study relates to the ring-surface interaction in the ocean (e.g. generated by large submersible vehicles), we simplify the problem by ignoring the effects of surfactants and surface tension.

3.2.1 Interaction of a vortex ring with an undisturbed free surface

The aim of our undisturbed surface investigation is to investigate the phenomena and questions posed by the experiments of Song *et al.* (1992). Their numerical study, and subsequent investigations by Ye & Chu (1997) and Wu *et al.* (1995), have not successfully addressed the interaction past the initial vortex climb toward

the surface and early expansion. This is due to their assumptions of axisymmetry and inviscid flow which prohibit the ring from becoming unstable and developing the Widnall or Crow instabilities and reconnecting with the surface. We are well placed, with our DNS codes, to ignore these assumptions and model more closely the full interaction. Our main objective is therefore to develop the ring instability in the presence of the surface. This will enable us to investigate with a greater degree of realism both the ring and surface behaviour. Moreover, it will allow us to focus on the two instability mechanisms (Crow and Widnall) and examine how they interact. It is hoped that through knowledge of the unstable ring behaviour at the surface, we may be able to improve understanding of why the high-Fr cases behaved differently to the low-Fr cases in the experiments of Song *et al.* (1992). In particular, we are interested in why the high Fr case expands at greater depth, why reconnection zones are generated around the depression before the ring core reconnects in a series of U-shaped vortex filaments, and why both rings form surface striations. The oblique interaction of rings at different stages of their life cycle was shown by Wiegand & Gharib (1995) and Wiegand (1996) to modify the process dramatically. It is therefore also our aim to simulate the normal interaction of both transitional and turbulent rings, which to our knowledge has not be addressed in previous experimental or computational studies.

3.2.2 Interaction of a laminar vortex ring with a surface wave field

The final task is to investigate the ring interaction with a planar surface wave field of given wavelength and amplitude. The literature review suggests three main possible outcomes. If the wave energy is small compared to that of the ring, it is likely that the motion of the surface waves will be strongly affected, with the possibility of scattering and perhaps even dislocation. However if the wave energy is large compared to that of the ring, the ring motion could be affected, causing periodic stretching in phase with the wave motion as found for a turbulent flow by Teixeira & Belcher (2002). A third possibility also exists, whereby the ring and waves are of similar strength and affect each other in a strongly coupled nonlinear fashion. As no previous examples could be found in the literature for this case, we shall begin by addressing very basic questions. The strategy will be to vary the surface and wave parameters to assess their effect on the ring/planar wave interaction and to highlight its main features.

Chapter 4

Numerical codes

Two numerical codes have been used to simulate respectively the evolution of the vortex ring and its surface interaction, which we label the *fixed-boundary code* and the *free-surface code*. In discussing the numerical codes we start by laying out the governing equations and spatial and temporal discretisation, common to both codes, before discussing each in more detail.

4.1 Governing Equation

Both codes seek solutions to the incompressible Navier-Stokes equation for the fluid velocity $u_i = (u_1, u_2, u_3) = (u, v, w)$ given in the usual Cartesian tensor notation by

$$\frac{\partial u_i}{\partial t} + u_j \frac{\partial u_i}{\partial x_j} = -\frac{1}{\rho}\frac{\partial p}{\partial x_i} + \nu \frac{\partial^2 u_i}{\partial x_j \partial x_j} + F_i, \tag{4.1}$$

for a Cartesian coordinate system $x_i = (x_1, x_2, x_3) = (x, y, z)$, where the density ρ and the kinematic viscosity ν are constants, the fluid has pressure p and F_i denotes the contribution of external body forces. Conservation of mass is also enforced by

$$\frac{\partial u_i}{\partial x_i} = 0. \tag{4.2}$$

4.1.1 Spatial and temporal discretization

The Navier-Stokes equations are discretized on a staggered grid with spatial gradients evaluated using a second-order central differencing scheme.

The solution is advanced in time with the projection method based on a second-order explicit Adams-Bashforth scheme. The Adams-Bashforth scheme can be formulated as

$$u_i^{n+1} = u_i^n + \frac{3\Delta t}{2} H_i^n - \frac{\Delta t}{2} H_i^{n-1} + \frac{\Delta t}{2} \frac{\partial p_i^{n-1}}{\partial x_i} - \frac{3\Delta t}{2} \frac{\partial p^n}{\partial x_i}, \tag{4.3}$$

where the superscript n denotes the current time step, Δt is the duration of the time step and the quantity H_i contains the convective and diffusive terms in (4.1), with

$$H_i = \nu \frac{\partial^2 u_i}{\partial x_j \partial x_j} - u_j \frac{\partial u_i}{\partial x_j}. \tag{4.4}$$

The projection method entails first evaluating a provisional velocity u_i^* which comprises the first four terms on the right hand side of (4.3), hence

$$u_i^* = u_i^n + \frac{3\Delta t}{2} H_i^n - \frac{\Delta t}{2} H_i^{n-1} + \frac{\Delta t}{2} \frac{\partial p^{n-1}}{\partial x_i}. \tag{4.5}$$

Substituting u_i^* into (4.3) leaves

$$u_i^{n+1} = u_i^* - \frac{3\Delta t}{2} \frac{\partial p^n}{\partial x_i}. \tag{4.6}$$

By enforcing continuity at the next $(n+1)$ time step, we are left with the Poisson equation for pressure

$$\frac{\partial^2 p^n}{\partial x_i \partial x_i} = \frac{2}{3\Delta t} \frac{\partial u_i^*}{\partial x_i}. \tag{4.7}$$

p^n is then found by solving (4.7) and the updated velocity computed by (4.6). The two codes use different methods to solve (4.7) which are described below along with the two codes strengths and weaknesses with respect to the vortex ring investigation.

4.2 Fixed-boundary code

The fixed-boundary code, CGLES, has been written in C/C++ and has been parallelised using MPI (Message-Passing Interface) libraries, giving it the capability of running efficiently on a large numbers of processors. It has been used previously to investigate flow over complex geometry with both LES (Large Eddy Simulation) and DNS (Direct Numerical Simulation) techniques; see for example Thomas & Williams (1999), Yao *et al.* (2001), Coceal *et al.* (2007).

The code splits the computational domain into an arbitrary collection of N_b blocks which are then mapped onto N_p ($\leq N_b$) processors. Each block contains its own portion of the domain plus an overlap region of one layer of grid points beyond the block boundary. As the flow data is updated within a block the overlap region of adjacent blocks is updated through message passing. The code solves (4.7) through use of an efficient parallel multi-grid technique (see below for an explanation of the technique). The algorithm uses a sequence of grids constructed by binary subdivision within each block. Each grid has its own overlap region which is updated through message passing between grids at the same subdivision. A red-black successive-over-relaxation (RB-SOR)[1] scheme is used to solve (4.7) on the bottom grid. It is necessary for the red-black colouring to be consistent across adjacent blocks, which is ensured by requiring that the length of any closed path be an even number of grid points; this is enforced by preventing the last level of subdivision if necessary. Testing has shown that the time spent by the code solving the Poisson equation on the bottom grid is very small in comparison to the subsequent projection and restriction operations provided that the top grid allows for sufficient factoring (Thomas & Williams, 1997).

4.2.1 Outline of the numerical algorithm

1) Sweep domain to collect the convective and diffusive terms, which are summed to produce H_i^n (4.4) at the current time step, using standard second-order central differencing for the spatial gradients.

2) Project velocity u^* using the Adams Bashforth algorithm (4.5) with H_i^n and H_i^{n-1} and $(\partial p/\partial x_i)^{n-1}$ stored from the previous time step.

3) Create the source term for the Poisson equation (4.7).

[1] see Chapter 19 of Press *et al.* (2003) for an explanation of the RB-SOR scheme.

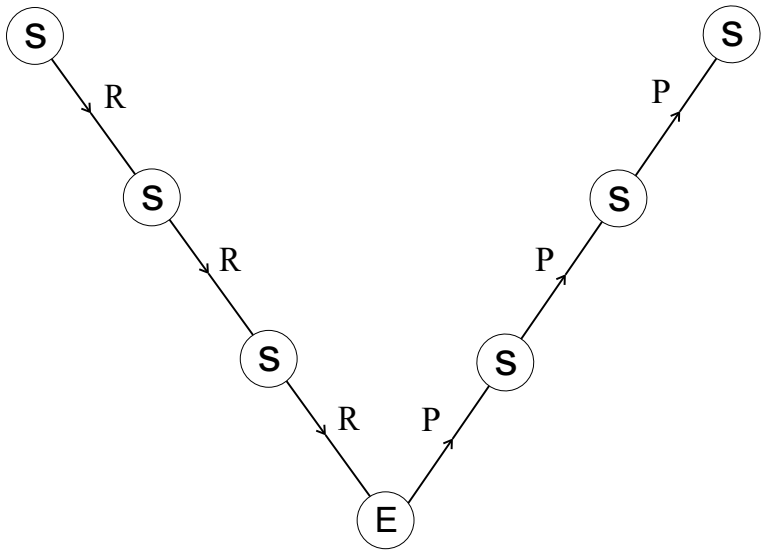

FIGURE 4.1: Structure of one multigrid V-cycle. 'S' denotes a smoothing procedure, 'E' denotes solving for the exact solution on the bottom grid, 'R' denotes a restriction procedure and 'P' denotes a prolongation procedure.

4) Solve the Poisson equation (4.7) to give p^n using a parallel multigrid technique. The procedure conducts a series of V-cycles until the pressure error is below a given tolerance, following the method layed out in Chapter 19 Press *et al.* (2003). The structure of the V-cycle is shown in figure 4.1 and the main steps of the multigrid technique are listed below:

- Perform two Gauss-Seidel iterations to smooth the solution on the top grid.
- Calculate the current residual and then use a 'restriction' operator (see below) to transfer the residual to a coarser grid which has half the grid points in all three directions.
- Continue to smooth the solution (through two Gauss-Siedel iterations) and restrict the residual to progressively coarser grids until the grid is small enough that performing a RB-SOR iteration scheme is more efficient than further restrictions.
- Perform RB-SOR iterations on this 'bottom' grid to reduce the residual below a given tolerance.
- Interpolate the corrected field to a grid with double the grid points in each direction through use of a 'prolongation' operator (see below).
- Continue to smooth the solution (through two Gauss-Siedel iterations) and

interpolate the pressure field onto progressively finer grids until we have returned to the initial grid and perform two final Gauss-Seidel iterations.

The restriction and prolongation operators transfer the residual to lower and higher grids respectively. The cell on the unknown grid is generated by a combination of the surrounding cells on the known grid. The factor to which each surrounding cell contributes to the unknown cell is specified by the operator; see Chapter 19 Press *et al.* (2003) for a discussion of operators.

4) Use the gradient of the pressure field and the projected velocity to give u_i^{n+1} (4.6).

4.2.2 Closing remarks

The parallelisation of the code makes it a powerful tool due its speed. Computer time on the HPCx high performance parallel computing system, has been provided by the funding bodies (DSTL and EPSRC) and the UK Turbulence Consortium. The code is thus ideal for simulating the vortex ring through its natural lifetime from laminar to turbulence, fulfilling part I of the project. The code can also be used to simulate the case of a vortex ring interacting with a free surface of very low Froude number and deflections. This case can be approximated by imposing free-slip boundary conditions at the extents of the axis of ring propagation.

4.3 Free-surface code

The free-surface code, FRECCLES, is written in Fortran 77 and solves the Navier-Stokes equations (4.1) on a single processor. The pressure problem (4.7) is solved with a RB-SOR iterative technique. Consequentially, it performs significantly slower than the parallel fixed-boundary code. However, the code encorparates a deformable surface on one of its boundaries. The free-surface boundary conditions are imposed on the upper extent of the z-axis with a free-slip condition imposed on the bottom of the domain. The flow moves under the influence of gravity g which is added to (4.1) as the force term $F_i = -g\delta_{i3}$, where δ_{ij} is the Kronecker delta.

4.3.1 Free-surface boundary conditions

A restriction is placed on surface height h, such that the maximum slope cannot exceed the aspect ratio of the grid cells,

$$|\partial h/\partial x| \leq \Delta z/\Delta x, \quad |\partial h/\partial y| \leq \Delta z/\Delta y, \tag{4.8}$$

where Δx, Δy and Δz are the dimensions of the grid cell. A kinematic boundary condition is imposed on the free surface, stating that the rate of change of elevation is proportional to the flux of fluid over the surface,

$$\partial h/\partial t = (\mathbf{u} \bullet \mathbf{n}) \sqrt{S}, \tag{4.9}$$

where S is the ratio of the the sloping surface area to the vertical projection of the surface area,

$$S = 1 + (\partial h/\partial x)^2 + (\partial h/\partial y)^2 , \tag{4.10}$$

and $\mathbf{n}$ denotes the surface unit normal vector,

$$\mathbf{n} = (-\partial h/\partial x, -\partial h/\partial y, 1) \sqrt{S^{-1}}. \tag{4.11}$$

A dynamic free-surface boundary condition is also imposed which states that the total normal stress (including the viscous component) and tangential stress must be zero,

$$\mathbf{n} \bullet (\tau - p\mathbf{I}) = 0, \tag{4.12}$$

where $\mathbf{I}$ denotes the unit tensor. The dynamic boundary condition leads to a Dirichlet condition for the pressure equation (4.7) as at the surface $z = h(x, y, t)$, $p(x, y, h) = p_s$ equals the normal viscous stress component and any externally applied pressure field. By imposing impermeable free-slip conditions on the domain bed we enforce $w = 0$ at $z = 0$ for all time, thus $\partial w/\partial t = 0$, hence the boundary conditions for (4.7) in the vertical direction z are

$$p = p_s(x,y,t) \quad \text{on } z = h(x,y,t), \tag{4.13}$$

$$\frac{\partial p}{\partial z} = u_3^* \quad \text{on } z = 0. \tag{4.14}$$

A further simplification is made by setting u_3^* to zero in the bottom layer of cells. This is equivalent to applying a constraining force which prevents acceleration in the cells. This simplifies the boundary condition (4.14) to

$$\frac{\partial p}{\partial z} = 0 \quad \text{on } z = 0, \tag{4.15}$$

but does not affect pressure field. Periodic boundary conditions are applied in the lateral x and y directions.

The free surface elevation $h(x,y,t)$ is updated using the split merge technique which is outlined in Appendix A.

4.3.2 Outline of the numerical algorithm

1) Sum the convection and diffusion terms to give the current value of H_i^n (4.4) in the surface cells, i.e. the top two layers of cells below the surface.

2) Add contributions of external body forces such as gravity.

3) Calculate H_i^n in the remaining domain.

4) Calculate projected velocity u_i^* for the *interior cells* (entire domain bar the top two layers of *surface cells*) using the Adams Bashforth scheme and history terms H_i^{n-1} and $\partial p_i^{n-1}/\partial x_i$ stored from the previous time step.

5) Project $(u_i^*)_{surf}$ in the same way.

6) Solve the Poisson equation (4.7) for p^n. The main steps are outlined below, in which we make a distinction between the surface cells that occupy the uppermost two planes below the surface and the interior cells which comprise the rest of the sub-surface cells:

- Calculate and store the source terms for all the interior cells with standard second-order finite differences.

- Store the coefficients for the standard-finite difference stencil factored by the over-relaxation parameter σ for an interior fluid cell.
- Calculate and store the modified finite-difference stencil for the surface cells.
- Calculate the source terms for the interior and surface cells.
- Iterate (4.7) with the RB-SOR routine, sweeping the x-y planes of cells vertically in two stages. In the first stage the interior cells which do not intersect with the free surface are subjected to full iteration. The second stage sweeps the surface layer of cells and conducts one full iteration. Note each full iteration step involves two sweeps, the first sweep updating the red cells and the second the black cells using the updated red cell values.
- The iterations cease after the error in the pressure field falls below a defined tolerance.

7) Update the velocity field u_i^{n+1} for the new time step by (4.6).

8) Use the split-merge technique to reassign the surface cells.

The maximum surface deformation constraint means that the surface code cannot model wave breaking, thus the Froude number must be low enough to prevent excessive surface deformation. The code can be started with an initially stationary free surface or alternatively a wave field can be imposed. It is thus suitable for simulating the free-surface interaction. A limitation is that the code is serial and thus increasing grid resolution and domain size is costly in physical time. This also poses the problem of memory space as the RAM demands increase with increasing number of grid cells. However the free-surface interaction occurs over a relatively short time scale compared to its life time. It is the aim of this project to investigate the interaction of the vortex ring at different stages in its lifetime. This can be best achieved in two steps. In step one, a vortex ring is evolved within the parallel fixed-boundary code until the vortex ring is at the desired state. The resulting velocity field can then be embedded within the free-surface code at a desired depth.

Chapter 5

Vortex ring initialisation methods

In this chapter we discuss different methods of initialising the simulations. The chapter is split into two sections concerning the initial velocity field of a vortex ring in an unbounded domain (§ 5.1) and the ring initialisation below a surface (§ 5.2).

5.1 Ring initialisation in an unbounded domain

The aim of the initialisation is to produce a coherent vortex ring which displays the intended characteristics in as short a development time as possible. Three initialisation methods were tested; a discussion of their strengths and weaknesses follows.

5.1.1 Initialisation method I

The initial velocity field for a vortex ring was defined by solving the inviscid analytical expression for the stream function derived from the Biot-Savart law by Yoon & Heister (2004) as

$$\psi = \frac{\Gamma}{2\pi} \left(\chi_1 + \chi_2\right) \left[\mathrm{K}\left(\iota\right) - \mathrm{E}\left(\iota\right)\right], \tag{5.1}$$

where $\mathrm{K}(\iota)$ and $\mathrm{E}(\iota)$ represent elliptic integrals of the first and second kind, $\iota = \left(\chi_2 - \chi_1\right) / \left(\chi_2 + \chi_1\right)$, $\chi_1^2 = z^2 + \left(r - R\right)^2$ and $\chi_2^2 = z^2 + \left(r + R\right)^2$. The 'vertical' u_z and 'radial' components u_r at each grid cell can then be evaluated from

$$u_r = -\frac{1}{r}\frac{\partial \psi}{\partial z}, \quad u_z = \frac{1}{r}\frac{\partial \psi}{\partial r}. \tag{5.2}$$

The analytical expression is for an inviscid ring with an infinitely thin core, which has an unphysical infinite propagation velocity as (2.2) is logarithmically singular for an infinitely thin core radius. This problem was overcome by patching a Gaussian distribution of vorticity on the core region. However, initial tests showed that the ring quickly broke down if the Reynolds number was greater than about 2000. Analysis of the ring velocity profile showed that the patched core region was not well matched to the analytically defined velocity field. The discontinuity created a sheet of vorticity around the circumference of the ring at the interface. The sheet of vorticity was concentrated over one grid cell and high in magnitude. It caused the ring to break down prematurely within a small number of time steps. Low Reynolds number simulations ($\mathrm{Re} < 2000$) did not experience the same premature breakdown, as viscosity quickly smoothed the velocity profile yielding a coherent vortex ring.

Inspired by these observations an improved method of pre-conditioning was adopted. A ring with an initially thin core was advanced in time with $\mathrm{Re} = 400$ until the core radius was the intended size, thus smoothing the patch and the analytical solution. The time scale of the conditioning phase was calculated using (2.4). Once the conditioning phase was over the simulations were restarted at the required Reynolds number. Perturbations in the form of broadband random noise of order 2% of the local velocity were added to the initialisation to encourage the Widnall instability to grow around the circumference of the core. The resultant azimuthal wave number was checked against the wave number predicted by Saffman (1978). It was found that the expected wavenumber did not develop around the azimuth, which favoured a four or eight wave configuration dependant on the size of the core slenderness ratio ϵ, with smaller ϵ yielding the eight wave pattern. Other drawbacks of the method were that thin rings could not be initialised and the conditioning phase resulted in a lack of control of ring geometry.

5.1.2 Initialisation method II

The rational behind initialisation II was to improve the previous method by avoiding the problematic switch between the inviscid flow field and the Gaussian core. A new method[1] incorporated a relaxation term, with magnitude of the desired

[1] suggested by Dr K Shariff in a private communication

core radius δ, into the definition of χ, yielding: $\chi_1^2 = z^2 + (r-R)^2 + \delta^2$ and $\chi_2^2 = z^2 + (r+R)^2 + \delta^2$. The velocity field for the whole domain could now be calculated from the stream function (5.1) without the need of a Gaussian patch for the core region. A $\pm 2\%$ random noise scaling was added to the velocity field to excite the azimuthal ring instability. The vortex ring was found to adopt the correct number of azimuthal waves and broke down in a time scale consistent with the numerical simulations of Shariff *et al.* (1994). However close examination of the vorticity field at $t = 0$ showed that the method produced a core distribution with a long tail of relatively low vorticity in both the radial and z-directions. This meant that rings with $\epsilon > 0.3$ suffered canceling of vorticity on the ring centreline, reducing the overall circulation. It was also difficult to determine the relationship between the magnitude of the relaxation factor and resultant core radius, thus this method also lacked a degree of control.

5.1.3 Initialisation method III

The third method initialised a vortex ring with a Gaussian distribution of vorticity around the azimuth of the ring, as used by Shariff *et al.* (1994), with

$$\omega_\theta = \frac{\Gamma}{\pi\delta^2}\, e^{-s^2/\delta^2}, \tag{5.3}$$

where $s^2 = z^2 + (r-R)^2$. Small initial perturbations were added to the vortex ring in the form of a local displacement of the radius R around the azimuth of the ring. Thus s^2 can be written as $s^2 = z^2 + (r - R'(\theta))^2$. We suppose that the local radius $R(\theta)$ can be written as a small parameter $\varsigma \ll 1$ multiplied by the sum of a set of N Fourier modes, each with unit amplitude and random phase, so that

$$\begin{aligned} R'(\theta) &= R_0\,[1 + \varsigma f(\theta)] \\ f(\theta) &= \sum_{n=1}^{N} A_n \sin(n\theta) + B_n \sin(n\theta), \end{aligned}$$

where $A_n^2 + B_n^2 = 1$. However, although this method would lead naturally to a divergence-free velocity field, the continuity of the vortex lines themselves is not guaranteed – partly because the vorticity should be tilted slightly to follow the tangent to the path of the vortex centreline, and partly because the implied cross-section area of the vortex is not perfectly constant around the ring. The above vorticity field can be corrected to become divergence-free by superimposing the

gradient of a scalar field $\nabla\phi$ and requiring that ϕ satisfy a Poisson equation whose source term is the divergence error of the original vorticity field[2],

$$\nabla^2\phi = -\nabla \cdot \omega. \tag{5.4}$$

The complete initial field is then obtained by solving for the vector stream function that is consistent with the corrected vorticity distribution ω^c,

$$\nabla^2\psi = -\omega^c, \tag{5.5}$$

and the velocity field then follows directly by taking its curl,

$$\mathbf{u} = \nabla \times \psi, \tag{5.6}$$

where $\mathbf{u}$ is the velocity field and ψ is the vector stream function. This method of perturbation also allow us to excite solitary modes or groups of modes if the need arose. The method produced a coherent vortex ring that developed the correct azimuthal number of waves as predicted by theory and experiments and was thus adopted as the initialisation technique for the subsequent investigations.

It was noted, by Shariff *et al.* (1994), that the initial Gaussian distribution of vorticity is only an exact steady solution in the limit of infinitely thin cores. Since the Gaussian cores specified here have finite size (and thus only approximately satisfy the Navier-Stokes equations) the ring initially undergoes an 'equilibration' phase, during which the ω_θ profile across the core region relaxes toward a new equilibrium state. This is obtained after the Gaussian profile approaches the axisymmetric inviscid ideal for which, in axes attached to the ring, ω_θ/r is solely a function of the streamfunction ψ. The core profile must thus depart from the initially symmetric Gaussian distribution, and become skewed, with ω_θ decreasing faster toward the bubble edge than the ring centre. Our results show that during the equilibration phase ω_θ is shed from the ring (figure 5.1(a)) reducing the circulation and modifying the ring geometry; this process is most severe for thick-core rings (figure 5.1(b)).

[2]The maximum correction to the vorticity field was less than 1.7%.

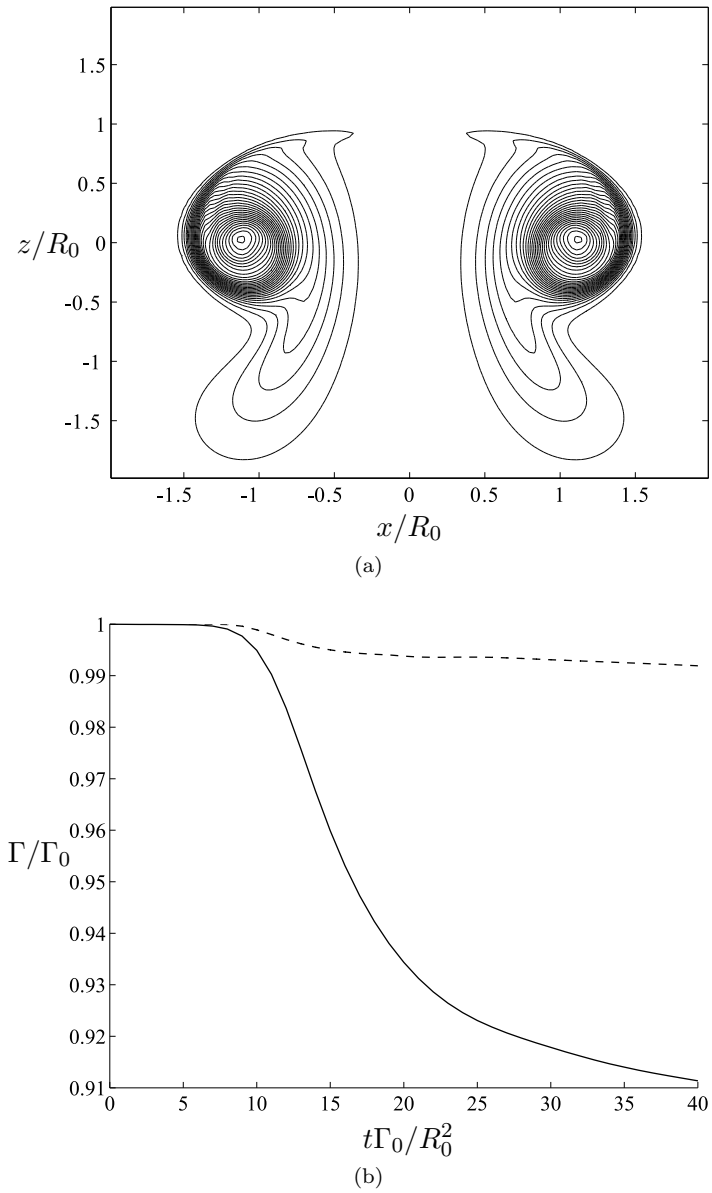

FIGURE 5.1: Ring adjustment during the equilibration; (a) Vorticity shedding visualised by ω_θ contours for a thick-core ring, $\epsilon = 0.4131$, at time $t\Gamma_0/R_0^2 = 5$; increments $\omega_\theta^{max}/50$. (b) Loss of Γ for two ring of different core thickness: $---$, $\epsilon = 0.2$; —, $\epsilon = 0.4131$.

5.2 Ring initialisation below a surface

By introducing surface boundary conditions we are in effect constraining the size of the simulation. One of the aims is to investigate rings at different stages of their life cycle. However, allowing a laminar ring to transition naturally to turbulence before it is in contact with the surface would require an extremely long domain, unfeasible for the present codes. In light of this we have devised a ring embedding

method which allows the ring to be defined a given distance from the surface at the desired stage of its evolution.

5.2.1 Embedding method

The embedding method makes use of ring simulations in the unbounded investigation. The first step is to extract the entire vorticity field from the unbounded simulation once the ring has evolved to the desired state and store it in an output file. The intended surface investigation may not have the same domain dimensions or cell density, in which case the output file is then modified to reflect the free-surface domain. The vorticity is almost entirely concentrated around the ring in the centre of the domain, with the exception of a relatively small wake, and naturally becomes zero in the lateral x and y-directions toward the boundaries (and indeed far from them). This allows us to reduce or expand the domain simply by adding or subtracting zeros from the output file. The velocity field is then evaluated from the vorticity field and its vector stream function using (5.5) and (5.6).

The above is sufficient to initialise a surface investigation as the Froude number tends to zero as $g \to \infty$ leading to an 'infinitly stiff' free surface. For cases where $\mathrm{Fr} > 0$, however, we must also prescribe an initial surface deformation consistent with the vorticity field below. Failure to initialise the free surface correctly leads to the formation of a propagating surface wave with wavelength equal to the lateral box size. The wave is created due to an imbalance between the pressure in the cells directly below the surface and their hydrostatic value leading to an impulse on the surface. As we define a relatively low viscosity the wave is not significantly damped during the simulation. It is thus crucial to prevent its creation to avoid modification of the ring behaviour. In effect, we require the pressure field to be known before the first time step. An approximation for the pressure field is found by simulating the ring with free slip boundary conditions for a small number of very small time steps $\Delta t = 0.00001 R_0^2/\Gamma_0$. The pressure in the cells in the highest $x - y$ plane are then used to prescribe a surface elevation through use of the Bernoulli equation,

$$h = \frac{p}{g}. \tag{5.7}$$

Note, in the case of the CGLES rigid lid code the pressure field contains an arbi-

trary constant which must first be subtracted from the local pressure before the initial surface elevations are calculated. Testing showed that this method prevented the generation of the initialisation wave if the ring was embedded below $2R_0$.

5.2.2 Surface wave field

In prescribing a surface wave field we appeal to the linear theory of surface gravity waves ignoring the effect of surface tension. This is a reasonable assumption as the vortex rings of most interest here are of large scale (typically of radius $\approx$ 10m) and we limit our interest to the interaction of waves with amplitude small compared to wavelength. The surface waves take the form of a sine wave described by

$$h = a\sin\left(\frac{2\pi kx}{L_x}\right), \tag{5.8}$$

where a is the wave amplitude,k is the wavenumber and L_x is the computational domain width. In shallow water, the irrotational velocity field for linear gravity waves can be derived from Laplace's equation, $\nabla^2\phi = 0$, where ϕ is the velocity potential (Lighthill, 1978). It follows that the velocity field corresponding to the waves is given by

$$u = \frac{a\xi}{\sinh(kL_z)}\cosh(kz)\sin(kx), \tag{5.9}$$

$$w = -\frac{a\xi}{\sinh(kL_z)}\sinh(kz)\cos(kx), \tag{5.10}$$

where $\xi = \tanh(kL_z)(gk)^{0.5}$ is the angular frequency.

Chapter 6

Investigation of vortex ring evolution from a laminar to a turbulent state

In this chapter[1] we present results from DNS of single naturally evolving laminar vortex rings with different relative core thicknesses and Reynolds number, and examine their initial breakdown and transition into the early stages of turbulence. After the mathematical and numerical preliminaries are presented in § 6.1 and § 6.2, the cases of interest are introduced in § 6.3, along with analysis of the numerical approach in § 6.4. We next investigate the laminar evolution of the ring (§ 6.5.1), and the wake generation, modal growth, and wave breaking during the linear (§ 6.5.2) and nonlinear (§ 6.5.3) regimes, with special attention paid to the generation of secondary vorticity structure. Finally we investigate, using Lagrangian particle-path analysis, the relationship between the amount of entrainment or detrainment and the various stages of the ring evolution (§ 6.5.4) and the possibility of an axial flow generation in the core region (§ 6.5.5).

6.1 Mathematical background

For the vortex ring evolution investigation we consider a single vortex ring of radius R and core radius δ, with circulation Γ and Reynolds number $\mathrm{Re} \equiv \Gamma/\nu$, with

[1] Much of the material in this chapter has been presented in Archer *et al.* (2008); see Appendix B.

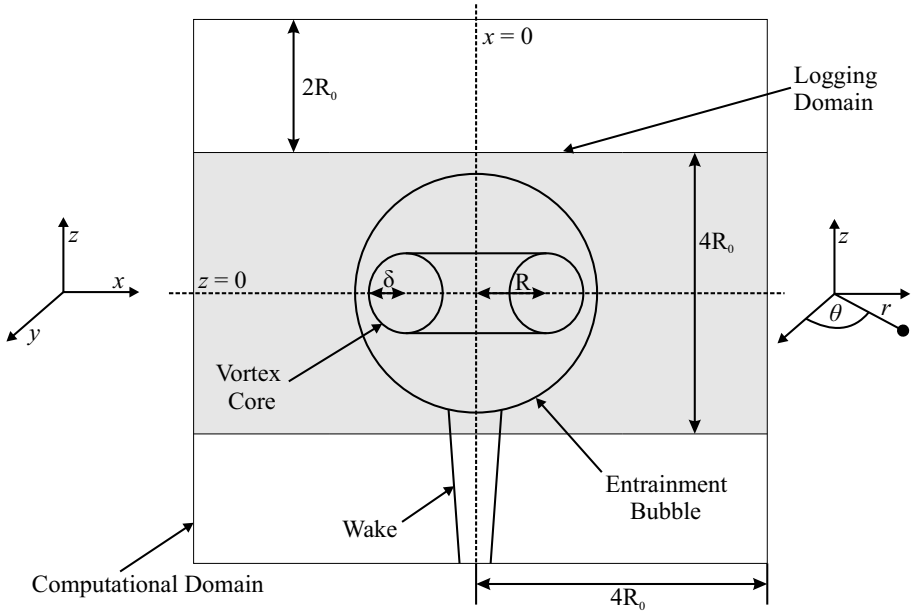

FIGURE 6.1: Schematic diagram of the vortex ring domain, the shaded region corresponds to the logging domain.

impulse $\mathbf{P}$ propagating along the positive z-direction with respect to Cartesian coordinates $\mathbf{x} = (x, y, z)$ and with corresponding velocity components $\mathbf{u} = (u, v, w)$; see figure 6.1. The vortex is initiated such that it is centred about $\mathbf{x} = (0, 0, 0)$ at time $t = 0$ and, after an initial adjustment (see section 6.5.1), propagates at a velocity U that depends on its instantaneous parameters according to (2.2)

We follow Saffman (1970) and define the vortex-ring geometry in terms of integral parameters. For example, under the assumption of axisymmetry (reasonable for a laminar ring), measures of the ring radius can be extracted from the first and second radial moments of the azimuthal vorticity ω_θ, with

$$R_\theta = \frac{1}{\Gamma}\int r\omega_\theta \,\mathrm{d}r\mathrm{d}z \quad \text{and} \quad R_2^2 = \frac{1}{\Gamma}\int r^2\omega_\theta \,\mathrm{d}r\mathrm{d}z, \tag{6.1}$$

where the circulation Γ and impulse P take their usual forms,

$$\Gamma = \int \omega_\theta \,\mathrm{d}r\mathrm{d}z \quad \text{and} \quad P = \pi R_2^2\Gamma, \tag{6.2}$$

and $r^2 = x^2 + y^2$. Equivalent three-dimensional formula can be derived for more general non-axisymmetric distributions of vorticity. The ring radius R_θ can be interpreted as the radial ω_θ-weighted average, and the core thickness δ_θ as the

ω_θ-weighted measure of its spread. For a Gaussian ω_θ distribution we have

$$\delta_\theta^2 = 2(R_2^2 - R_\theta^2). \tag{6.3}$$

These quantities are referred to below as impulse-weighted measures of the vortex geometry; they are particularly useful because of their close relationship to the integral parameters. It is also convenient to define an integral measure of the ring radius R_Ω based on the first moment of enstrophy via

$$R_\Omega \;=\; \frac{1}{2\Omega}\int r|\omega|^2 \,\mathrm{d}x\,\mathrm{d}y\,\mathrm{d}z, \tag{6.4}$$

where $\Omega = \int |\omega|^2 \mathrm{d}x\,\mathrm{d}y\,\mathrm{d}z$ is the total enstrophy. Since the laminar ring produces a wake of shed vorticity, all characteristic ring radii and integral properties presented in this paper have been calculated over a 'logging domain', the top and bottom of which are two initial ring radii R_0 from the origin (see figure 6.1). This prevents the wake from artificially distorting measures of the ring parameters.

6.2 Numerical Approach

The fixed-boundary code was used for all vortex life time investigations as described in § 4.2. The Cartesian computation domain assumes periodic boundary conditions in the x and y-directions, so that we are, in effect, simulating an infinite array of vortices, but with the domain widths L_x and L_y chosen to be sufficiently large that the effects of periodicity are small (see below). However, because the vortex sheds a wake, the ring propagation direction (z) cannot be treated as periodic if interactions with its own wake are to be avoided. We therefore use inflow and outflow boundary conditions, at $z = +L_z/2$ and $-L_z/2$ respectively, and perform the calculations with respect to a moving reference frame attached to the ring. The time-dependent axial velocity $W_1(t)$ of this moving reference frame is adjusted by a simple control algorithm to keep the ring at a fixed vertical location within the domain. It thus provides the inflow boundary condition at $z = +L_z/2$, with $w(x, y, L_z/2) = W_1(t)$. (This assumes that L_z is large enough, compared to the ring radius R, that the velocity induced by the ring vorticity at the inflow plane is negligible.) In order to avoid introducing spurious vorticity into the domain, Neumann conditions are applied to the other two components at $z = +L_z/2$: $\partial u/\partial z = \partial v/\partial z = 0$. At the outflow, $z = -L_z/2$, all three components satisfy a linear gradient condition, with $\partial u/\partial z = \partial v/\partial z = \partial w/\partial z = 0$.

Calculation of the reference-frame speed W_1 (i.e. the time-dependent inflow velocity) requires a time-dependent measure of the vertical ring location Z. We use

$$Z(t) \;=\; \frac{1}{2\Omega}\int z|\omega(t)|^2\,\mathrm{d}x\,\mathrm{d}y\,\mathrm{d}z, \tag{6.5}$$

where Ω is the total enstrophy (cf. (6.4)). The value of W_1 that minimises the difference between $Z(t)$ and the target location $Z_c = 0$ is determined by an integral-proportional controller,

$$W_1(t) \;=\; 2c_1\left(Z(t) - Z_c\right) + c_2^2\int_0^t \left(Z(t') - Z_c\right)\,\mathrm{d}t', \tag{6.6}$$

where c_1 and c_2 respectively set the damping and oscillation timescales. These were chosen to give a critically damped response with $c_1 = 2\Gamma_0/R_0^2$ and $c_2 = 4\Gamma_0/R_0^2$ (where the 0 subscript indicates initial values), which locates the ring to within $10^{-3}R_0$ of Z_c by three R_0^2/Γ_0 time units, and to within $5\times10^{-5}R_0$ by $20R_0^2/\Gamma_0$. Once the ring is locked in place, it remains in the centre of the domain throughout the computation, despite shedding circulation and impulse, and changing its translational velocity.

Since the DNS effectively approximates the motion of a single vortex ring by considering a periodic array of rings in x and y, it is necessary to quantify the influence of the implied image vortices, which act to reduce the speed at which the ring propagates, compared to the infinite-domain idealisation. The amount of this reduction can be calculated by integrating the net effect of the velocity induced by the neighbouring rings, located at distances $\mathbf{x} = (i\xi_x, j\xi_y, 0)$ from the point in question, where ξ_x and ξ_y are respectively the x and y periods of the image array, and i and j are integers. The velocity induced by a single image is $\mathbf{U} = \nabla\wedge\mathbf{A}$, where $\mathbf{A}$ is the far-field velocity potential, which for $|\mathbf{x}| \gg R$ is

$$\mathbf{A} = \nabla\wedge\left(\frac{(0,0,R^2\Gamma)}{4\,|\mathbf{x}|}\right).$$

The net induced axial velocity $\widetilde{w}$ is thus

$$\widetilde{w} = -\frac{\Gamma R^2}{4\xi^3}\sum_{i=1,\,j=1}^{\infty}\frac{i^2+j^2}{\left(i^2+j^2\right)^{5/2}} \approx -9.032\frac{\Gamma R^2}{4\xi^3}, \tag{6.7}$$

where we assume a square array, with $\xi = \xi_x = \xi_y$, and the i,j summation has been evaluated numerically. This gives both a criterion for choosing the lateral

Case	δ_0/R_0	Γ_0/ν	$N_x \times N_y \times N_z$	$t^*\Gamma_0/R_0^2$	Γ^*/Γ_0	R_θ^*/R_0	δ_θ^*/R_0
A1	0.413	5500	256×256×256	40.0	0.907	1.038	0.373
A2	0.413	10000	256×256×256	40.0	0.911	1.038	0.360
B1	0.200	5500	256×256×256	25.0	0.992	0.999	0.243
B2	0.200	10000	384×384×384	25.0	0.995	1.000	0.227
B3	0.200	7500	512×512×512	25.0	0.993	1.000	0.232
C1	0.140	3000	256×256×256	15.0	0.999	0.995	0.203

TABLE 6.1: Run parameters. The $*$ superscript indicates quantities at the sampling initiation time t^*.

sizes L_x and L_y of the domain, and also allows the translational velocity exhibited by the ring in the finite-domain simulation to be corrected and compared to the corresponding infinite-domain experimental results. Note that since Γ and R vary with time so does the $\widetilde{w}$ correction, and that the ratio of $\widetilde{w}$ to the velocity induced by the local ring within a square domain of size L is $O(R/L)^3$ (2.2).

6.3 Simulation parameters

The parameters that define the six cases summarised in table 6.1 allow consideration of the effects of both Reynolds number $\mathrm{Re} = \Gamma_0/\nu$ and the slenderness ratio $\epsilon_0 = \delta_0/R_0$. Since this part of the study will revisit some of the issues first raised by Shariff *et al.* (1994), two of our runs have been designed to match theirs. The Case A1 and B1 values respectively correspond to those used for their Runs 3 and 12, with $\mathrm{Re} = 5500$ for both and $\epsilon_0 \approx 0.4$ and ≈ 0.2, defining rings within the thick- and thin-core regimes. Cases A2 and B2 are higher Reynolds number versions of A1 and B1, respectively, with $\mathrm{Re} = 10000$. Case B3 defines another $\epsilon_0 = 0.2$ thin-core ring, at an intermediate Reynolds number, $\mathrm{Re} = 7500$. This case, with its intermediate Re and higher spatial resolution, will be especially useful when we examine the nonlinear breakdown and the early stages of the fully turbulent regime. Finally, Case C1 was designed to help determine the expression for the translational velocity constant C (see § 6.5.1), by capturing both thin- and thick-core behaviour. The number of grid cells employed in each direction (N_x, N_y, N_z) is shown in table 6.1. The quality of the spatial resolution is examined below. A cubic Cartesian domain was used for all cases, with $L_x/R_0 = L_y/R_0 = L_z/R_0 = 8$. Equation (6.7) implies that this introduces

differences between the finite- and infinite-domain ring translational velocity of approximately $0.005\Gamma_0/R_0$. All cases also utilised a constant timestep, with the Courant-Friedrichs-Lewy (CFL) number, based on local velocity and grid size, always less than 0.15. A radius perturbation of amplitude $\varsigma = 2 \times 10^{-4}$ was imposed on the first 32 azimuthal modes for the thin-core rings (Cases B1, B2, B3 and C1), while for (thick-core) Cases A1 and A2 the first 24 modes were disturbed, following the approach of Shariff *et al.* (1994).

6.4 Assesment of the numerical approach

6.4.1 Cell resolution

The reliability and accuracy of the fixed-boundary code was assessed by comparing the results of Case A1 with linear-instability results obtained with an in-house fully spectral third-order Runge-Kutta code[2] using $192 \times 192 \times 768$ Fourier modes[3]. The spectral domain was large enough ($L_z = 32R_0$) in the z-direction to prevent the ring interacting with its wake during the time considered. (Were it not for the need to employ nonperiodic boundary conditions in z, the fully spectral code could have been used for this part of the study.)

Excellent agreement was found for the ring translational velocity and integral measures, as well as the linear-regime growth rates of the azimuthal disturbances, which after adjusting to a slightly different random initialisation eventually track each other; see figure 6.2.

A further check of the spatial resolution is provided in figure 6.3, which shows histories of the rate of change of the volume-integrated kinetic energy K (per unit mass) within the simulation domain, with respect to the frame of reference attached to the ring[4]. Within an infinite domain the rate of change of K is equal to the volume-integrated rate of kinetic energy dissipation $-\epsilon_K$. However, since kinetic energy is lost to the wake and convected out of the finite domain, here the energy balance is altered such that

$$\frac{\mathrm{d}K}{\mathrm{d}t} = -\epsilon_K + F_K, \tag{6.8}$$

[2]Written and run by Dr C.P. Yorke of University of Southampton.

[3]This involved a 288^3 collocation grid, to allow de-aliasing of the spatial derivatives.

[4]The moving coordinate system and the associated unsteady inflow define an effective pressure gradient of $-\mathrm{d}W_1/\mathrm{d}t$, such that $K = \frac{1}{2}\int_V (u_i u_i - {W_1}^2)\mathrm{d}V$, where V is the volume of the DNS domain.

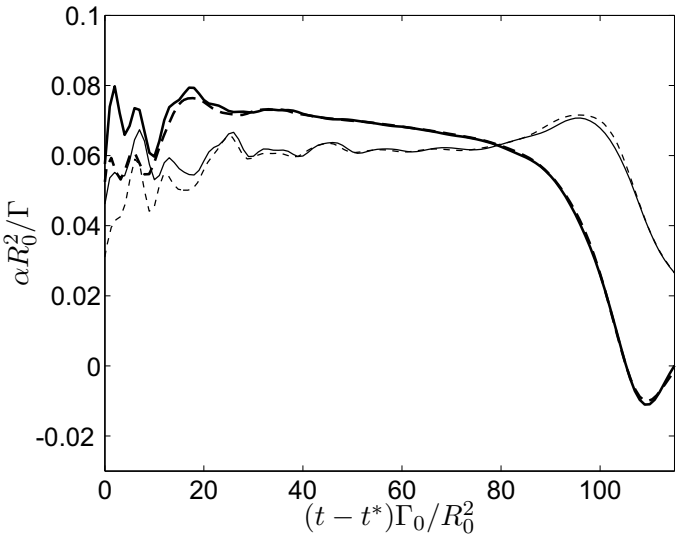

FIGURE 6.2: Comparison of modal growth rates for azimuthal modes $n = 5$ (thin line) and $n = 6$ (thick line): — , Case A1; – – – , $192 \times 192 \times 768$ spectral DNS.

where F_K is the net volume-integrated kinetic energy flux, set by the difference between the (unsteady) fluxes at the inlet and outlet planes. The difference between the left- and right-hand sides of (6.8) is a measure of the spatial discretisation error in resolving the smallest turbulence scales. For all six cases the difference was within $1 \times 10^{-5}\Gamma_0^3/R_0$ up to the point of transition. Transition involves stretching of the vorticity filaments to fine scale, resulting in an enstrophy and dissipation peak. Note that the flux term F_K is only significant after the ring breaks down and its turbulent wake reaches the outflow boundary (compare the solid and chain dot curves in figure 6.3). Even during this most difficult to resolve phase ($t > 80R_0^2/\Gamma_0$) the accuracy is reasonable, with the error remaining less than $2.2 \times 10^{-4}\Gamma_0^3/R_0$.

6.4.2 Sensitivity to domain size

The influence of the distance of the ring to the boundaries was addressed by repeating Case A1 using two larger domains. In one simulation, the box width (x-y plane) was increased to $12R_0 \times 12R_0$, to assess the influence of the image vortices, and to confirm the validity of the periodic correction $\tilde{w}$ (6.7). In the other simulation, the box height (z-direction) was increased to $16R_0$, to assess the influence of distance from the ring to the upstream and downstream boundaries. As shown in figures 6.4 and 6.5, the effect of increasing the domain size is negligible for all featured results. Figure 6.4 compares slenderness ratio ϵ, ring radius measures R_θ and R_Ω, circulation Γ and translational velocity U (which includes

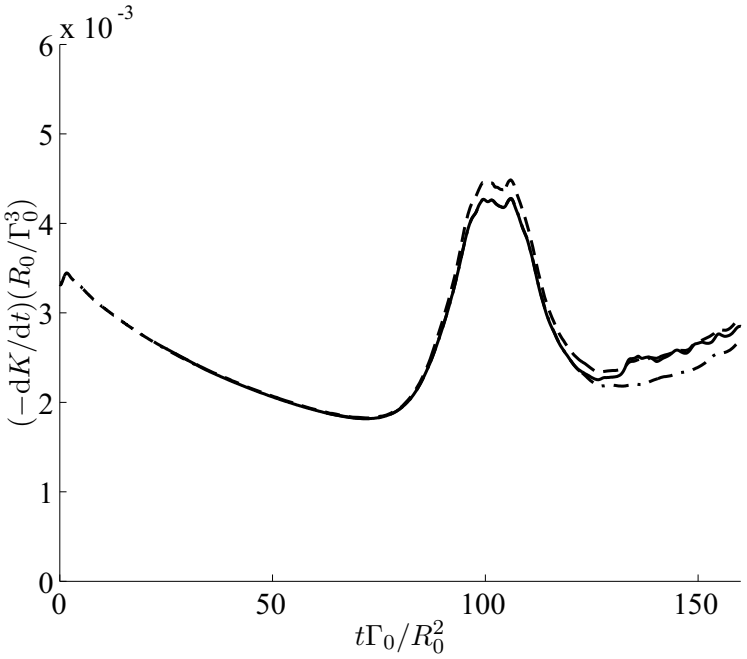

FIGURE 6.3: Numerical integrity. History of rate of change of volume-integrated kinetic energy K for Case B3 (thin core): $---$, $-\mathrm{d}K/\mathrm{d}t$; $-\cdot-$, ϵ_K; —, $\epsilon_K - F_K$. Dissipation and flux terms shown for $t \geq t^*$, where t^* is the sampling initiation time (see § 6.5.1).

the correction factor $\tilde{w}$) for the different domains. The evolution of the vortex ring radius measures are least affected by the domain size, with a maximum difference of 0.2%. The other ring measures show the same order of accuracy, all within 0.5%. Also shown, in figure 6.5, is the history of the growth rate of the most amplified azimuthal mode, which for this case is the $n = 6$ mode. Again the agreement across the different domain sizes is excellent, with the maximum difference during the linear growth phase less than 1%. The accuracy of the velocity correction $\tilde{w}$, employed to account for the finite lateral domain size and the resulting retarding effect of the periodic spanwise array of rings, is demonstrated by the close agreement in U between the different sized domains (figure 6.4(d)). For the original $8R_0$x$8R_0$x$8R_0$ domain $\tilde{w}$ is approximately $4 \times 10^{-3} R_0/\Gamma_0$. This is an order of magnitude larger than the difference ($4 \times 10^{-4} R_0/\Gamma_0$) between the ring translational velocities for the $8R_0$x$8R_0$x$8R_0$ and $12R_0$x$12R_0$x$8R_0$ domains, after the respective corrections have been added. The maximum relative difference between the translational velocities (after $\tilde{w}$ has been added) is 0.25%. We thus have confidence that the results have not been spuriously affected by the domain size or the velocity correction $\tilde{w}$.

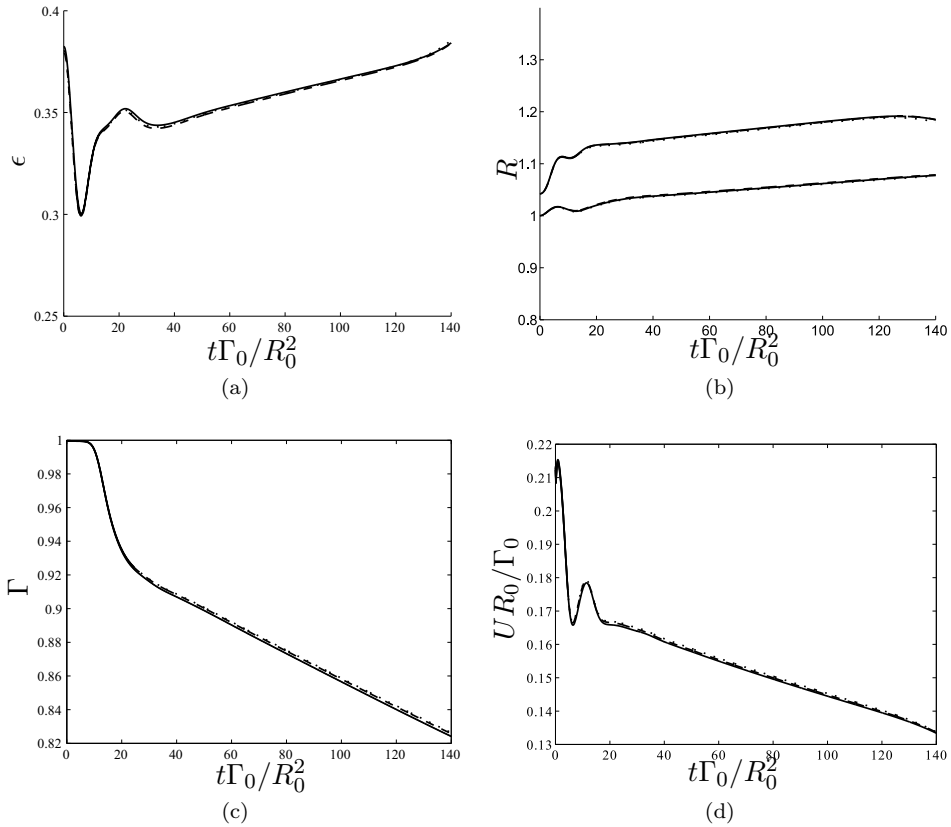

FIGURE 6.4: Comparison of ring characteristic parameters for Case A1 with three different sized domains: — , $8R_0$x$8R_0$x$8R_0$; · · · , $8R_0$x$8R_0$x$16R_0$; – – – , $12R_0$x$12R_0$x$8R_0$. (a) Evolution of slenderness ratio $\epsilon = \delta_\theta/R_\theta$. (b) Evolution of R_θ and R_Ω. (c) Decay of circulation Γ. (d) History of ring translational velocity U. (Note U includes the velocity correction $\tilde{w}$.)

6.5 Results

6.5.1 Laminar Evolution

As mentioned in § 5.1.3, the ring initially undergoes an 'equilibration' phase, during which ω_θ is shed from the ring, reducing the circulation and modifying the ring geometry; this process is most severe for thick-core rings. These observations led us to define a *sampling initiation time* t^* at a time just after equilibrisation has occurred, such that the core vorticity distribution has fully adjusted and the associated shed vorticity has left the logging domain, thereby avoiding spurious measurements of the ring characteristics. (The impact of the start-up wake as it passes out of the logging domain can be seen in the local increase in circulation decay rate between $t = 5$ and $15R_0^2/\Gamma_0$ in figure 6.8) The initial sampling time is documented together with the ring parameters associated with this time (indicated

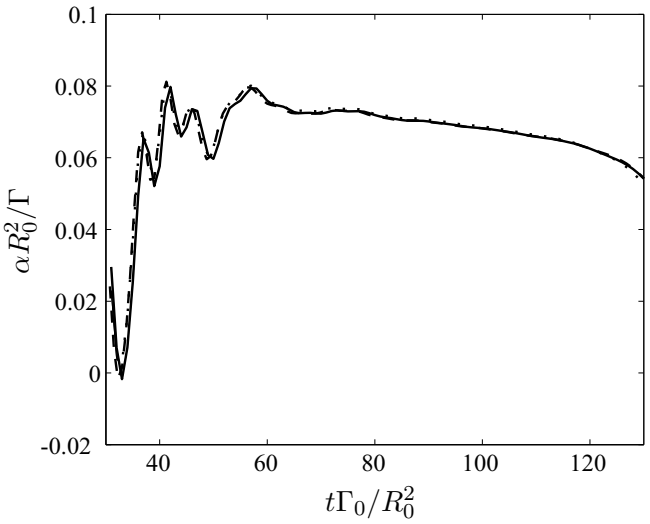

FIGURE 6.5: Comparison of azimuthal growth rates of the most amplified $n = 6$ mode for case A1 with three differently sized domains: — , $8R_0$x$8R_0$x$8R_0$; $\cdots$, $8R_0$x$8R_0$x$16R_0$; $- - -$, $12R_0$x$12R_0$x$8R_0$.

by an * superscript) in table 6.1.

Having adjusted, the ω_θ profile extends outside the instantaneous zero streamline (broken vertical line, see figure 6.6) for both the thin- and thick-core rings, but to a far greater degree for the thick-core ring. Vorticity extending across the zero streamline is nominally outside of the entrainment bubble. It can then either be entrained back into the bubble or transverse the bubble surface and depart into the wake, as suggested by Maxworthy's model for diffusive entrainment (Maxworthy, 1972). Figure 6.7 shows precisely this mechanism, with weak vorticity (shaded contours on right-hand side) trailing into the wake over the zero streamline (thick-solid contour). The fact that vorticity crossing the instantaneous $\psi = 0$ streamline can be entrained back into the entrainment bubble is due to the fact that the zero streamline is not stationary and moves in time to incorporate changes to the ring translational velocity and integral parameters. The Eulerian view would see any vorticity crossing the zero streamline into the irrotational fluid convected into the wake. However the vorticity takes time to transverse the bubble surface down towards the rear stagnation point. During this time the zero streamline can expand, encompassing vorticity previously outside the entrainment bubble. Lagrangian analysis of the flow yields an entrainment bubble surface which takes into account the moving $\psi = 0$ streamline. Vorticity diffused across this boundary, outboard of the zero streamline, passes into the wake. These arguments are explored further in § 6.5.4. Whether the 'leaked' vorticity is recovered or not, the vorticity profile is clipped by the presence of the entrainment bubble surface. This vorticity clipping

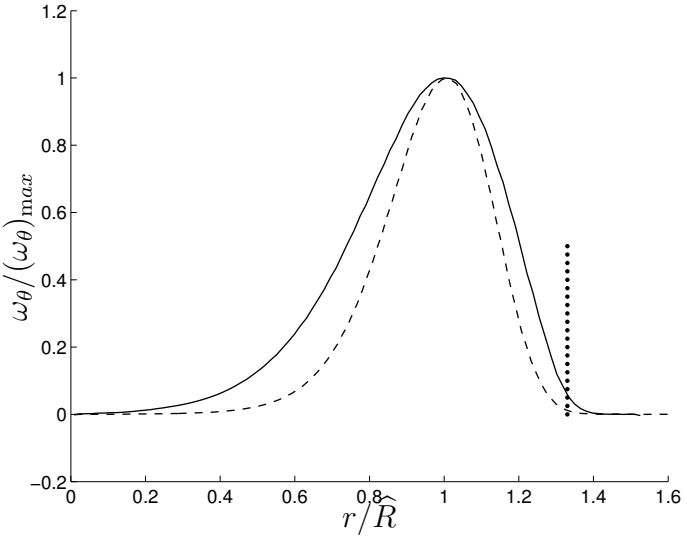

FIGURE 6.6: Comparison of core vorticity distributions for a thick- and a thin-core ring, at $t = t^*$: — , Case A1 ($\epsilon_0 = 0.41$); – – – , Case B1 ($\epsilon_0 = 0.20$). Broken vertical line indicates the location of instantaneous zero streamline on the concurrent plane. Radial locations nondimensionalised by local $\widehat{R}$, the distance from the origin to the peak in ω_θ.

leads to a sharpening in the ω_θ profile in the vicinity of the zero streamline surface, hence increasing the skewness of the core. It is interesting that for both cases the instantaneous zero streamline surface appears at a constant distance $r \approx 1.33\widehat{R}$ from the ring centreline, where $\widehat{R}$ is the current radial location of the ω_θ peak. The instantaneous zero streamline surface thus expands to track radial displacement of the vorticity peak as the core diffuses, leading to a relationship between the core thickness and the rate of decay of ω_θ.

The loss of ω_θ manifests itself in an overall reduction of ring circulation. Figure 6.8 displays the rate of decay in circulation during the laminar regime. The main figure shows the rate of decay from the start of the simulation, with the early peaks corresponding to the vorticity shed during the core adjustment leaving the domain. We focus on the inner figure which presents the behaviour when the core has adjusted its vorticity distribution, after t^*. Comparing Cases A1 with B1 and A2 with B2, we see that despite similar initial Reynolds numbers Γ^*/ν the thick-core rings reduce in circulation faster than the thin-core rings. This can be attributed to the increased skewness of the thick-core rings with the result of greater ω_θ extension across the entrainment bubble surface. The rate of circulation loss increases with time for the thin-core rings, which is consistent with the ongoing core diffusion, such that they become increasingly skewed. The thick-core rings, on the other hand, exhibit a larger but more-nearly constant rate of circulation

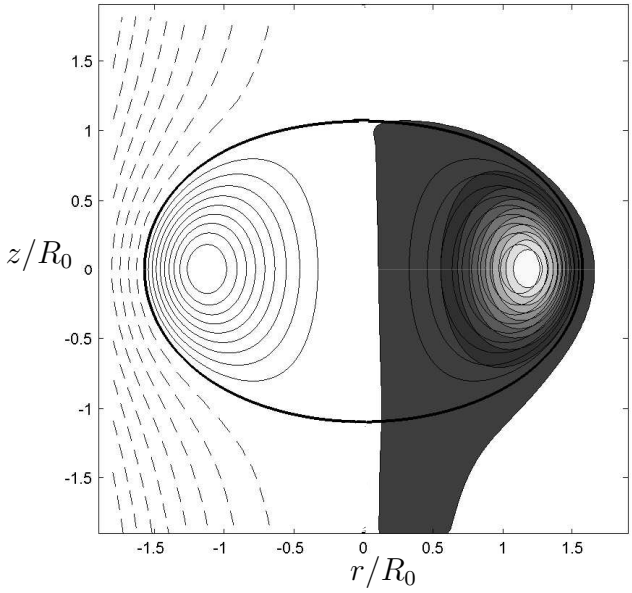

FIGURE 6.7: Loss of of azimuthal vorticity ω_θ for Case A1 at $(t-t^*)\,\Gamma_0/R_0^2 = 20$: — , $\psi \leq 0$ (thicker contour denotes $\psi = 0$); – – – , $\psi > 0$; shaded contours show ω_θ (darker contours show weaker vorticity).

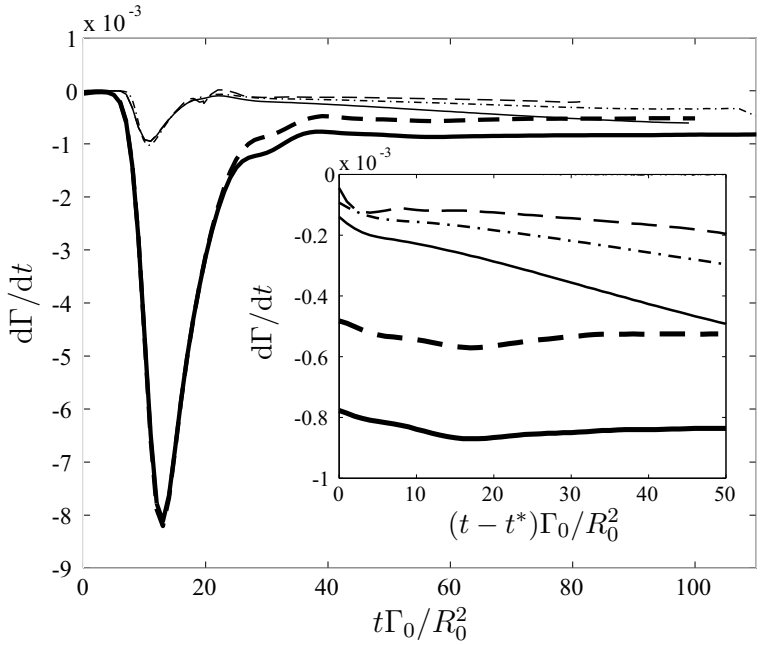

FIGURE 6.8: Histories of rate of change of circulation $\mathrm{d}\Gamma/\mathrm{d}t$: — , Case A1 (thicker line) and B1 (thinner); – – – , Case A2 (thicker) and B2 (thinner); – · – , Case B3.

loss, since they are closer to a quasi-steady state defined by fixed ϵ (compare figures 6.9(a) and 6.9(b)), and thus experience little change to their skewness and associated relative rate of ω_θ diffusion.

Maxworthy's model for diffusive detrainment (Maxworthy, 1972) predicts a -2/3 power law decay of Γ. The decay rate was not found to be universal by Dabiri & Gharib (2004) however, who experimentally generated rings at Reynolds numbers between 2000 and 4000, finding that Γ decayed with power laws between -0.27 and -0.067, with the power decreasing with increasing Reynolds number. We find for the present rings that the circulation tends to decay as $\Gamma \sim t^c$ where c is in the range -0.01 to -0.002. One can account for the range of reported circulation decay rates by the difference in Reynolds numbers across the previous and present cases. As shown in figure 6.8, for identical initial ϵ the decay rate increases monotonically with decreasing Reynolds number.

The laminar evolution of the core radius measures, δ_θ, a_e and a_1[5], normalised by the instantaneous value of R_θ, and the ring radii measures R_θ and R_Ω are shown in figure 6.9, for two rings that typify the behaviour of thin and thick cores (Cases A1 and B3). To calculate a_1, the core centre was first determined by linear interpolation, then second-order polynomial extrapolation was used to find the distance from the core centre to the location of the maximum tangential velocity on the plane $z = 0$ inboard and outboard of the core centre. These two lengths were then averaged to give a_1.

Since the integral measure R_Ω is weighted by $|\omega|^2$ it is biased toward regions of high vorticity and hence approximates the radial location of peak vorticity. On the other hand, R_θ (being weighted by ω_θ) effectively yields the radial location of the centre of vorticity of the core, which during the laminar regime is always inboard of R_Ω, due to the skewness of the core ω_θ profile. The difference between the two measures is thus an indication of the core skewness, which is greater for thicker cores. Note that, prior to transition, R_θ for the thin-core rings is approximately constant, while R_Ω increases slightly with time, demonstrating the increasing skewness of the thin-core rings due to core diffusion. The thick-core rings behave differently, in that both R_θ and R_Ω increase with time. This shows that the ring is expanding radially while the skewness of the core remains approximately constant.

The three dotted lines in figure 6.9 (a) and (b) represent the predicted core diffusion for an equivalent core with a Gaussian profile in accordance with (2.3). The history of the thin-core ring follows the Saffman diffusion equation very closely, with the exception of a_e/R_θ, which deviates with time away from the upper dotted line. The divergence can be attributed to the increasing core skewness. As the core ω_θ distribution becomes less Gaussian, the translational velocity of the ring

[5] see § 2.1

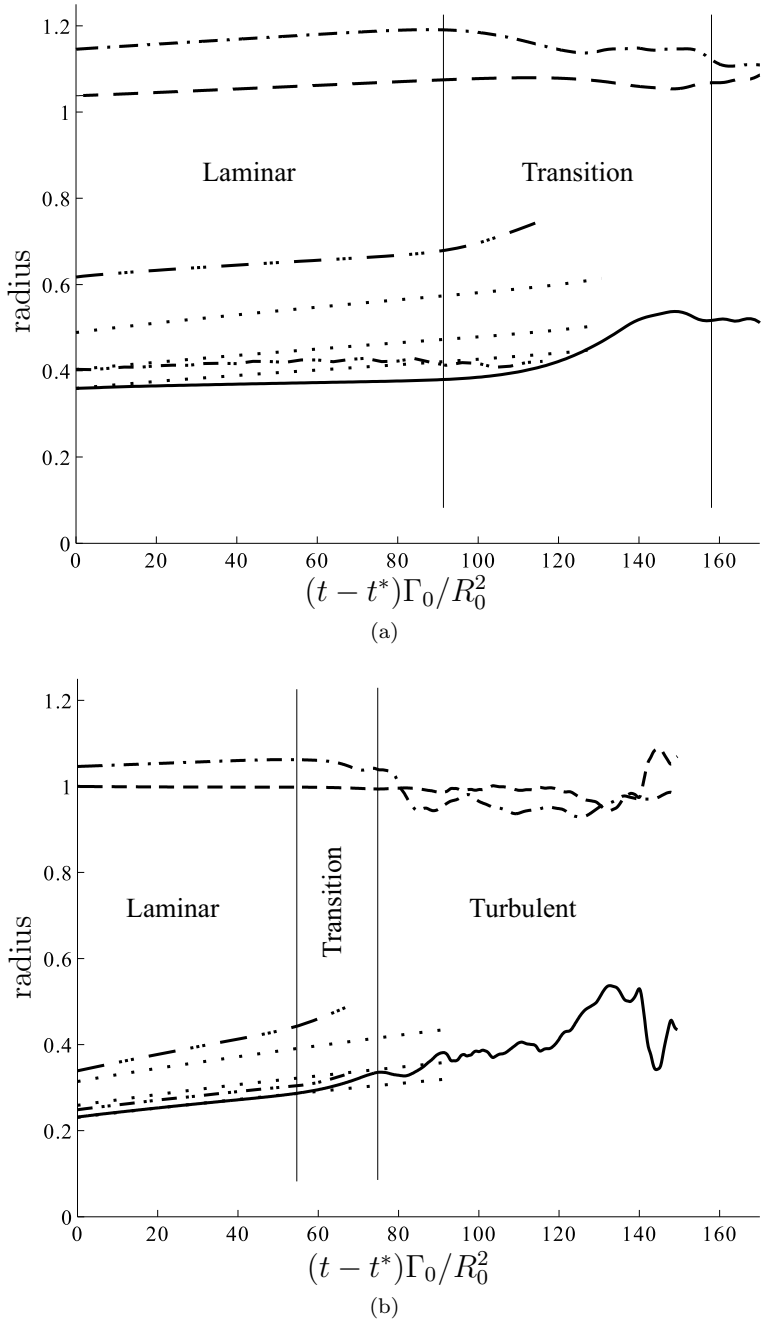

FIGURE 6.9: Histories of core and ring radii for (a) Case A1 (thick core) and (b) Case B3 (thin core): — , δ_θ/R_θ; – · · · – , a_1/R_θ; – · · · · – , a_e/R_θ; · · · , theoretical core diffusion determined by (2.3) nondimensionalised by R_θ, (with the lower line corresponding to δ_θ, the middle to a_1 and the upper to a_e); – – – , R_θ/R_0; – · – , R_Ω/R_0.

reduces with an associated increase in a_e (cf. (2.2)). For the thick-core ring, the slenderness ratios a_1/R_θ and δ_θ/R_θ remain approximately constant with time. The core expansion is constrained by the ring geometry, as ω_θ must equal zero on the ring centreline and its outer extent is clipped by the zero entrainment streamline

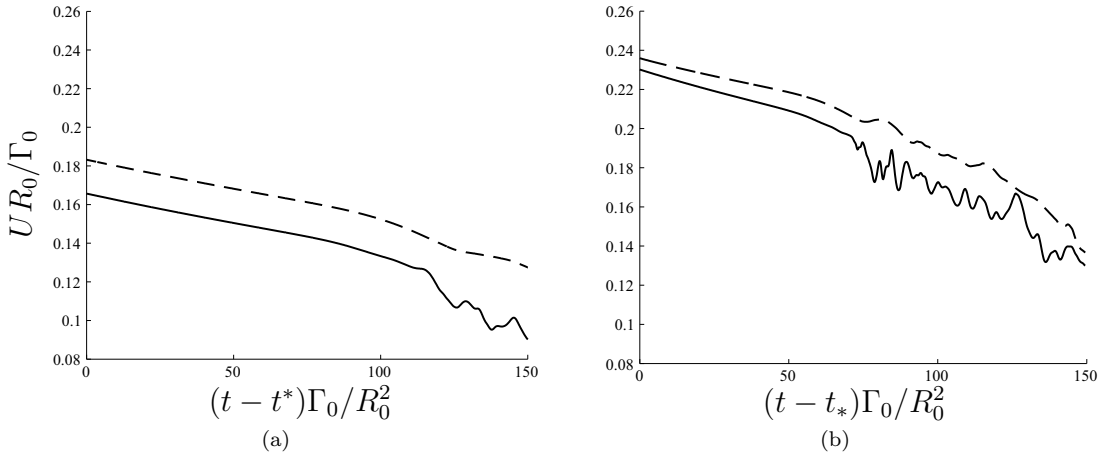

FIGURE 6.10: Histories of vortex translational velocity for (a) Case A1 (thick core) and (b) Case B3 (thin core): – – – , U_{G}; — , U_{DNS}.

(which expands at the same rate as the radius). Consequentially the core diffuses at a very similar rate to the ring radius, leading to a nearly constant ϵ. With both ϵ and hence the degree of skewness nearly constant, the core distribution of vorticity changes little, resulting in the nearly constant rate of decay of circulation for thick cores seen in figure 6.8.

The transitional and early turbulent behavior of the ring is also presented in figure 6.9, to give perspective to the laminar results. Transition begins near $(t - t^*)\Gamma_0/R_0^2 = 95$ and 55 for Cases A1 and B3, respectively, with the decrease of R_Ω as the core distorts and the development of interior and peripheral vortical structures moves the location of the maximum vorticity. The transitional and early turbulent behavior will be examined further in § 6.5.3.

Histories of the translational velocity U of the thick- and thin-core rings are shown in figures 6.10(a) and 6.10(b) respectively, and compared to equivalent rings with a Gaussian core profile. These include the periodic correction $\widetilde{w}$ (cf. (6.7)) to account for the induced velocity of the periodic array of vortices, so we in effect report the translational velocity of a single vortex ring in an unbounded domain. The Gaussian ring velocity U_{G} is given by (2.2), where $C = -0.558$ and the instantaneous values of Γ, R_θ and δ_θ are taken from the DNS results. The difference between U_{G} and the numerical results reveal the impact of the non-Gaussian core ω_θ distribution. The difference is greater for the highly skewed thick-core rings and remains almost constant as the core diffusion is limited (for reasons given above). Since for thin-core rings the ω_θ distribution becomes increasingly skewed as the simulation progresses, the difference between the Gaussian and the DNS velocity

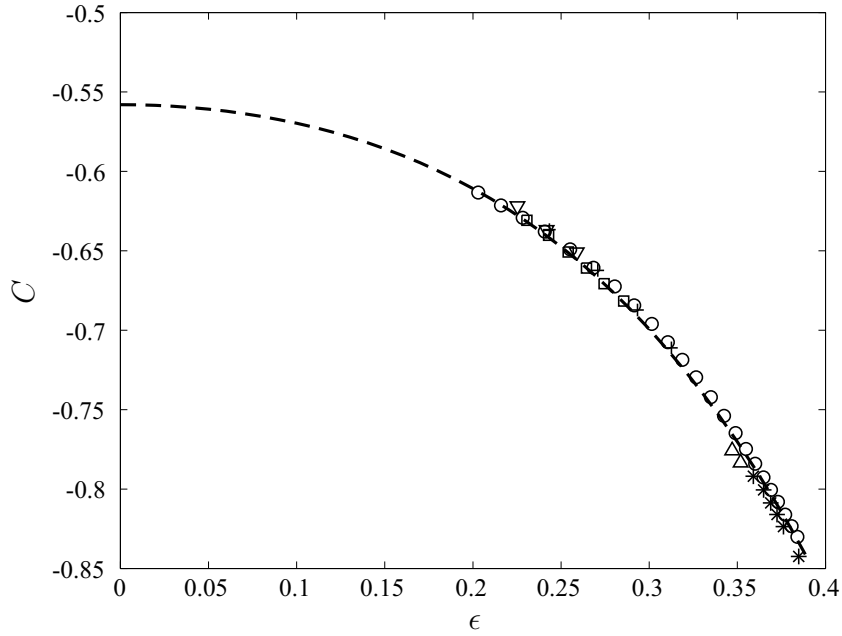

FIGURE 6.11: Translational velocity parameter C vs ϵ: – – – , $C = -5.0\epsilon^2 - 1.12\epsilon^4 - 0.558$; $*$, Case A1; Δ, Case A2; $+$, Case B1; ∇, Case B2; $\Box$, Case B3; $\circ$, Case C1.

increases with time. For all cases the rings decelerated smoothly until the onset of turbulence, whereby the translational velocity fluctuates as it decays.

The inclusion of C in (2.2) allows for cores with finite slenderness ratios ϵ that possess non-Gaussian core distributions. The difference between the ring translational velocity and that of a Gaussian-core ring increases with time as the core diffuses. This implies that C becomes increasingly negative with increasing ϵ. One might expect that the effect of increasing skewness would manifest itself as an even-series expansion in ϵ^2, i.e. C can be approximated as $C = A\epsilon^2 + B\epsilon^4 + C'$, where the constant C' must equal -0.558, since for small finite ϵ, C must equal -0.558. The parameter C has been extracted from the simulations and is plotted in figure 6.11 against the instantaneous value of $\epsilon = \delta_\theta / R_\theta$ for all cases. The results are well approximated by $C = -1.12\epsilon^2 - 5.0\epsilon^4 - 0.558$ (dashed curve). The generalized expression for the translation speed of a laminar vortex ring as a function of Γ, R and ϵ then becomes

$$U = \frac{\Gamma}{4\pi R}\left[\ln\left(\frac{8}{\epsilon}\right) + A\epsilon^2 + B\epsilon^4 + C' + \ldots\right], \tag{6.9}$$

where $A = -1.12$, $B = -5.0$ and $C' = -0.558$.

6.5.2 Instability Growth

During the initial laminar phase an azimuthal instability associated with the vortex core develops, and deforms the core into a standing wave with an integer number n of waves around the circumference. The number of modes depends on the slenderness ratio such that $n \sim 2.26/\epsilon$ (for a Gaussian core distribution of vorticity (Shariff *et al.*, 1994)). The growth rate of a mode n is defined as $\alpha_n \equiv \frac{1}{2}(1/E_n)\mathrm{d}E_n/\mathrm{d}t$, where E_n is the energy of the mode. The inviscid case was examined by Widnall & Tsai (1977) deriving the growth rate α_{WT} (2.6). However, the numerical study of Shariff *et al.* (1994) found that the effect of viscosity is to reduce the growth rate from the inviscid value by a factor that depends on the local internal Reynolds number of the core, and established a viscous correction factor (2.7). Shariff *et al.* formulated the viscous correction by comparing the measured growth rates for a number of rings with ϵ varying from 0.2066 to 0.4131, and across a range of Reynolds numbers Re from 1200 to 10000. They determined the growth rate as being that of the most amplified azimuthal mode (i.e. the mode with the largest growth rate at a given time, not necessarily the mode currently with the most energy) observed at a time $\bar{t}\Gamma_0/R_0^2$ between 52.5 and 57.5. The growth rate was averaged over 15 R_0^2/Γ_0 time units centred about $\bar{t}$. However, as the vortex ring geometry changes slowly over time because of viscous diffusion of the core, the most amplified mode will also slowly change. In fact, successive modes with reducing n will be selected and amplified, so that the average growth rate measured by this method can be expected to be slightly lower than suggested by the equation above.

Shariff *et al.* estimated the internal Reynolds number Re_S at time $\bar{t}$ using the core measures a_1 and a_e, and assuming a Gaussian core distribution of vorticity diffusing in accordance with (2.3) (accurate for thin cores but less so for thicker ones). Finally, α_{WT} was calculated using the initial ring parameters and it was found that $\alpha_1 = 18$ fitted their results well.

The main differences between our numerical investigation and the simulations of Shariff *et al.* are that our boundary conditions are not periodic in the direction of ring propagation and that we use a cubic domain rather than a cylindrical one. The latter requires us to interpolate our velocity fields onto a cylindrical grid in order to extract the modal energy spectrum and associated modal growth rates. An azimuthal Fourier transform was performed over the cylindrical grid to reveal the modal energy histories displayed in figure 6.12. We follow Shariff *et al.* and report the growth rate of the most amplified mode at $\bar{t}\Gamma_0/R_0^2 = 52.5$, averaging the

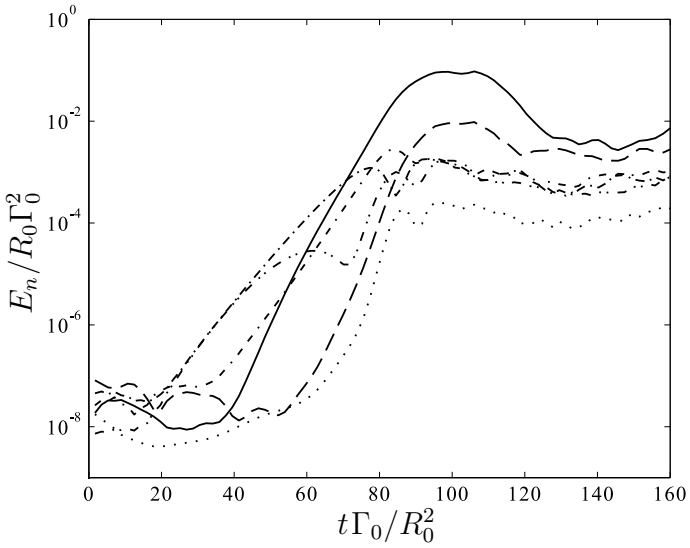

FIGURE 6.12: Evolution of selected azimuthal modal energies for Case B3: — , $n = 1$; – – – , 2; – – · – – , 9; – · – , 10; – · · – , 11; · · · ,18.

Case	$\bar{t}$	$n\left(\bar{t}\right)$	α	α_S	$\Gamma(\bar{t})$	$R_\Omega(\bar{t})$	$a_e(\bar{t})$	$a_1(\bar{t})$	$\alpha_{WT}(\bar{t})$	$\alpha_S(\bar{t})$
A1	52.5	6	0.072	0.090	0.897	1.173	0.65	0.44	0.081	0.069
A2	52.5	6	0.082	0.098	0.904	1.144	0.62	0.42	0.087	0.080
B1	52.5	9	0.099	0.108	0.989	1.062	0.42	0.30	0.128	0.103
B2	47.5	10	0.130	0.126	0.995	1.044	0.34	0.26	0.141	0.124
B3	52.5	9	0.112	0.119	0.989	1.056	0.39	0.28	0.133	0.113

TABLE 6.2: Comparison of present growth rate α with Shariff *et al.* (1994) viscous prediction α_S. Time $\bar{t}$ given in units of R_0^2/Γ_0, growth rates in units of Γ_0/R_0^2, circulation in units of Γ_0 and lengths in units of R_0.

growth rate over a time window of $\pm 7.5 R_0^2/\Gamma_0$ centred at $\bar{t}$. The Case B2 result, however, is reported at the earlier time of $\bar{t}\Gamma_0/R_0^2 = 47.5$ to avoid the possibility of being affected by the nonlinear regime. The growth rate α_S was calculated using the instantaneous values of a_1 and a_e at $\bar{t}$ as approximated by (2.3) and Γ_0 and R_0 in accordance with the methodology used by Shariff *et al.*

A comparison between the present growth rates α and those given by the Shariff *et al.* (1994) viscous correction α_S is presented in table 6.2. It is found that α_S is within 9% of α for the thin-core rings, Cases B1, B2 and B3. However, the difference is greater for the thick-core cases, A1 and A2, at approximately 25%. The difference in growth rates for the thick-core rings can be attributed in part to the periodicity of the Shariff *et al.* simulations in the direction of ring propagation.

Ring	α_{Daz}	$\alpha_{WT,Daz}$	$\alpha_{S,Daz}$	α'_{WT}	α'_S
A′	0.78	1.36	1.00	1.39	1.02
C′	0.91	1.59	1.03	1.39	0.90

TABLE 6.3: Dazin *et al.*'s (2006a) experimental growth rates α_{Daz} and recorded quantities $\alpha_{WT,Daz}$ and $\alpha_{S,Daz}$ compared to α'_{WT} and α'_S which result from using a_1 in 2.6. Growth rates given in s^{-1}.

Since we follow essentially identical initialisation procedures, the Shariff *et al.* rings were subject to the same equilibrilisation phase as documented here. In Shariff *et al.*'s triply periodic computations the shed vorticity, associated with the vortex ring adjusting to its steady-state vorticity profile (see § 6.5.1), is ejected from the ring during the equilibration phase and cycles periodically through the domain. It interacts with the ring on each pass, providing a forcing of the ring instability. This explanation was verified using the in-house spectral DNS code mentioned earlier, periodic in all three directions, by initialising a thick-core ring in domains of different length. The longest domain ensured breakdown occurred before the wake interacted with the vortex ring and yielded a growth rate 10% less than for a domain of similar size to that used by Shariff *et al.* The growth rate for thin cores is more accurate because the initial equalibrilisation wake shedding is negligible, thus the rings are not influenced in the same way. As shown in § 6.5.1 all ring measures vary during the laminar regime, dependent on ϵ and the Reynolds number. This led us to test the Shariff *et al.* viscous correction by incorporating the instantaneous $\Gamma(\bar{t})$, $R_\Omega(\bar{t})$, $a_1(\bar{t})$ and $a_e(\bar{t})$ at $\bar{t}$ to estimate $\alpha_{WT}(\bar{t})$, $e(\bar{t})$ and $\mathrm{Re}_S(\bar{t})$, with $\alpha_S(\bar{t}) = \alpha_{WT}(\bar{t})[1 - \widehat{\alpha}_1/\mathrm{Re}_S(\bar{t})]$. Using this method and choosing $\widehat{\alpha}_1 = 8$ improves the agreement to within 5% for both the thin- and thick-core cases. This supports the validity of correcting the inviscid growth rate based on the internal Reynolds number Re_S.

Recently Dazin *et al.* (2006*a*) used PIV to calculate the instability growth rate of two of their experimental rings A′ and C′, reporting differences with their implementation of the Shariff *et al.* correction. However they followed a slightly different method to that proposed by Shariff *et al.* using a_e as their core measure in place of a_1 in calculating α_{WT}. We have followed the methodology of Shariff *et al.* to give a corrected prediction for their growth rates, α'_{WT} and α'_S (see table 6.3). The difference between the growth rate of ring C' and α_S is reduced significantly, however for ring A' the difference is still large. Another important

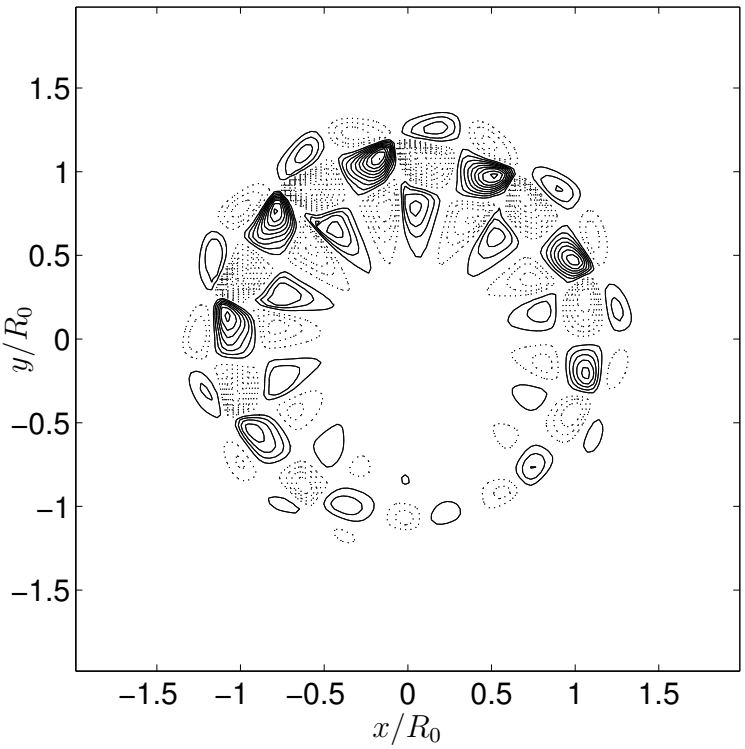

FIGURE 6.13: Contours of ω_z on the horizontal plane through centre of ring ($z = 0$) for Case B3 at time $(t - t^*)\Gamma_0/R_0^2 = 55$: — , $\omega_z > 0$; · · · , $\omega_z < 0$. Contour increments at $|\omega_{z\,max}|\,/10$.

difference between the two methods is the sampling period over which the growth rate is calculated. Dazin *et al.* had access to very few sample points over the entire laminar regime with which to calculate the growth rate. Figure 6.12 shows that this simplification is reasonable for mode 9, which grows at an approximately constant rate, but much worse for modes 10 and 11, as their growth rate changes greatly during the laminar regime. In general, the growth rate of a single mode will not be constant throughout the laminar regime, as viscosity diffuses the core region amplifying modes with monotonically decreasing mode number.

6.5.3 Non Linear Transition Phase

The elliptical instability initially leads to a narrow band of modes growing independently, which determine the number of standing waves around the core azimuth. However, at a certain amplitude the modes begin to interact nonlinearly with each other producing higher harmonics and lower-order intermodulation products (see figure 6.12), consistent with the experiments of Dazin *et al.* (2006*b*) and the simulations of Shariff *et al.* (1994). Constructive interference between neighbouring

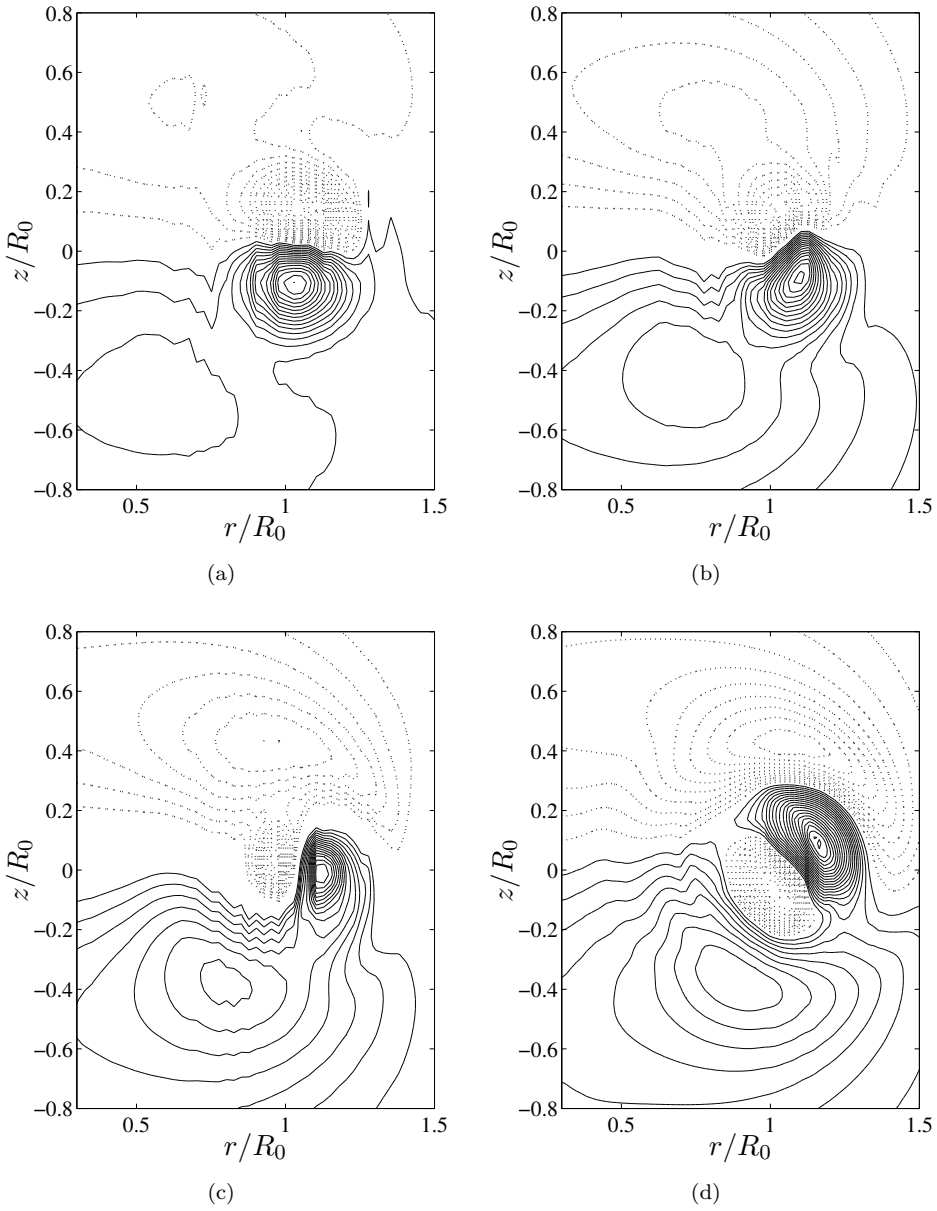

FIGURE 6.14: Contours of azimuthal velocity averaged around the ring azimuth at various times prior to the onset of turbulence. (a) Minimum contour level = 1×10^{-5}, increments of 2×10^{-5}, $(t-t^*)\Gamma_0/R_0^2 = 43.35$ (b) minimum contour level = 4×10^{-5}, increments of 2.5×10^{-5}, $(t-t^*)\Gamma_0/R_0^2 = 48.75$ (c) minimum contour level = 9×10^{-5}, increments od 4×10^{-5},$(t-t^*)\Gamma_0/R_0^2 = 52.35$ (d) minimum contour level = 1×10^{-4}, increments od 2×10^{-4}, $(t-t^*)\Gamma_0/R_0^2 = 61.35$.

modes causes a noticeable 'lob-sidedness' to the wave growth and associated core displacement, which is represented by the rapid growth of the $n = 1$ mode prior to transition. The relative dominance of the $n = 1$ mode varies from case to case and is largest for the thin-core Cases B1, B2 and B3, which during the nonlinear phase have 8,10 and 10 waves around the core respectively. An $n = 0$ mode also grows

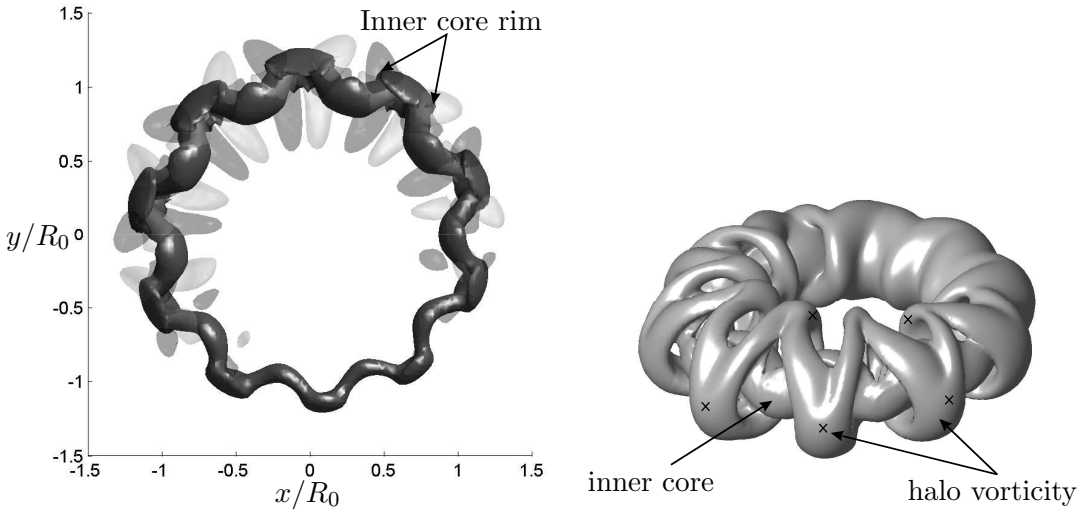

FIGURE 6.15: Three-dimensional isosurface visualisations of the secondary structures for Case B3 at $(t-t^*)\Gamma_0/R_0^2 = 65$. (a) Isosurfaces of vorticity viewed from above. Dark surface corresponds to the inner core region $|\omega|\, R_0^2/\Gamma = 3.8$; mid grey isosurface corresponds to $\omega_z R_0^2/\Gamma = 0.8$, light grey to $\omega_z R_0^2/\Gamma = -0.8$ visualising the secondary structure. (b) Isosurface of the second invariant of the velocity gradient tensor $\mathrm{II} = (\partial u_i/\partial x_j)(\partial u_j/\partial x_i)$, $\mathrm{II}R_0^4/\Gamma^2 = -0.005$, crosses mark the locations of saddle points where neighbouring loops meet.

rapidly in the azimuthal velocity energy component (i.e. an axial flow along the circumferential axis of the vortex core), which corresponds to a mean azimuthal profile of opposing streams, such that angular momentum is conserved. Initially the opposing streams are configured as two inner crescents, arranged one on top of the other in the core region and two outer maxima closer to the ring centreline (figure 6.14(a)). As the $n = 0$ mode intensifies, the inner crescents rotate anti-clockwise around the core centre as shown in figure 6.14, until the crescents have approximately switched positions and the ring breaks down into turbulence. Figure 6.14(d) shows the azimuthal profile just prior to turbulence and corresponds to the profile shown by Shariff *et al.* (1994) in figure 7 of their paper. A description of the nature of this axial flow follows in § 6.5.5.

Here we make a distinction between the region of intense vorticity at the core centre, which we call the 'inner core' and the surrounding outer core region of lower vorticity, which we call 'halo' vorticity (see figure 6.15(b)). The elliptical instability causes displacement of the inner core into a stationary wave pattern, while the halo vorticity displaces in the opposite direction, consistent with the second radial mode (Widnall, 1975). In a slice across the $z = 0$ plane the signature of the

second radial mode in the axial and radial components of vorticity is three layers arranged radially (figure 6.13). The halo vorticity occupies the inner and outer layers and is 180° out of phase of the inner core. The structure is also apparent in three-dimensional isosurface plots of the second invariant of the velocity gradient tensor II = $(\partial u_i/\partial x_j)(\partial u_j/\partial x_i)$(a useful marker of vortical structure), and isosurface plots of vorticity shown in figure 6.15. They show that as the inner core displacement becomes appreciable the halo vorticity rolls up into an interwoven mesh of secondary structure. The secondary structure develops first in the top left corner of figures 6.15(a) (bottom of figure 6.15(b)), where constructive interference between the azimuthal modes $n = 9$ and $n = 10$ yields the greatest inner core displacement. It then develops around the azimuth of the ring as the local inner core displacement increases with time. The figures further show that the secondary structure consists of a series of loops which encompass the inner core. The inner core weaves its way through the centre of the loops. It is noted that neighbouring loops are of alternating signed vorticity, consistent with the observations of Dazin *et al.* (2006*b*) and simulations of Bergdorf *et al.* (2007), and are formed by tilting and reorganisation of the halo vorticity. The loops touch at saddle points positioned in azimuthal planes aligned with the maximum and minimum inner core displacements but displaced radially in opposition to the core displacement (the approximate locations of the saddle points is denoted in figure 6.15(b) by crosses). Two loops wrap around each azimuthal wave, hence there are the same number of pairs of loops as there are waves around the ring. Bergdorf *et al.* (2007) give a slightly different account for the generation of the secondary structure, suggesting they originate due to stretching of the outer rim regions of the inner core. We also see stretching of the rims of the inner core (figure 6.16) but this occurs after the halo vorticity has reorganised into the secondary loops and their magnitude of vorticity $|\omega|$ has become comparable to the inner core.

The generation of the organised secondary structures coincides with deformation of the core ω_θ distribution. During the laminar regime the three-dimensional geometry of the core approximates a ring with a mildly elliptic cross section. During transition the cross section is distorted to form a thin crescent shape (figure 6.17). The distortion is more severe at regions of the core in the periphery of the entrainment bubble as the local radial expansion is restricted by the instantaneous zero streamline. The stretching of the inner core intensifies the local vorticity and is accompanied by stretching of the secondary structure, which also intensifies in vorticity causing an overall enstrophy peak (figure 6.3). As the secondary loops stretch they begin to protrude locally outside the entrainment bubble, trailing be-

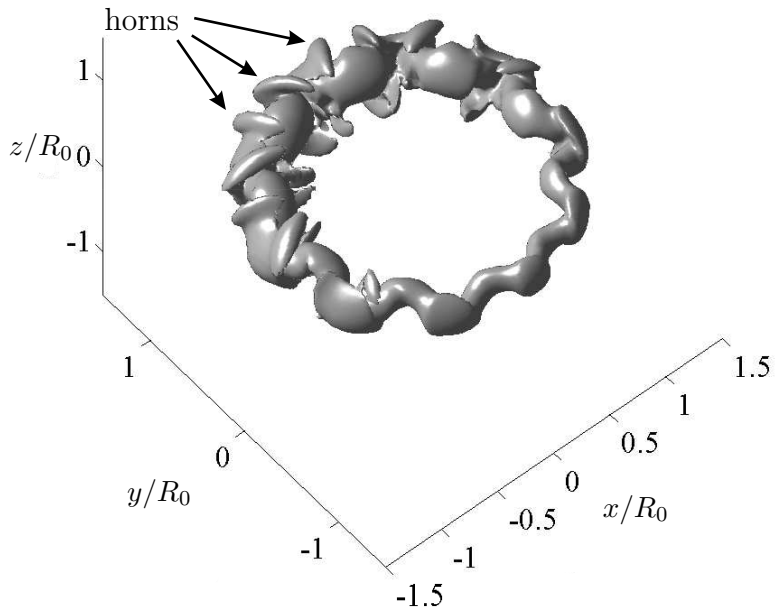

FIGURE 6.16: Formation of horn-like structures visualised with three dimensional isosurface of $|\omega|$, Case B3, $(t - t^*)\Gamma_0/R_0^2 = 64.95$. Surface level $\omega R_0^2/\Gamma_0 = 3.0$.

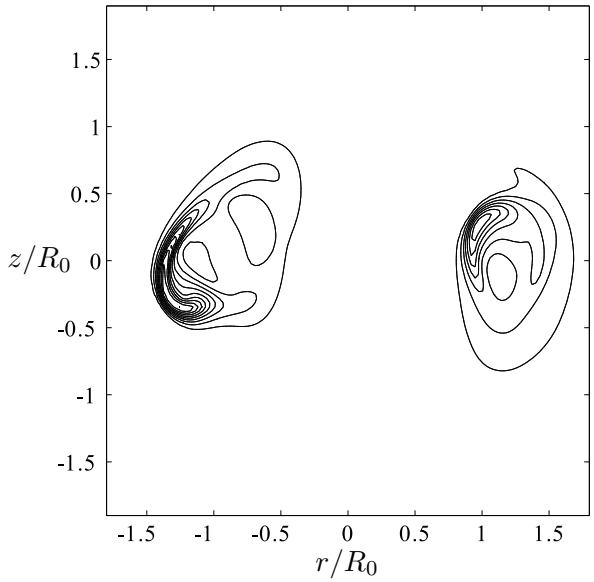

FIGURE 6.17: Contours of ω_θ on the vertical plane through the ring axis ($y = 0$), for Case A1 at time $(t - t^*)\Gamma_0/R_0^2 = 116$. Contour increments at $\omega_{\theta\,max}/10$.

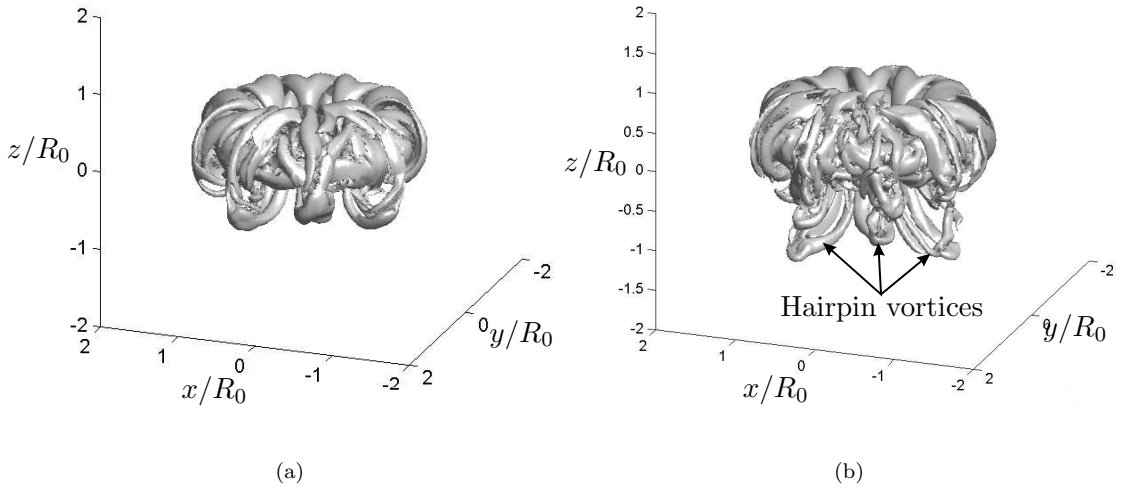

FIGURE 6.18: Isosurfaces of II showing the termination of the secondary structures forming hairpin vortices in the wake for Case B3 at (a) $(t-t^*)\Gamma_0/R_0^2 = 75.8$ and (b) $(t-t^*)\Gamma_0/R_0^2 = 79.4$. Surface level $\mathrm{II}R_0^4/\Gamma_0^2 = -0.25$.

hind the vortex ring and into the wake. The loops originally developed as counter rotating pairs side by side, but as they trail outside the ring the loops detach and reattach with their neighbour at the saddle point to form hairpin vortices that fill the wake (figure 6.18), as reported by Bergdorf *et al.* (2007). The localised equilibrium between the inner core and the outer halo vorticity is broken, as portions of the halo vorticity leave the entrainment bubble, and the core becomes locally turbulent at the position of the initial hairpin vortex shedding. The azimuthal instability wave does not rotate prior to the ring becoming turbulent, which conflicts with the inferences that Maxworthy (1977) made from smoke visualisations of the core region. The waves continue to develop across the remainder of the ring unhindered, until the secondary structure is shed into hairpin vortices around the entire azimuth of the ring and the ring can be considered to be fully turbulent.

The stationary coherent vortical structure found during the laminar and transitional phases is superseded by the swirling of vorticity filaments. Two cases were simulated and resolved through to transition and into the early turbulent regime: Case A1, a thick-core of low Reynolds number and Case B3, a thin-core of moderate Reynolds number. Figure 6.19(a) shows that the thick-core ring breaks down into a number of interwoven vortex filaments. No well-defined coherent core persists and circulation is shed via a continual stream of vortex filaments into the wake. The thin-core ring however maintains a core region of concentrated vor-

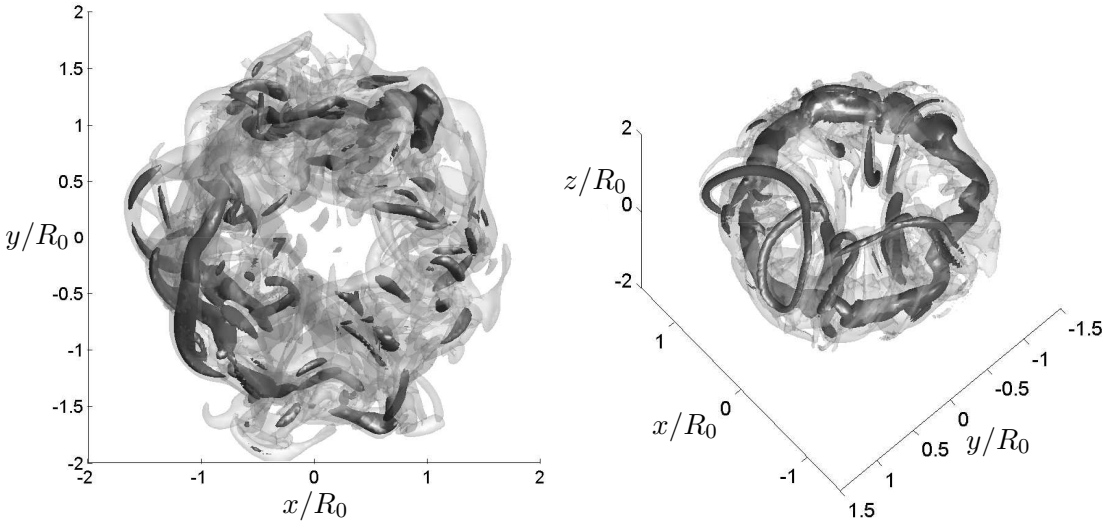

FIGURE 6.19: Double isosurface of $|\omega|$ for turbulent vortex rings. (a) Case A1 at time $(t - t^*)\Gamma_0/R_0^2 = 180$: dark surface level $|\omega|R_0^2/\Gamma_0 = 1.4$; light surface level $|\omega|R_0^2/\Gamma_0 = 0.7$. (b) Case B3 at time $(t - t^*)\Gamma_0/R_0^2 = 111.8$: dark surface level $|\omega|R_0^2/\Gamma_0 = 2.5$; light surface level $|\omega|R_0^2/\Gamma_0 = 1.25$.

ticity (the dark region in figure 6.19(b)) which is consistent with the turbulent visualisations of Wiegand & Gharib (1994). The core region is no longer stationary, but bends and twists with time. Vorticity filaments, similar to the secondary structure, are continually generated, wrapping around the turbulent core and circulating around it. Figure 6.19(b) shows a number of these vorticity filaments wrapped round the core region. The filaments have long looped tails that trail into the wake and out of the domain. Just as for the thick-core ring, these vorticity filaments circulate around the core and gradually pass out of the vortex bubble and into the wake as a stream of vorticity filaments and hairpin vortices, as visualised by Glezer & Coles (1990) and Wiegand & Gharib (1994). The ring was not simulated further into the turbulent regime, however the beginning of a staircase-like decay of circulation, as reported by Wiegand & Gharib (1994) and Bergdorf *et al.* (2007), was noted.

6.5.4 Particle Paths

Particle paths are a useful tool for analysing the entrainment and detrainment characteristics of the vortex ring. Particle paths were obtained by integrating the

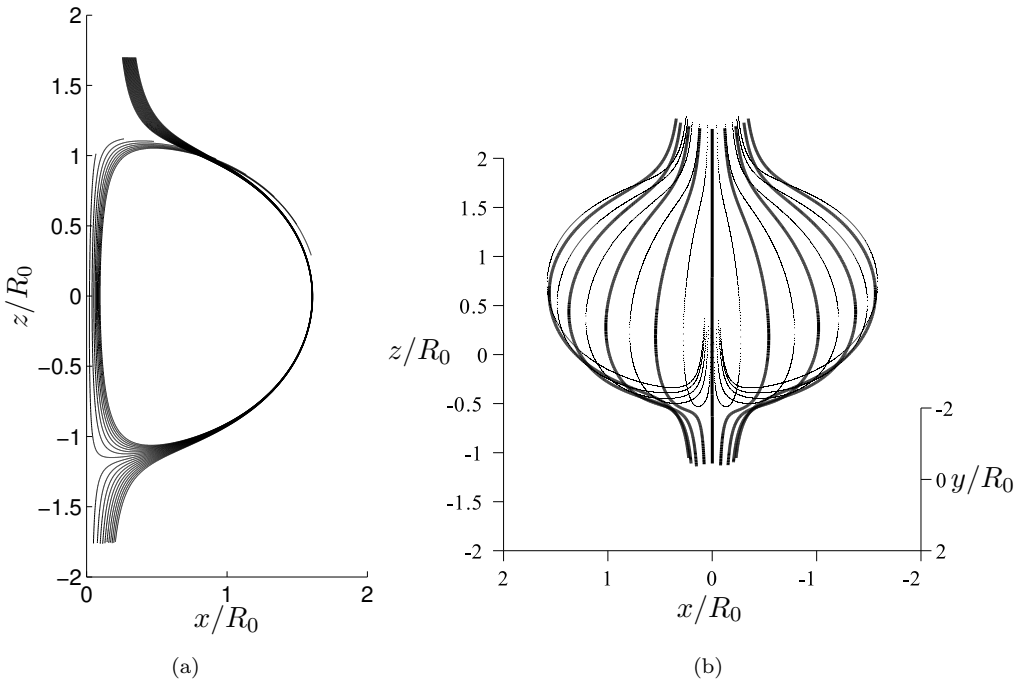

FIGURE 6.20: Laminar entrainment of tracked particles released at $(t - t^*)\Gamma_0/R_0^2 = 20$, for Case A1, on the $z = 1.7R_0$ plane. (a) Particles released on the $y = 0$ plane between $x = 0.25R_0$ and $x = 0.35R_0$ at increments of $0.005R_0$; (b) Particles released at equidistant azimuthal locations around the circumference of two semicircles of radius $0.25R_0$ (dotted), and $0.35R_0$ (solid).

ordinary differential equation,

$$\frac{\mathrm{d}\mathbf{x}\,(t)}{\mathrm{d}t} = \mathbf{v}\left[\mathbf{x}\,(t)\,, t\right] \tag{6.10}$$

where $\mathbf{x}\,(t)$ denotes the position vector of the particle and $\mathbf{v}$ is the time-dependent velocity field taken from the DNS. The sampling interval of the velocity field was determined to ensure convergence of the path lines, and was dependent on the complexity of the flow field. During the laminar phase the sampling interval was 20 time steps, reducing to 5 time steps during the transitional and early turbulent phase. Particles could be initialised at any location within the logging domain, figure 6.1, with the initial particle velocity, $\mathbf{v}\left[\mathbf{x}\,(t_0)\,, t_0\right]$, found by linear interpolation.

We first examine entrainment and detrainment characteristics of the thick-core ring, Case A1, during the laminar regime. Figure 6.20(a) shows the tracked particle pathlines for particles released at $(t - t^*)\Gamma_0/R_0^2 = 20$. The particles were

released at equal intervals on a line between $x = 0.25R_0$ and $x = 0.35R_0$ with a spacing of $0.005R_0$ in the $y = 0$ plane, at $z = 1.7$. As the particles pass around the entrainment bubble surface, the pathlines contract before diverging as they approach the rear stagnation point. At the rear stagnation point the particle pathlines are divided and are either entrained into the vortex ring bubble or pass past into the wake. Tracing back the pathlines of the entrained particles it is noted that a streamtube surface exists upstream of the vortex ring separating flow that will be entrained and flow that bypasses the vortex ring. Figure 6.20(b) shows a three dimensional visualisation of the process, the particles here have been released around the circumference of two semi circles on the plane $z = 1.7R_0$ of radii $0.25R_0$ and $0.35R_0$, with the particles within the streamtube surface, on the inner semi-circle being entrained. There is no detrainment of particles prior to the development of significant secondary structure, and the wake is created solely by vorticity diffusion.

It is important to note that during the laminar regime, no hole exists in the entrainment bubble surface through which the particles enter, recall figure 6.7 where the instantaneous streamlines are closed. As shown in § 6.5.1 the laminar ring gradually expands through radial growth and core diffusion, and decelerates to accommodate changes in the bubble geometry and loss of circulation. This increases the distance between the front and rear stagnation points and bubble volume. This results in an expansion of the instantaneous zero streamline which causes the entrainment of particles. Once inside the bubble the dynamics of the particles are governed by the highly vortical core region. The growth of the entrainment bubble is illustrated by the path of the entrained particles as they begin to circulate around the vortex core for a second time, figure 6.20(a), crossing there original path and circulating further away from the centreline. Although the particle paths have been limited so as not to extend indefinitely, the particle is in fact still inside the bubble and continues to circulate with an origin increasing in radial displacement from the ring centreline, as new fluid continually fills the outer reaches of the rear of the entrainment bubble. There is no detrainment of particles prior to the development of significant secondary structure, and the wake is created solely by vorticity diffusion, as evidenced in figure 6.7. The absence of particle detrainment implies that the stable and unstable manifolds of the front and rear stagnation points coincide exactly. This is only the case if no velocity perturbations exist on the propagation velocity of the vortex ring, which is confirmed by the straight velocity decay lines during the laminar regime of figure 6.10. In contrast, the Lagrangian bubble interface identified by a Lagrangian Coherent Structure (LCS)

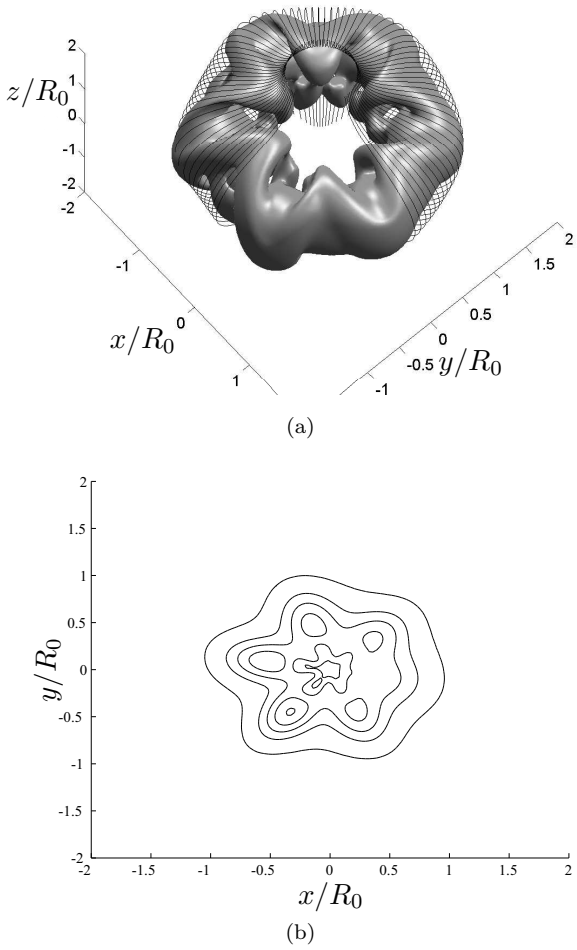

FIGURE 6.21: Entrainment bubble distortion for Case A1: (a) Lagrangian pathlines of particles initiated around a circle of radius $0.43R_0$ on the $z/R_0 = 1.9$ plane released at $(t - t^*)\Gamma_0/R_0^2 = 79$. An isosurface of II with surface level $\mathrm{II}R_0^4/\Gamma_0^2 = -0.005$, at $(t - t^*)\Gamma_0/R_0^2 = 110$ is included to aid visualisation; (b) ω_θ contours across the wake, increments of local $\omega_{max}/5$, at $(t-t^*)\Gamma_0/R_0^2 = 100$ on the $z = -1.95$ plane.

technique in the experiments of Shadden *et al.* (2006) exhibits alternating lobes of entrainment and detrainment during the laminar regime. Kumar *et al.* (1995) showed that experimentally generated rings at a similar Reynolds number to those studied by Shadden *et al.* (2006) initially experience large-scale oscillations in their translational velocity that persist for a short time after formation. We postulate that these experimental rings may also undergo an equilibrilisation phase similar to that observed in our simulation, during which the core adjusts to its steady-state profile. Changes in the distribution of vorticity within the core are sufficient to explain the initial oscillations in the translational velocity and associated lobe

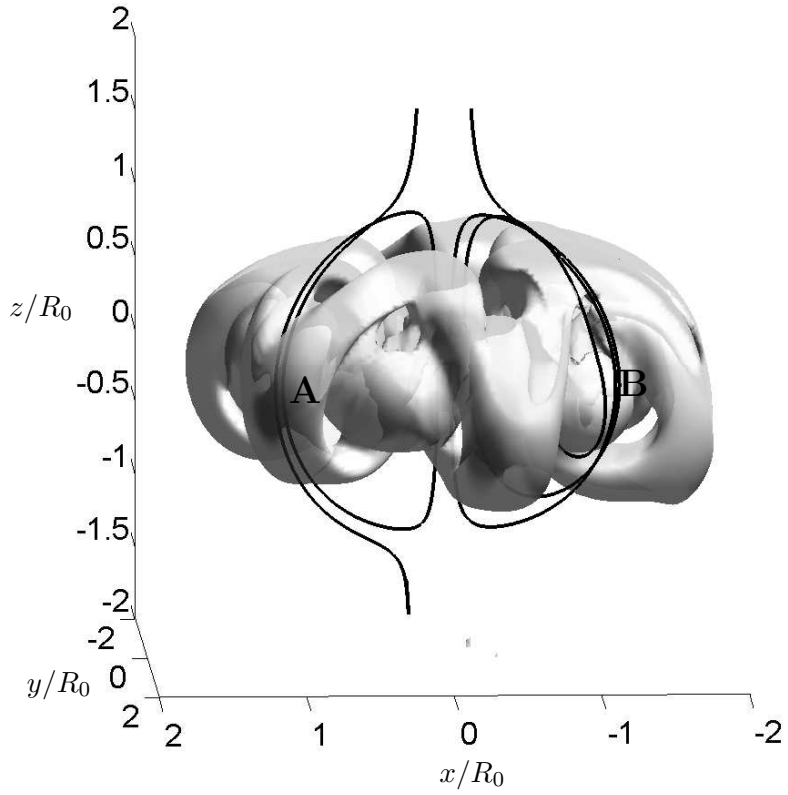

FIGURE 6.22: Transitional detrainment zones. Two particle pathlines were initiated on the $z/R_0 = 1.9$ plane at $r/R_0 = 0.25$ at time $(t - t^*)\Gamma_0/R_0^2 = 10$. A translucent isosurface of II with surface level $\mathrm{II}R_0^4/\Gamma_0^2 = -0.005$, at $(t - t^*)\Gamma_0/R_0^2 = 118$ is included to aid visualisation.

dynamics. It was necessary for Shadden *et al.* to use long integration times when constructing the LCS to reveal the ring's Lagrangian structure. This included part of the time immediately after the ring formation, thus the initial transient is likely to be captured within their results, leading to their observed lobe dynamics.

The laminar entrainment process, characterised by an axisymmetric Lagrangian surface, is significantly altered by the development of the azimuthal instability and associated secondary vortical structure. The first effect of the secondary structure is to deform the Lagrangian surface that defines the entrainment bubble into a wavy interface, which follows the shape of the secondary structure as shown in figure 6.21(a). The bubble deformation also changes the structure of the wake from a circular to a 'petal-like' cross-section at fixed z, with the individual petals corresponding to the azimuthal location of the peripheral secondary structure (figure 6.21(b)). This petal-like wake structure has been recently visualised in the experiments of Dazin *et al.* (2006*a*). As the secondary structure develops, the Lagrangian surface is folded to the extent that 'holes' are created through which

particles can detrain. The holes are located at points where the secondary loops meet in the outer periphery of the ring. This can be seen by comparing the two particle paths in figure 6.22, both of which were initiated at the same time and radial distance from the z-axis. Just before the onset of turbulence, fluid that is at location A detrains into the wake. Note also the slight drift in the left-hand-side particle around the azimuth of the ring. On the other hand, fluid that passes between the loops of the secondary structure, location B, continues to circulate within the entrainment bubble throughout the period of transition. After the onset of turbulence the ring continually sheds loops of vortical structure, carrying fluid (such as the right-hand-side particle) into the wake. This is the principle mechanism for turbulent detrainment.

6.5.5 Axial flow

We investigate the behaviour of the core region for the possibility of an axial flow being generated prior to the onset of turbulence. Recall that like Maxworthy (1977), we use the term axial flow to refer to circumferential flow along the axis of the vortex core.

The axial flow is analysed by calculating the Lagrangian paths of a number of fluid particles that are initiated within the core along radial lines that intersect the vortex centre at four azimuthal positions, labeled A B C and D in figure 6.23(a). The core centre was interpolated from the local velocity field and the Lagrangian pathlines were integrated from the start of the transitional phase to the onset of turbulence.

The thick-core ring (Case A1) shows negligible axial flow. Prior to the onset of turbulence, the particles orbit the core centre and drift through an angle of less than one degree along the circumferential axis of the core. However the thin-core ring (Case B3) shows a pronounced axial flow. Figures 6.23(a) and 6.23(b) present the particle paths during the early ($54.2 \leq (t - t^*)\Gamma_0/R_0^2 \leq 60.5$) and entire ($54.2 \leq (t - t^*)\Gamma_0/R_0^2 \leq 73.1$) transitional phase. During the laminar phase the particles simply orbit around the centre of the vortex core. However during the transitional phase the orbits begins to drift around the ring. The direction in which the particles drift depends on how close they are to the centre of the core. Constructive interference between the azimuthal modes causes a region of increased core stretching, labeled E in figure 6.23(b). The individual pathlines indicate an inner region of axial flow directed toward E (such that inner particles at A and B

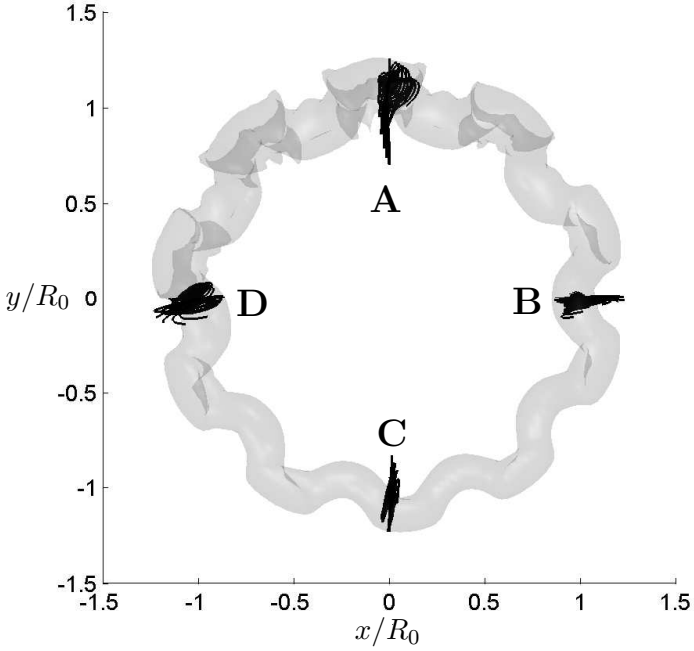

(a)

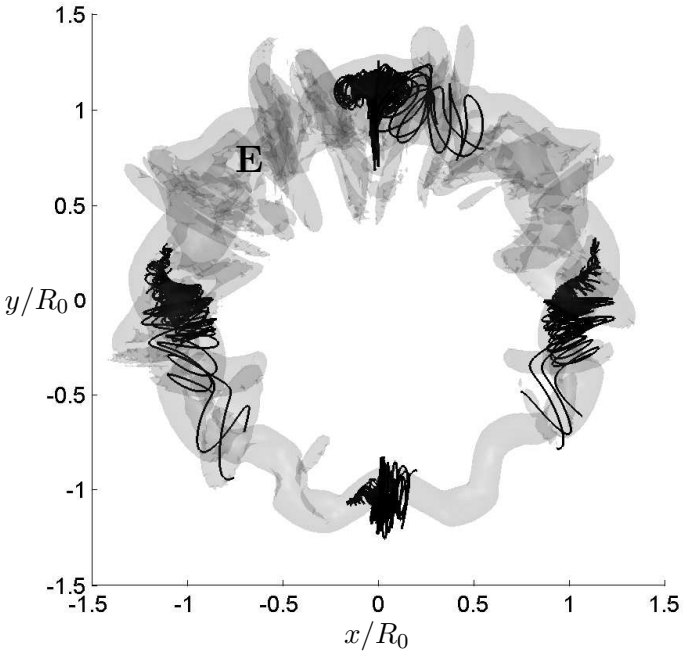

(b)

FIGURE 6.23: Axial core flow for thin-core ring case B3. (a) Lagrangian pathlines from time $(t - t^*)\Gamma_0/R_0^2 = 54.2 \rightarrow 60.5$ with translucent isosurface of $|\omega|\, R_0^2/\Gamma_0 = 3.0$ at $t = 60.5$. (b) Pathlines from time $(t-t^*)\Gamma_0/R_0^2 = 54.2 \rightarrow 73.1$ with translucent isosurface of $|\omega|\, R_0^2/\Gamma_0 = 3.0$ at $(t - t^*)\Gamma_0/R_0^2 = 73.1$.

move anti-clockwise and C and D move clockwise) and an outer region moving in the opposing direction. The axial flow in the inner core region is greatest at B, with particles translating 17° along the circumferential axis of the core during the transitional period. The radius of the inner core region is approximately $0.078R_0$ (27% of δ_θ at time $(t - t^*)\Gamma_0/R_0^2 = 54.2$). The inner core axial flow is maximum at the core centre and grows approximately exponentially with time.

This type of axial flow, showing a general drift of particles near the core centre toward point E of strongest instability development, is consistent with the $m = 1$ type axial flow recorded by Naitoh *et al.* (2002), in observations of rings generated through a circular orifice. They inferred that the axial flow was due to an azimuthal pressure gradient caused by preferential wave growth and associated core stretching. This is supported by our simulations as the thick-core ring undergoes near uniform wave growth leading to negligible axial flow and the thin-core ring experiences preferential wave growth leading to a pronounced axial flow. The thin-core ring would be expected to develop with less uniformity as a greater number of modes are excited by the linear instability leading to a larger $n = 1$ mode.

Chapter 7

Interaction of a vortex ring with an undisturbed free surface

In this chapter we focus upon the interaction of a vortex ring with an initially undisturbed free surface. We start by formulating the mathematical description of the problem in § 7.1 followed in § 7.2 by the numerical approach employed to simulate the interaction. In § 7.2.1 we describe the cases of interest and their run parameters. We then document a series of initial studies which were undertaken to assess the validity of our numerical techniques (§ 7.2.2). Finally we present and discuss the results examining in turn the laminar (§ 7.3), transitional (§ 7.4) and turbulent (§ 7.5) ring interactions, focusing on the ring dynamics, instability growth, vortex reconnection and the free surface response.

7.1 Mathematical Background

We consider a single vortex ring of radius R and core radius δ, with circulation Γ and Reynolds number $\mathrm{Re} \equiv \Gamma/\nu$, with impulse $\mathbf{P}$. The ring propagates vertically toward the free surface, with Froude number $\mathrm{Fr} = \Gamma/\sqrt{gR^3}$, in the z-direction with respect to Cartesian coordinates $\mathbf{x} = (x, y, z)$ and corresponding velocity components $\mathbf{u} = (u, v, w)$; see figure 6.1. The vortex is embedded at depth d_0 such that it is centred about $\mathbf{x} = (0, 0, d_0)$ at time $t = 0$ and initially propagates at a velocity U that depends on its instantaneous parameters, according to (6.9).

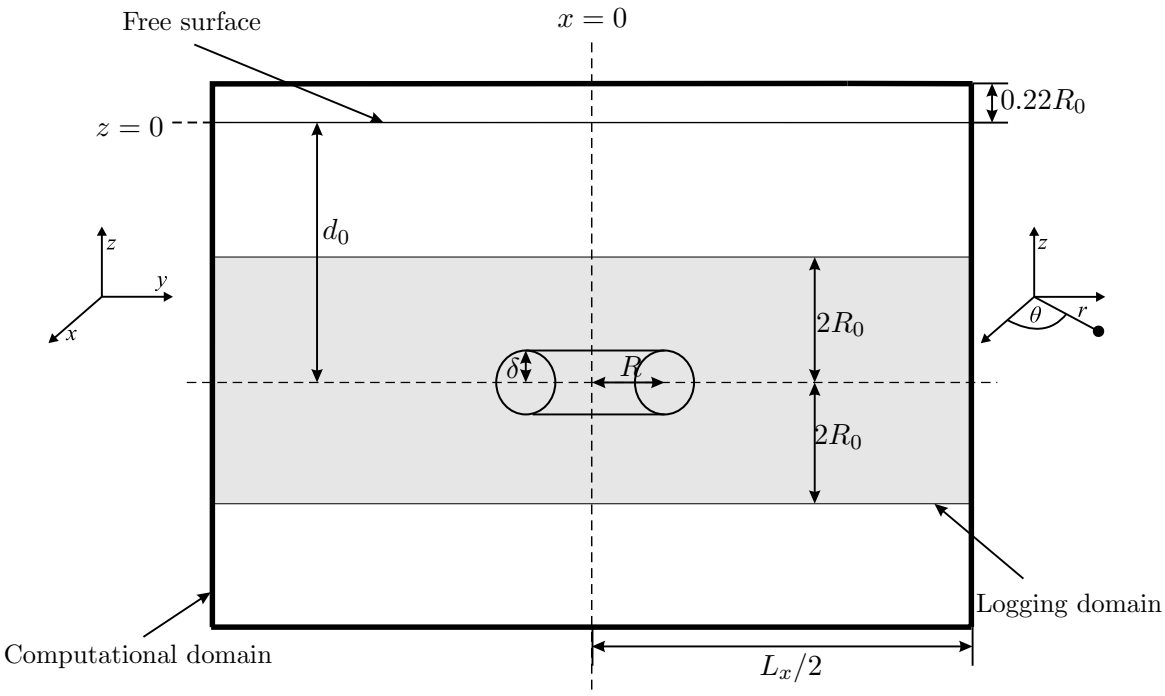

FIGURE 7.1: Schematic diagram of the normal vortex ring interaction with a free surface. The shaded region represents the co-moving logging domain, across which the ring integral measures are calculated.

7.2 Numerical approach

The Cartesian computational domain assumes periodic boundary conditions in the x- and y-directions, so that we are, in effect simulating an infinite array of rings. However, the domain widths L_x and L_y are chosen to be sufficiently large such that the propagation of the ring toward the surface and subsequent expansion is not affected greatly by the periodic images. Following the domain sensitivity study § 6.4.2, we require that the ring does not encroach within three ring radii of the lateral boundaries during its approach to the surface. At small depths the ring dynamics are dominated by its virtual image above the surface, which induces a radial expansion of the ring. To prevent the periodic rings, implied by the lateral periodic boundary conditions, from influencing the dynamics of the expanding ring we also ensure that it does not move within three ring depths of the lateral domain limits. For cases where Froude number approaches zero we impose impermeable free-slip boundary conditions on the upper ($z = 0$) boundary and simulate the interaction using the fixed-boundary code described in § 4.2. For cases with finite Froude number, we impose free-surface boundary conditions (§ 4.3.1) on the upper ($z = 0$) boundary and simulate the interaction with the free-surface code described in § 4.3. For both codes, impermeable free-slip boundary conditions are imposed

on the bottom plane of the z-axis. The initial velocity field is prescribed by embedding vortex rings which have been aged within an unbounded domain for a given time period t_e, following the method described in § 5.2.1

Since the ring expands as it approaches the surface (Song *et al.*, 1992) the core region is increasingly stretched with time. Under the assumption of conservation of circulation and in the absence of viscosity, one would expect the volume of the core to be conserved (Fukumoto, 2003), with

$$\delta^2 R = \delta_0^2 R_0, \tag{7.1}$$

where a zero subscript indicates an initial value. Viscosity diffuses the core slowly with time and circulation is shed into the wake, but we can thus expect δ to approximately decrease in proportion to $\sqrt{R}$. To maintain resolution as the core stretches, the flow field is interpolated at discrete intervals onto progressively finer grids. This requires that cells at the bottom of the domain (far from the ring), which have very small effect on the dynamics of the ring, are removed or 'trimmed' to avoid excessively large computations. In cases where Froude number approaches zero the bottom cells are trimmed during the interpolation routine. For simulations with finite Froude numbers, the trimming occurs during the simulation every time the ring propagates a distance $\tilde{d} = 0.11R_0$ in either the radial or the z-directions. The continuous trimming is required to avoid the generation of a transient surface wave which is introduced if the reduction to the z-axis is too large; see § 7.2.2.

Interpolation of the flow is performed in all three directions. In the x- and y-directions a Fourier scheme is employed, however, this high-order method cannot be implemented in the z-direction due to the non periodic boundary conditions. Instead a third-order polynomial interpolation scheme is employed. Fourier interpolation is also not suitable in lateral planes near the free surface that feature air/water discontinuities induced by large surface displacement. In such planes the polynomial interpolation scheme is used to avoid Gibb's phenomena. The quality of the interpolation and trimming routines is examined below.

The ring circulation, impulse and radial measures are defined in § 6.1 and are calculated in a co-moving cubic logging domain whose top and bottom is $2R_0$ from the ring centre of enstrophy; see figure 7.1. The logging domain moves with the ring so that the wake is left behind and does not contribute to the integral ring measures. Differencing neighbouring cells which span the surface would lead to the summation of 'artificial' vorticity in the integral ring measures as $\mathbf{u} = 0$ in cells

Case	δ_0/R_0	Fr	Re	t_e	Γ_0	R_0
F1	0.326	0	4988	40	0.907	1.145
F2	0.228	0	7440	40	0.992	1.048
D1	0.326	0.3	4988	40	0.907	1.145
D2	0.326	0.6	4988	40	0.907	1.145
D3	0.341	0.3	4576	130	0.832	1.195
D4	0.466	0.3	4400	180	0.800	1.148

TABLE 7.1: Ring parameters for the initially undisturbed surface interaction cases. Note $R_0 = R_\Omega$. t_e is the time that the ring has been evolved in an unbounded domain, normalised by its relevant initial parameters, see § 6.3.

Case	$N_x \times N_y \times N_z$	$L_x/R_0 \times L_y/R_0 \times L_z/R_0$	d_0/R_0	I_f	I_R
F1	384×384×224	$10.48 \times 10.48 \times 6.11$	3.06	1.5	$1.2R_0$
F2	384×384×256	$11.45 \times 11.45 \times 7.63$	3.82	see text	see text
D1	384×384×224	$10.48 \times 10.48 \times 6.11$	3.3	1.5	$1.5R_0$
D1	354×354×192	$11.53 \times 11.53 \times 6.29$	3.3	1.5	$1.5R_0$
D3	384×384×224	$10.04 \times 10.04 \times 5.86$	3.3	1.5	$1.2R_0$
D4	336×336×224	$8.9 \times 8.9 \times 5.99$	3.21	1.5	$1.2R_0$

TABLE 7.2: Domain sizes for the initially undisturbed surface interaction cases. Box dimensions are at the start of the simulation. Cases D1-4 also initially include 8 passive cells to capture surface displacement (see 7.1). Cells interpolated by interpolation factor I_f when ring radius exceeds I_R. Case F2 features multiple interpolations and is described in the text.

above the surface. Thus only the contribution of cells below the surface is included within the ring measures. Likewise to exclude the contribution of opposite-signed vorticity, generated due to surface curvature, only cells where $\omega_\theta \geq 0.0$ are included within the ring measures.

7.2.1 Simulation Parameters

The cases, shown in tables 7.1 and 7.2, allow us to investigate the effects of Froude number and ring age on the surface interaction. The 'F' and 'D' case labels refer to simulations performed by the fixed-boundary and deformable free-surface codes respectively. Cases F1, D1 and D2 are identical thick-core laminar rings at three

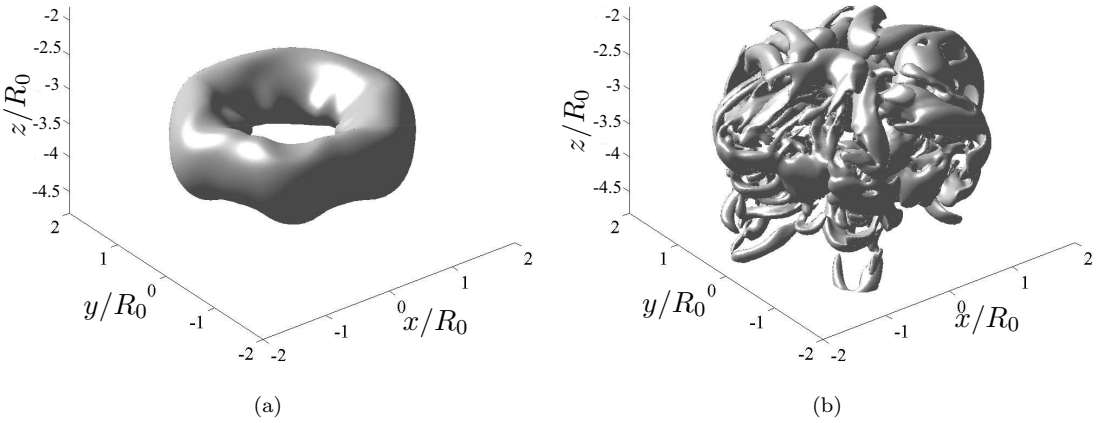

FIGURE 7.2: Ring structure of Cases (a) D3 (transitional) and and (b) D4 (turbulent) at the time of embedding. Ring structure is visualised with an isosurface of $\mathrm{II}R_0^4/\Gamma_0^2 = -0.05$.

different Froude numbers. The rings were aged for the duration of the equilibration phase in the unbounded domain, thus the initial vorticity shed as the ring relaxes to its steady state profile had left the domain. Case F2 features a thin-core ring with a high Reynolds number to maintain the slenderness of the core. To ensure adequate resolution of the core region the domain was interpolated onto finer grids, sequentially, by factors 1.5, 1.3333, 1.5, and 1.5 after the ring had expanded to $1.2R_0, 1.8R_0, 2.25R_0, 3.375R_0$ respectively. At each interpolation, the number of cells in the z direction N_z was reduced by 50%, 50%, 33.3333% and 66.6666% respectively. By interpolating the flow field on multiple occasions it was possible to maintain the core resolution as the ring expanded to $4.9R_0$, allowing us to investigate the ring instability. Cases D3 and D4 feature thick-core rings that have been aged for a greater time period in the unbounded domain. For Case D3 the Widnall instability has developed, distorting the core into a six azimuthal wave pattern, the secondary looping structure had just begun to develop and the ring can be considered to be in the transitional regime; see figure 7.2(a). In Case D4 the core has just become locally turbulent; see figure 7.2(b). The same nondimensionalisation as for the unbounded investigation is used, except, we now nondimensionalise lengths by R_Ω, for ease of comparison with experimental studies. Experimentalists judge ring radius as the distance from the ring centreline to the core centre, which is closely approximated by R_Ω. The initial values, which we use for nondimensionalisations, are recorded at the time of embedding and are shown in table 7.1.

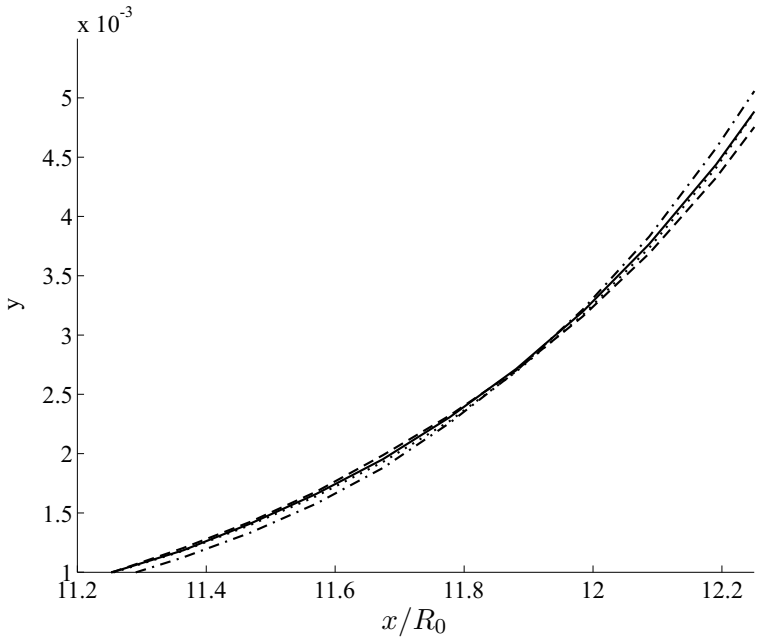

FIGURE 7.3: Comparison of surface elevation at the centre ($\mathbf{x} = [0, 0, h]$) for Case D1 with different trim lengths $\tilde{d}_{max}$: — , $\tilde{d} = 0.11R_0$; · · · , $\tilde{d} = 0.22R_0$; – – – , $\tilde{d} = 0.33R_0$; and – · – , $\tilde{d} = 0.55R_0$.

7.2.2 Assessment of the numerical approach

The same cell resolution was employed as in the unbounded simulations as it has been shown in § 6.4.1 to provide a high degree of accuracy. The sensitivity of free-surface simulations to the choice of the trimming length $\tilde{d}$ was investigated by repeating Case D1 with various magnitudes of $\tilde{d}$. By trimming cells from the z-axis we are modifying the flow field near the bottom of the domain. Since the ring is far from the boundary its dynamics are unaffected, however the code corrects the flow field by imposing continuity (4.7), thus the pressure in the following time step contains an error which is distributed throughout the domain. A sudden change in pressure at the surface causes a wave to be generated which then propagates with wavelength of the box width around the periodic domain. If the trim is sufficiently small, the pressure correction and resulting surface wave are negligible. Figure 7.3 shows the effect of $\tilde{d}$ on the free surface elevation at the centre $\mathbf{x} = (0, 0, h)$. If $\tilde{d}$ is large a small surface oscillation is formed but vanishes as $\tilde{d}$ falls below $0.22R_0$, significantly greater than our chosen value.

The validity of the interpolation procedure was checked through repetition of Case D1 with a constant domain, neither trimmed nor interpolated. The ring radius, depth, velocity and core thickness are relatively unaffected (<1%), how-

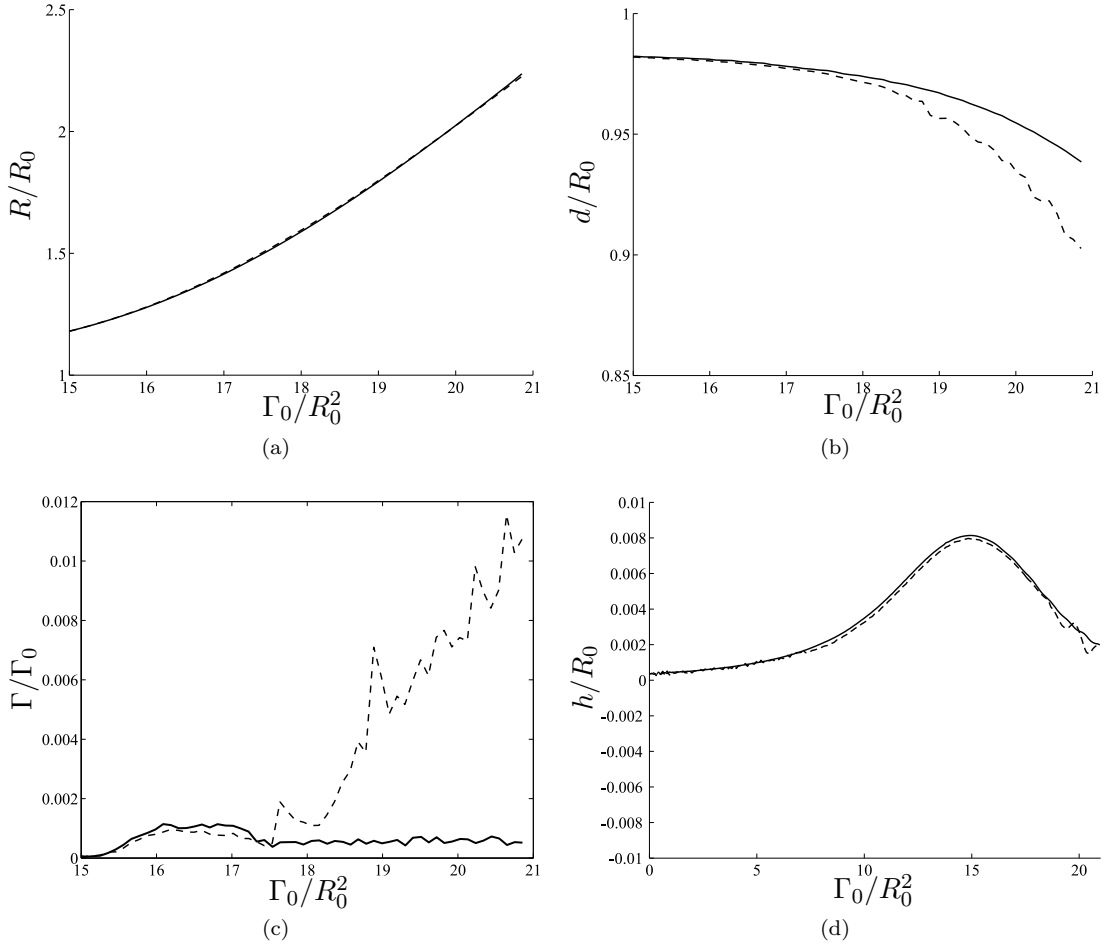

FIGURE 7.4: A comparison of results from a trimmed and interpolated simulation – – – to a domain with constant box geometry — for Case D1. Subfigures compare: (a) Ring radius; (b) Ring circulation; (c) Circulation of opposite-signed surface vorticity; (d) Elevation at the centre of the surface.

ever, after interpolating the field (when $R > 1.5R_0$) the ring circulation decays faster for the interpolated ring; see figure 7.4(b). The difference can be explained by analysing the surface vorticity field. Case D1 has a low Froude number and thus while the ring expands it forms only a small depression on the surface above. The resulting surface curvature generates a small region of opposite-signed vorticity (Longuet-Higgins, 1998). The opposite-signed surface vorticity cancels with that of the primary ring, reducing its circulation. This is not well captured by the coarse uninterpolated simulation (see figure 7.4(c)) leading to higher ring circulation. One consequence of interpolating the flow field is the initiation of a small surface oscillation (figure 7.9(c)). The transient is likely to be caused by errors in the interpolated flow field close to the surface. It is small compared to the maximum surface elevation (<8%) and tiny compared to the ring radius (< 0.04%),

thus it has little effect on the dynamics of the ring.

Further confidence in the numerical approach was gained through simulation and comparison with previous experimental and numerical work. The orthognal interaction of a ring with a free surface was assessed through comparison with the low Froude and Reynolds number experiment of Song *et al.* (1992). A ring was embedded in a computational domain of $L_x = L_y = 11.5R_0$ and $L_z = 5.75R_0$ including $0.24R_0$ of cells above the free surface to allow for surface displacement. Initially, the simulation featured $N_x = N_y = 384$ grid cells in the x- and y-planes, and $N_z = 200$ cells in the z-plane, but was interpolated when $R_\Omega = 1.2R_0$. Prior to embedding, the ring was evolved for 25 non-dimensional time units in an unbounded domain, sufficient for the ring to adjust to its steady-state core profile and for its initial start-up wake to be flushed from the domain. At the time of embedding, $R_\Omega = R_0 = 1.044$, $\Gamma = \Gamma_0 = 0.994$, Re = 10000, Fr = 0.287, $\delta_\theta = 0.218$ and depth $d = 2.84R_0$. These parameters matched closely those of Song *et al.* (1992), with the exception of Reynolds number which was lowered from 15100 to 10000 to stabilise the surface interaction. Lowering the Reynolds number causes a slightly lower instability growth rate and less core diffusion, but since the surface interaction lasts for a short time the differences are small. We specify a time t_d, at which the ring had propagated to a depth $d = 2.5R_0$, to compare our results with Song *et al.* (1992), who commenced their readings at this depth.

Good quantitative agreement is shown between the results for both ring depth and radial expansion over the duration of the simulation (see figure 7.5). The experimental ring propagated under the surface to a radial expansion of $4.2R_0$ at which point the vortex ring reconnected with the free surface. In order to maintain adequate resolution of the core it could not be simulated past $2.25R_0$; consideration of later times awaits further interpolation and code parallelisation. If our simulation had been continued without further interpolation, the core would eventually break down into small grid-scale vortical structures. This causes excessive surface displacement, violating the boundary restriction (4.8) and terminating the simulation.

Similar surface features were also present in the DNS and experiment. Initially the surface was deformed into a central bulge which grew with time as the ring depth decreased (figure 7.6(a)). As the ring radius expanded close to the surface a circular depression forms above and outboard of the ring (figure 7.6(b)).

Lack of resolution restricts further computation and thus we could not simulate the ring through to the stage of reconnection. A further test was performed to

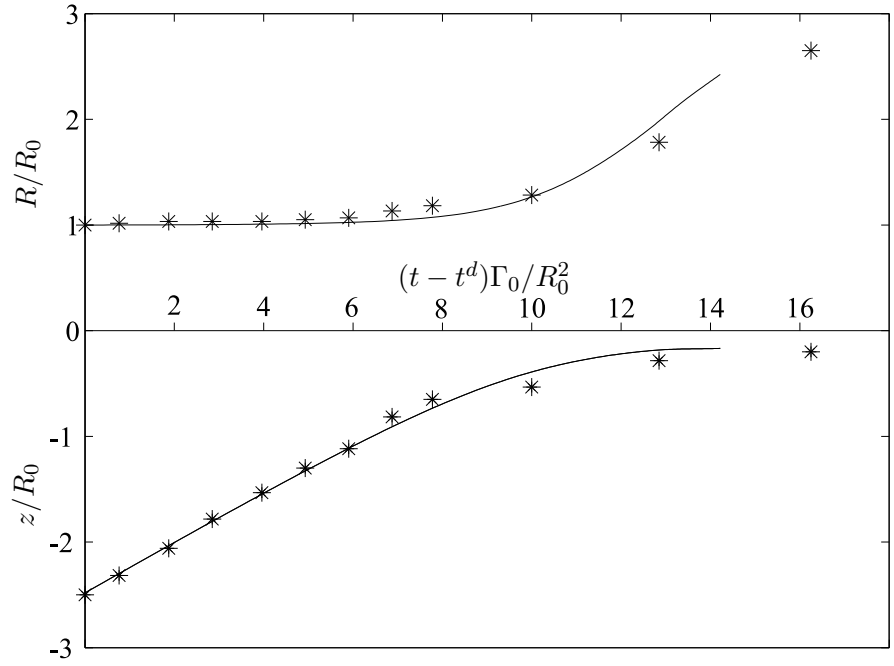

FIGURE 7.5: Comparison of ring depth and radial expansion: — , DNS; and $***$, experiment of Song *et al.* (1992).

show that the code is capable of capturing reconnection at the surface. The case of the oblique interaction of a vortex ring with a free surface was undertaken, as reconnection was observed in the experiments of Gharib & Wiegand (1996) and the numerical simulations of Zhang *et al.* (1999). A ring was initiated at depth $d_0 = 1.57R_0$ with its angle of propagation inclined at 10° above the horizontal plane toward the free surface. The study was performed before the conception of initialisation method III, thus initialisation method II was used to prescribe the initial velocity field. The intended ring parameters were radius $R_0 = 1.0$, core radius, $\delta = 0.35$, Reynolds number Re = 1570 and Froude number Fr = 0.47 to match a numerical simulation of Zhang *et al.* (1999). However, due to the limitations of the initialisation method (see § 5.1.2) the actual core size and circulation differed greatly. The domain had widths of $L_x = L_y = 8R_0$ and height $L_z = 4.25$ including $0.25R_0$ of cells above the free surface to allow for surface displacement. The number of grid cells in the lateral directions were $N_x = N_y = 256$, and $N_z = 136$ in the vertical.

Figure 7.7 shows good qualitative agreement with the numerical simulations of Zhang *et al.* (1999). As the ring propagates toward the surface it begins to reconnect toward the rear of the core, producing a U-shaped vorticity filament, as

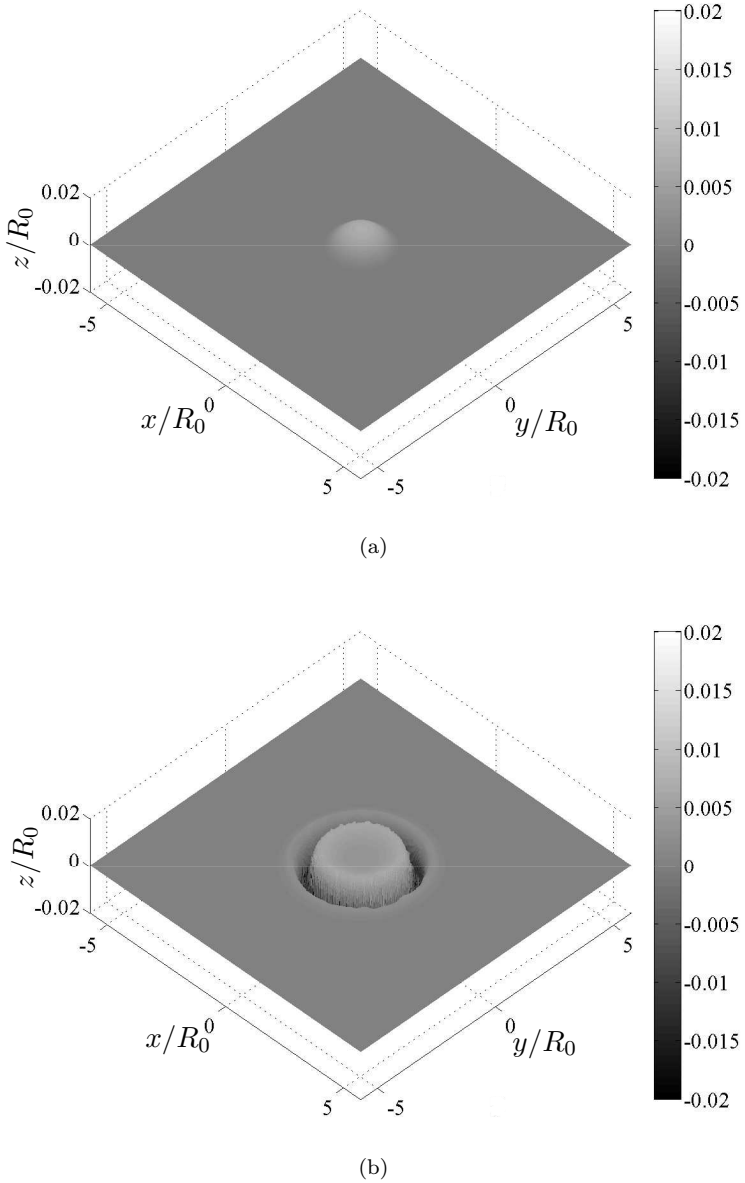

FIGURE 7.6: Free surface displacement at various times: (a) $(t-t_e)\Gamma_0/R_0^2 = 9.0$; (b) $(t-t_e)\Gamma_0/R_0^2 = 13.0$.

reported in all the relevant literature. The surface normal vorticity profile at the reconnection site is very similar in shape to that of Ohring & Lugt (1996). The reconnected ends of the U-shaped filament then move apart and the tail moves toward the surface as shown in figures 7.7(e) and 7.7(f). These results show that the free surface code is capable of modeling surface reconnections if the required resolution is present.

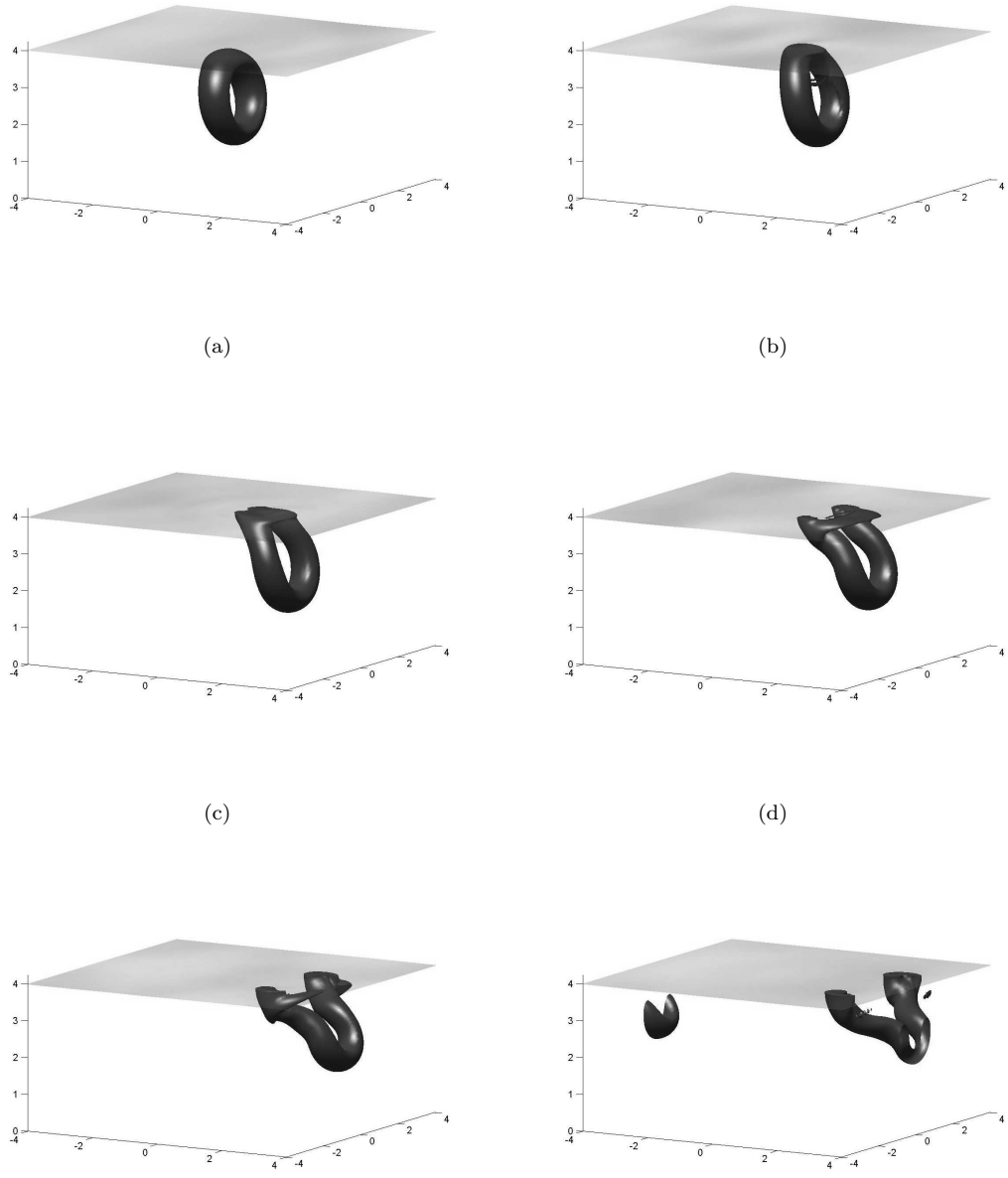

(a) (b)

(c) (d)

(e) (f)

FIGURE 7.7: Interaction of a vortex ring propagating at an angle of 10° toward a free surface. Vortical structure visualised by an isosurface of vorticity magnitude, $|\omega| = 0.25\,|\omega|_0^{max}$ at times: (a) $(t-t_e)\Gamma_0/R_0^2 = 6$; (b) $(t-t_e)\Gamma_0/R_0^2 = 12$; (c) $(t-t_e)\Gamma_0/R_0^2 = 18$; (d) $(t-t_e)\Gamma_0/R_0^2 = 24$; (e) $(t-t_e)\Gamma_0/R_0^2 = 30$; (f) $(t-t_e)\Gamma_0/R_0^2 = 36$.

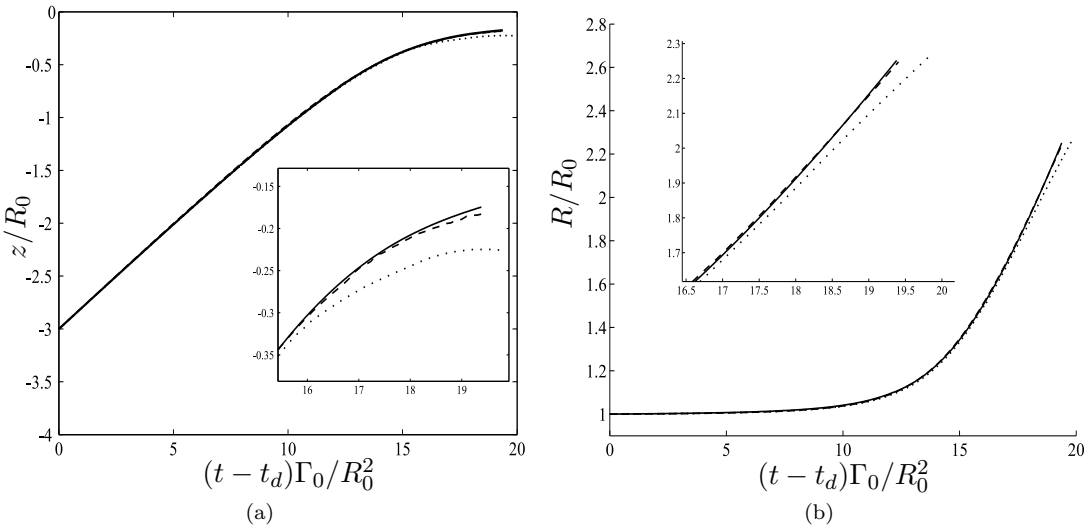

FIGURE 7.8: Comparison of ring depth (a) and radius (b) against time for a range of Froude numbers: — , Fr = 0; – – – , Fr = 0.3; · · · , Fr = 0.6. Subplots show the ring behaviour close to the surface.

7.3 Results

7.3.1 Laminar ring interaction

The variation of depth and radius of laminar rings of differing Froude number is shown in figure 7.8. As the rings approach a depth of approximately $1R_0$ they all follow the same trajectory. This result is expected, since the Froude number only affects the ring close to the surface (Song *et al.*, 1992). It is nevertheless important as it shows agreement between the two numerical codes. The ring flow field causes a bulge to form at the centre of the surface, which grows as the ring moves closer, as shown in figures 7.9(a) and 7.9(c). The magnitude of the surface displacement is a function of the Froude number. For Case D1, where Fr = 0.3, the centre of the surface reaches a maximum elevation $h_{max} = 0.00815R_0$, whereas for a higher Froude number, Case D2 (Fr = 0.6), $h_{max} = 0.0326R_0$. Surface displacement is proportional to the square of the Froude number, which is expected, since $h \propto g^{-1}$ (5.7) and g appears in the Froude number as $g^{-1/2}$. At this stage, the vorticity distribution in the core is similar to that of an unbounded ring (figure 6.6).

As the ring moves up to a depth of approximately one radius it begins to interact with its virtual image above the surface and expands radially (figure 7.8). The initial bulge drops and a surface depression forms above and just outboard of the ring (see figures 7.9(b) and 7.10(b)). The depth at which the ring expands

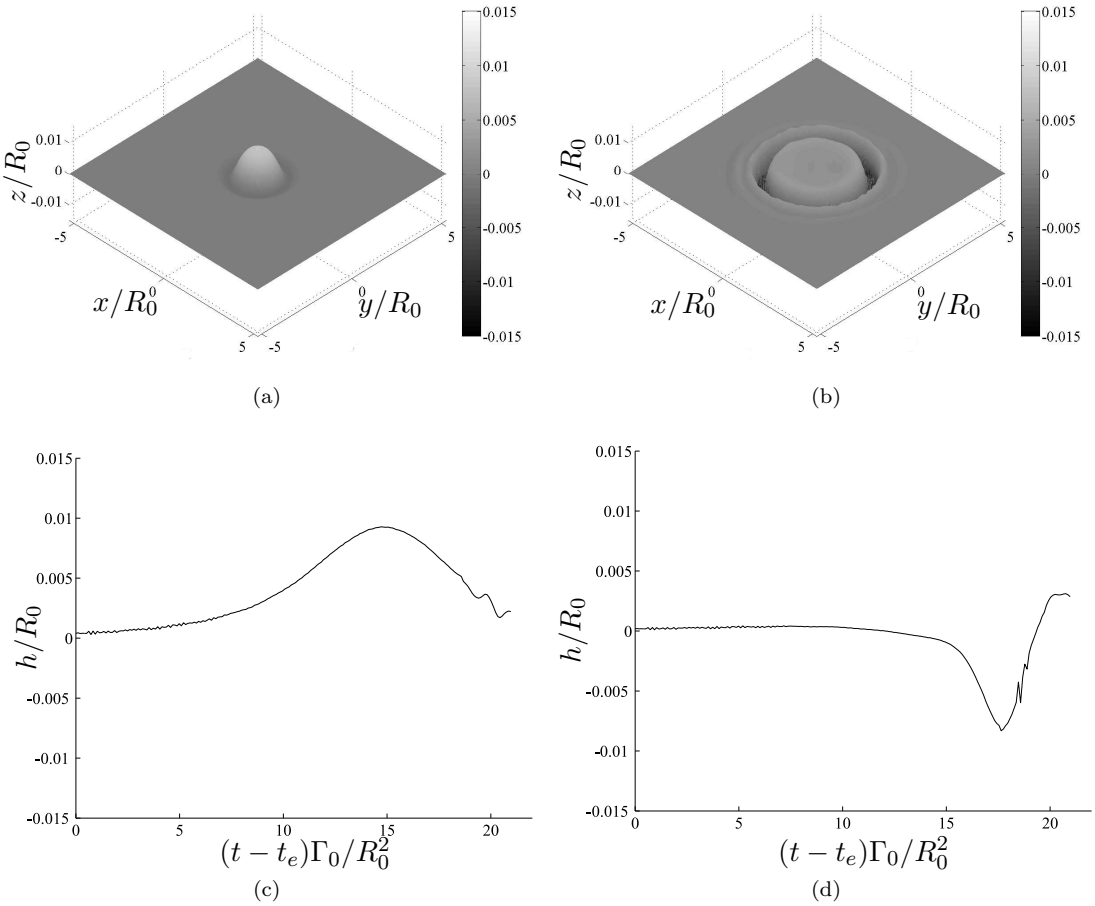

FIGURE 7.9: Surface displacement for laminar rings: Surface elevation field at (a) $(t-t_e)\Gamma_0/R_0^2 = 14.52$ and (b) $(t-t_e)\Gamma_0/R_0^2 = 20.75$; Surface elevation as a function of time for (c) the centre of the surface ($\mathbf{x} = [0, 0, h]$) and (d) $1.75R_0$ from the centre ($\mathbf{x} = [0, 1.75R_0, h]$)

is dependent on Froude number (see subplot in figure 7.8(a)). Case D2 expands radially further from the surface than the lower Froude number cases, consistent with the experiments of Song *et al.* (1992). The increased depth cannot be attributed solely to the deeper surface depression, as the difference in ring depths is greater than the difference in surface displacement (see figure 7.10). Surface curvature results in the generation of opposite-signed vorticity, which forms a secondary ring outboard of the primary ring (see figure 7.10). The secondary ring is far more intense in Case D2, 17.8% of the primary ring circulation compared to 1.4% for Case D1 (figure 7.11), due to the increased surface curvature, and induces a downward impulse on the primary ring leading to the ring expanding radially at a greater depth.

Figure 7.11 shows the evolution of the total circulation and the contribution of the

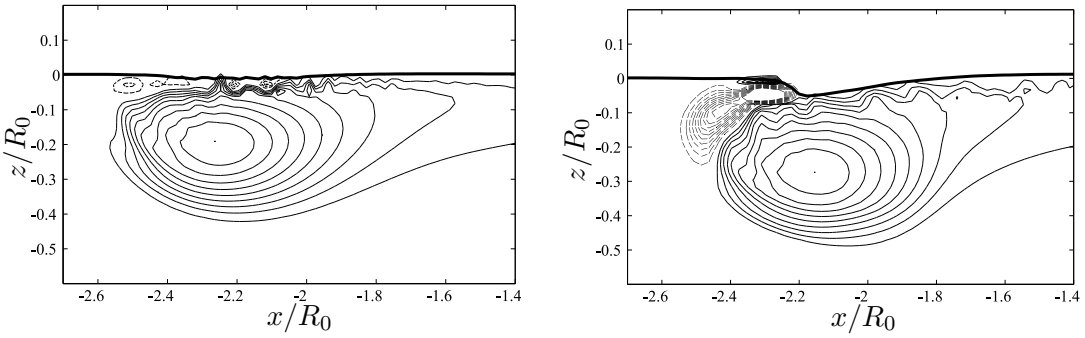

FIGURE 7.10: Surface vorticity generation for laminar rings at $(t-t_e)\Gamma_0/R_0^2 = 20.75$: (a) Case D1; (b) Case D2. — and – – – contours represent positive (ring) and negative (surface) vorticity at increments of $\omega_{max}/10$.

opposite-signed vorticity. As the ring propagates toward the surface the total circulation decays slightly because vorticity in the wake leaves the co-moving logging domain (see figure 7.11). As the ring moves closer to the surface ($(t-t_d)\Gamma_0/R_0^2 \approx 14$) the total circulation (thick lines in figure 7.11) starts to decay at a faster rate as opposite-signed vorticity adds a negative circulation component (thin lines in figure 7.11). The decay rate is far greater for Case D2 as it generates more oppositely signed vorticity due to its higher Froude number. For the Fr = 0 cases (F1 and F2) the decay rate of total circulation also increases slightly, dispite the absence of surface curvature and opposite-signed vorticity, due to a separate mechanism. When the ring is at very small depths the tail of its vorticity profile touches the surface and is canceled by its virtual image above the surface. Effectively this produces a vorticity sink at the surface reducing the ring circulation.

As the ring expands parallel to the surface, the distribution of vorticity in the core is modified from its unbounded profile. The distribution of vorticity becomes stretched in the horizontal direction (figure 7.12(a)) and forms a wake of weak vorticity, just as the unbounded ring does, but in the horizontal plane close to the surface. In the vertical direction the distribution of vorticity is far narrower and more Gaussian like (figure 7.12(b)). Figures 7.12(a) and 7.12(b) show the distribution of ω_θ in horizontal and vertical directions through the core centre. Consequentially the wake is less apparent in the horizontal profile for Case D2 as it lies on a horizontal plane that is closer to the surface than the core. Opposite-signed vorticity is evident in both the horizontal and vertical core profiles for Case D2 (see figure 7.12) revealing that the secondary vorticity wraps around the primary ring. For Case D1 the opposite-signed vorticity is only revealed in

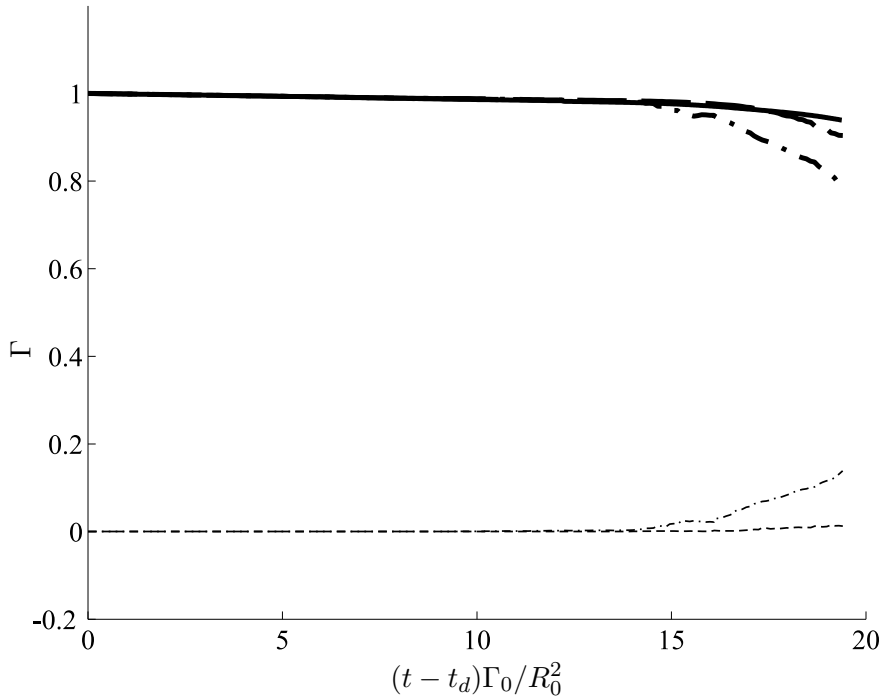

FIGURE 7.11: Evolution of total circulation for cases with differing Froude number: — , Fr = 0; – – – , Fr = 0.3; – · – , Fr = 0.6 (laminar cases). Thick lines denote total circulation, thin lines denote the contribution from opposite-signed vorticity generated at the surface due to surface curvature.

the vertical profile close to the surface. It is noted, for the low Froude number case, that a region of isolated grid-scale vorticity exists directly below the surface (revealed in the vorticity contours of figure 7.10(a)) resulting from small localised movements in the surface. Since the vorticity is tiny compared to the ring it does not affect its motion below the surface.

7.3.2 Instability growth

Case F2, which features a thin core at Fr = 0, was interpolated a number of times, allowing the ring to be simulated to a greater radial expansion. Prior to embedding, Case F2 was evolved for 40 time units in an unbounded domain. The ring had thus already begun to develop the Widnall instability. Although in the early stages, and not yet visible in isosurface plots of ω or II, an azimuthal modal decomposition (following the method layed out in § 6.5.2) reveals that $n = 10$ and $n = 11$ are the most unstable modes at the time of embedding; see figure 7.13(a). Cross referencing figures 7.13(a) and (7.13(b)), we see that as the ring propagates toward a depth of approximately one radius, modes 9, 10 and 11 are amplified

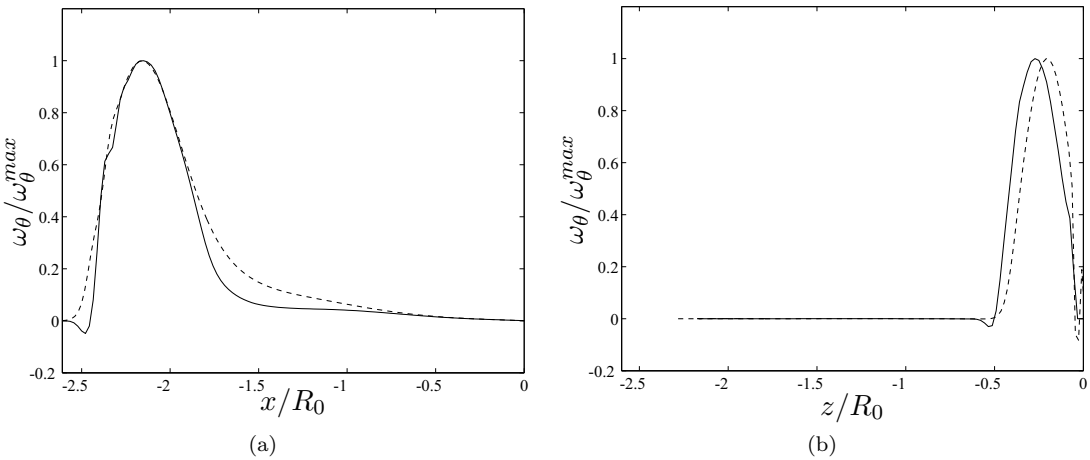

FIGURE 7.12: Comparison of the distribution of ω_θ through the centre of the core in the (a) x- and (b) z-directions for Cases – – – , D1 and — , D2 at $(t-t_e)\Gamma_0/R_0^2 = 20.34$ and $(t-t_e)\Gamma_0/R_0^2 = 20.75$ respectively.

due to the Widnall instability. Between times $(t-t_e)\Gamma_0/R_0^2 = 14 \rightarrow 19$ the ring expands radially, and the modes decay with the exception of $n = 1$ which continues to amplify. The modal decay continues until the ring approaches $R \approx 2R_0$ at which point the ring is very close to the surface. Only selected modes are plotted in figure 7.13(a) for clarity, but as the ring continues to expand radially, all modes amplify with a similar growth rate, except for $n = 1$ and $n = 22$ whose growth rates are affected by nonlinear modal interactions.

The amplification of a broad spectrum of modes can be explained by examining the linear stability results of Crow (1970). The radial expansion causes the ring curvature to decrease, thus locally the core and its image begin to approximate line vortices. Crow (1970) showed that for line vortices, the instability wavelength, growth rate and perturbation angle were a function of $\widehat{d}/\widehat{k}$ (see § 2.2.1). In our case, the close proximity of the core to the surface means that the vortex spacing b is of order the core diameter D, hence $D/b \approx 1$ and $\widehat{d}/\widehat{k} \approx 0.3210$ follows from (2.5). For $\widehat{d}/\widehat{k} \approx 0.3210$ figures 10, 11 and 12 in Crow (1970) give the most amplified wavenumber $k_{max} = 1.25$, maximum amplification rate $\alpha_{max} = 0.78$ and a planar angle of maximum amplification of 42°.

In the example of the line vortices there is no stretching of the vortex filaments and the most amplified mode n_{max} corresponding to k_{max} remains constant with time. For the case of a vortex ring n_{max} is the integer number of waves of wavelength

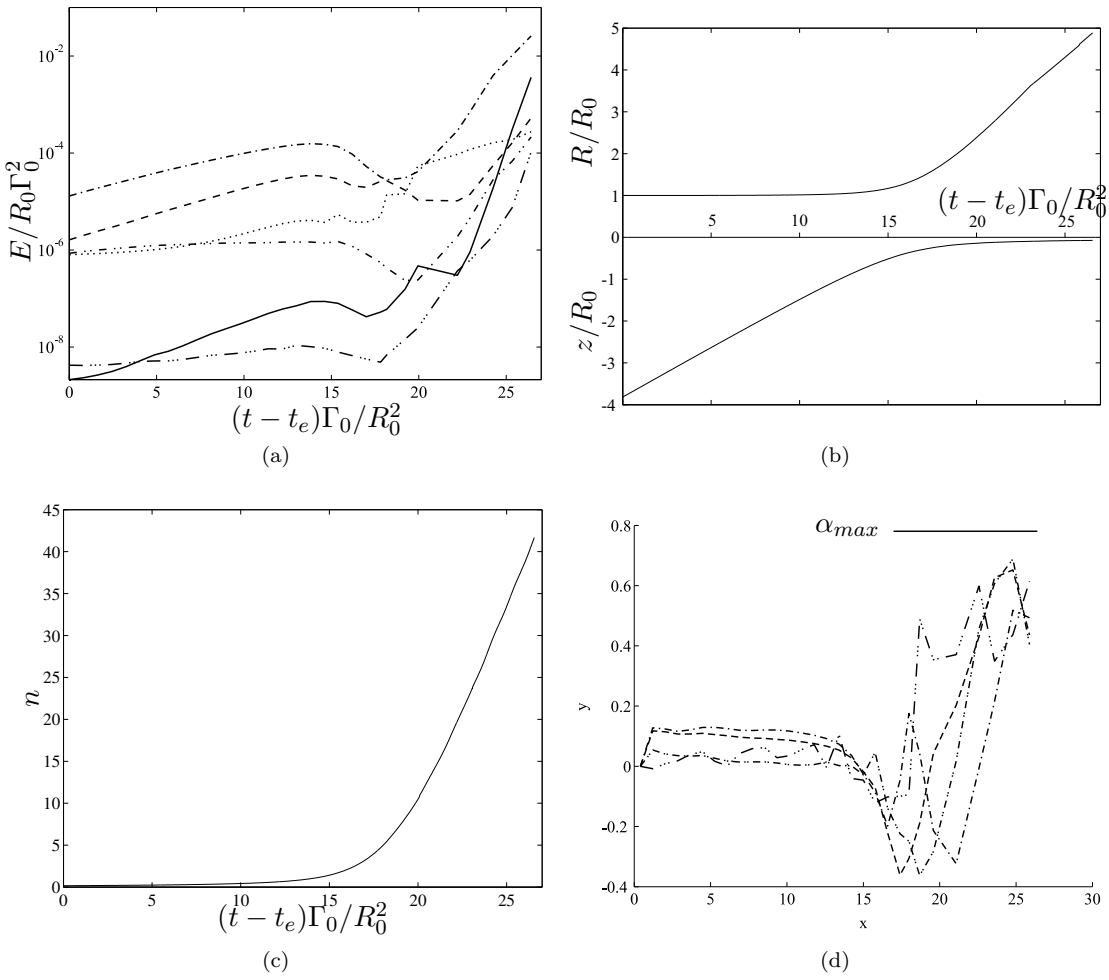

FIGURE 7.13: Instability development for Case F2: (a) Evolution of selected azimuthal modal energies: · · · , $n = 1$; – – – , $n = 10$; – · – , $n = 11$; – · · – , $n = 12$; — , $n = 22$; – · · · · – , $n = 23$; (b) Change in ring radius and depth with time; (c) Most amplified mode predicted by the stability analysis of Crow (1970); (d) Modal growth rates: same line styles as subfigure(a); — denotes $\alpha_{max} = 0.78$ (Crow, 1970).

λ_{max} that can fit around the ring circumference, thus

$$n_{max} = (2\pi R)\,/\lambda_{max}, \tag{7.2}$$

where $\lambda_{max} = (2\pi b/k_{max})$ and the vortex separation b is approximated as twice the depth. However, since the ring circumference increases as it expands below the surface the circumference increases one would expect n_{max} to increase correspondingly (see figure 7.13(c)). The rapidly changing n_{max} appears to contradict the broadband modal amplification shown in figure 7.13(a). However, analysing figures 6 and 9 in Crow (1970) for the case where $\widehat{d}/\widehat{k} = 0.3210$, reveals that a broad range of wavenumbers (and corresponding wavelengths) are unstable, all

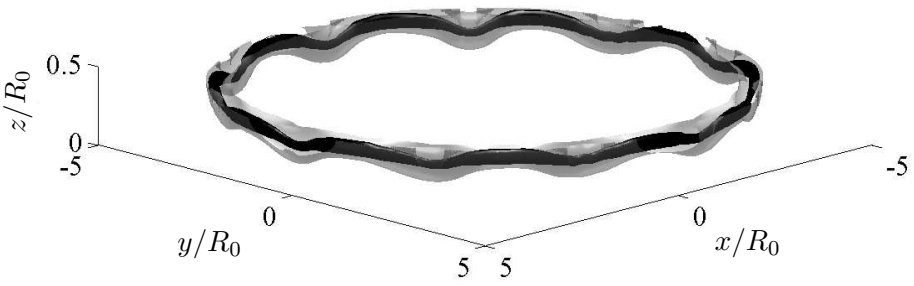

FIGURE 7.14: Development of the Crow instability for Case F2 at time $(t - t_e)\Gamma_0/R_0^2 = 26.6$ visualised by two isosurfaces of $|\omega|$. Dark and light surfaces correspond to $|\omega|\, R_0^2/\Gamma_0 = 14$ and $|\omega|\, R_0^2/\Gamma_0 = 2$ respectively.

with similar amplification rates. Thus although the most amplified azimuthal wavenumber changes rapidly with time, a broad range of modes are similarly amplified leading to the observed broadband modal growth. Figure 7.13(d) shows good agreement between our modal growth rates and the theoretical prediction $\alpha_{max} = 0.78$ (Crow, 1970). Our modal growth rates are all slightly below the maximum theoretical value. Note $n = 1$ and $n = 22$ are not plotted as their growth rate is the product of nonlinear interactions between modes.

In the later stages of the simulation the most unstable mode, $n = 11$, and its higher harmonic, $n = 22$, are greatly elevated above the rest of the modes (7.13(a)). This results in near uniform wave growth around the circumference of the ring (figure 7.14) and a correspondingly small $n = 1$ mode. This contrasts greatly to the modal development of the unbounded ring as the Widnall instability excites a narrow band of modes whose nonlinear interactions lead to a large $n = 1$ mode. The selection of a dominant single mode is consistent with the experiments of both Song *et al.* (1992) and Lim & Nickels (1992).

7.4 The surface interaction of transitional rings

As discussed in § 6.5.3 the transitional phase is marked by the reorganisation of the outer core into a series of counter rotating loops which encompass the sinusoidally deformed inner core. The secondary structure is at the early stages of its evolution at the time of embedding (figure 7.2(a)). As the ring propagates toward the surface, the loops develop as the inner core distortion intensifies due to the Widnall

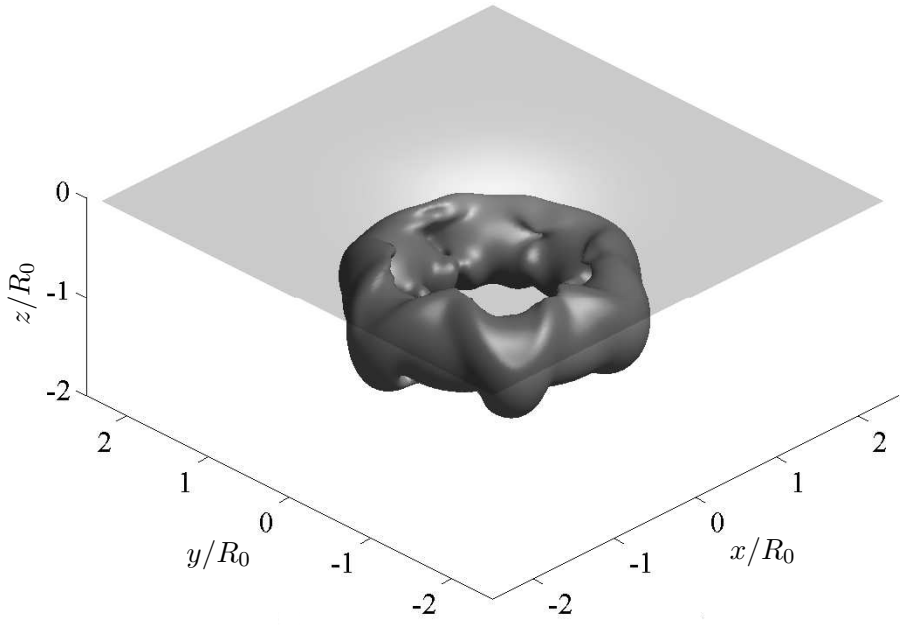

FIGURE 7.15: Development of the secondary structure for Case D3 on its approach to surface at time $(t - t_e)\Gamma_0/R_0^2 = 12.24$, visualised by an isosurface of $\mathrm{II}R_0^4/\Gamma_0^2 = -0.05$.

instability (see figure 7.15). The ascent of Case D3 induces a surface bulge, which is smaller in height compared to the laminar Case D1, due to the lower ring circulation and more diffuse core. However, for Case D3 the bulge is not circular but has a modulated wavy pattern as shown in figure 7.16(a). Comparing the surface bulge to the ring structure below, the surface modulation is in phase with the wavy inner core below. As the ring moves closer than approximately one radius of the surface it expands radially, forming a surface depression which is also modulated by the wavy inner core, as shown in figure 7.16(b).

The secondary structure is located in the ring periphery, consequentially, as the depth of the ring decreases it becomes in close contact with the surface. As in the unbounded domain neighbouring loops form next to one another in pairs but at the surface the loops move apart in the interior of the ring (indicated with arrows in figure 7.17(a)) and reconnect with the surface at their outer periphery (labeled by solid circles in figure 7.17(a)). The surface-normal vorticity ω_z field is shown in figure 7.17(b) in which the corresponding reconnection sites are also highlighted with solid circles. The neighbouring sites are of opposite sign, consistent with the counter rotating secondary loops. Also shown in figure 7.17(b) are regions of ω_z that lie between neighbouring loops of the secondary structure, highlighted by

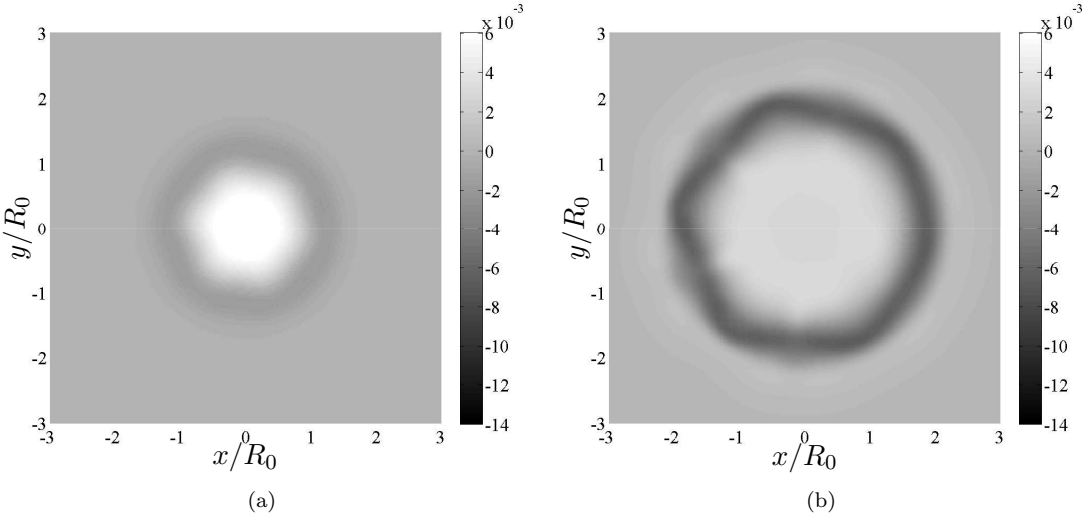

FIGURE 7.16: Free surface response to a transitional vortex ring (Case D3), light regions correspond to elevation, dark regions to depression: (a) $(t-t_e)\Gamma_0/R_0^2 = 15.21$; (b) $(t-t_e)\Gamma_0/R_0^2 = 19.93$.

dashed circles. They are also arranged in counter rotating pairs and correspond to the outer periphery of the inner core. Although the Fr is low, the small surface displacement does produce a small amount of opposite-signed vorticity ($\approx 0.5\%$ of the primary ring circulation) due to the curvature of the surface, which forms a secondary ring as in the laminar case. It is possible that the secondary ring stretches the outer periphery of the inner core to form the reconnection sites, consistent with the observations of Zhang *et al.* (1999) who simulated rings propagating at angles toward the surface. The surface displacement corresponding to the reconnecting ring is shown in figure 7.17(c). Notably there are no small surface indentations corresponding to the reconnecting filaments as seen in the experiments of Song *et al.* (1992). This is probably because the filaments are not yet fully connected to the surface, as ω_z at the surface is small. Further interpolation and simulation would presumably lead to the intensification of ω_z as both the secondary structure and the ring reconnect fully with the surface. Also evident either side of the depression, but more so on the interior, are local surface elevations which, like the depression, are also likely to be a result of the wavy inner core below.

The results of the transitional ring investigation have implications for the interpretation of the results of Song *et al.* (1992). The reconnection of Case D3 differs from the laminar instability and interaction, demonstrated by Case F2, due to the presence of the secondary structure. Its behaviour does, however, bear some resemblance to the high Re and Fr case of Song *et al.* (1992). Unlike their lower Re

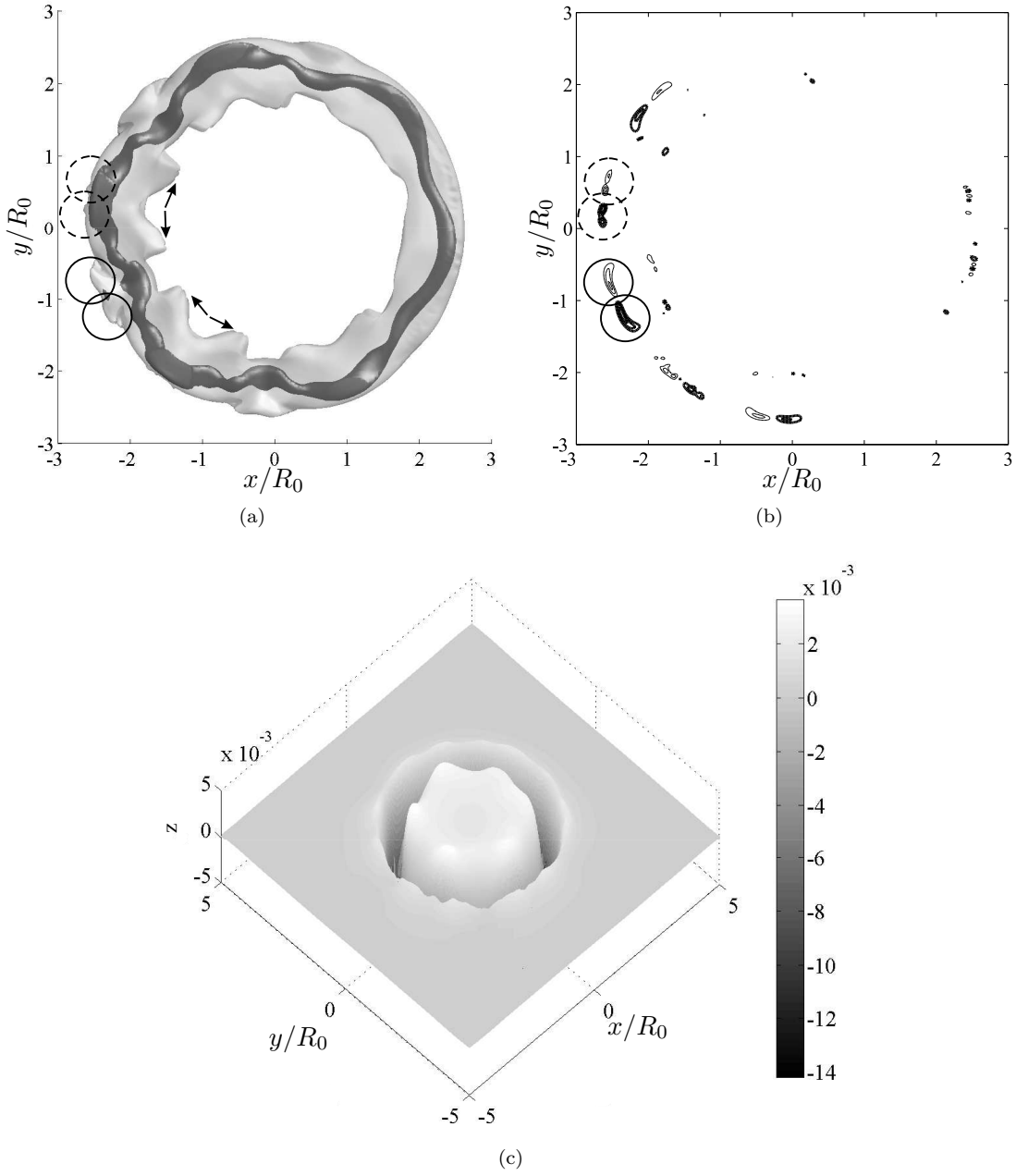

FIGURE 7.17: Surface reconnection of the secondary structure for Case D3 at time $(t-t_e)\Gamma_0/R_0^2 = 21.85$: (a) Double isosurface of $|\omega|$ at levels; $|\omega|\, R_0^2/\Gamma_0 = 4$ (dark) $|\omega|\, R_0^2/\Gamma_0 = 1.5$(light). Arrows denote splitting apart of neighbouring secondary structure in the ring interior, circles denote reconnection sites; (b) Corresponding ω_z on the surface at contour increments $\omega_z^{max}/5$, thicklines denote negative vorticity; (c) Surface elevations.

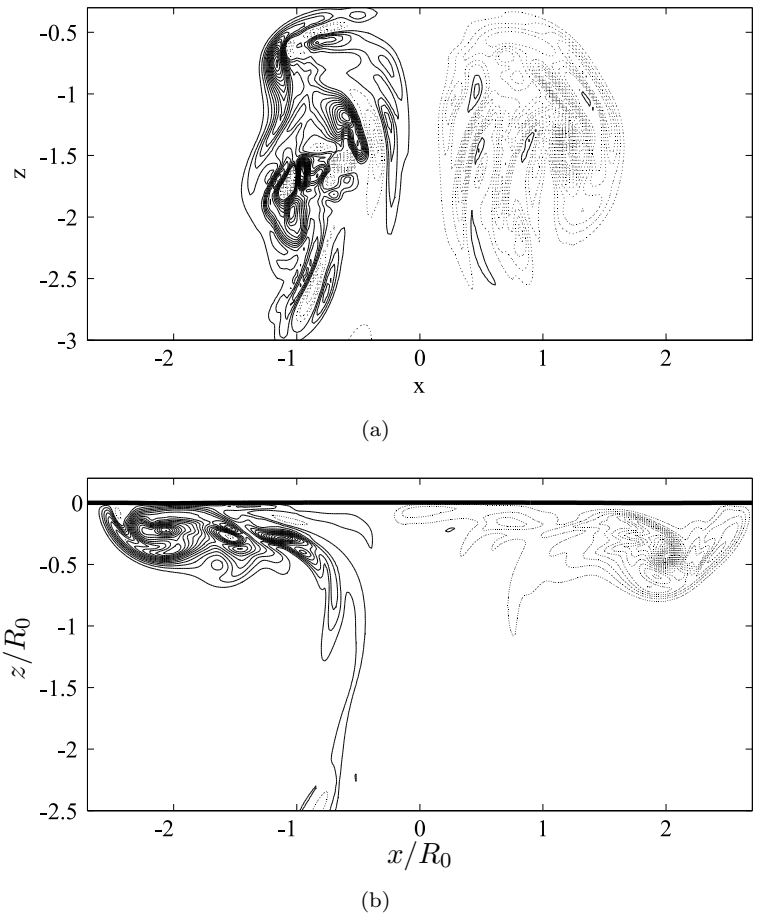

FIGURE 7.18: Contours of ω_θ on the $y = 0$ plane for turbulent Case D4 at (a) $(t - t_e)\Gamma_0/R_0^2 = 12.75$ and (b) $(t - t_e)\Gamma_0/R_0^2 = 25.4$. — increments of $\omega_y^{max}/20$, $\cdots$ increments of $\omega_y^{min}/20$ (negative). Thick solid line denotes surface location.

and Fr case, small surface indentations were seen outboard of the depression. Our results suggest that the indentations are due to the reconnection of the secondary structure. We speculate that the high Re leads to an aggressive amplification of the Widnall instability causing a transitional state to be reached as the ring impacts on the surface. This speculation is prompted by their early observation of three dimensional structure as the ring moved close to the surface. The surface striations seen across the depression could also be due to the wavy core structure below, as revealed by the localised elevations in figure 7.17(c).

7.5 The interaction of turbulent rings

As recorded in § 6.5.3, the onset of turbulence is marked by the shedding of secondary structure as a series of hairpin vortices. The process of instability growth

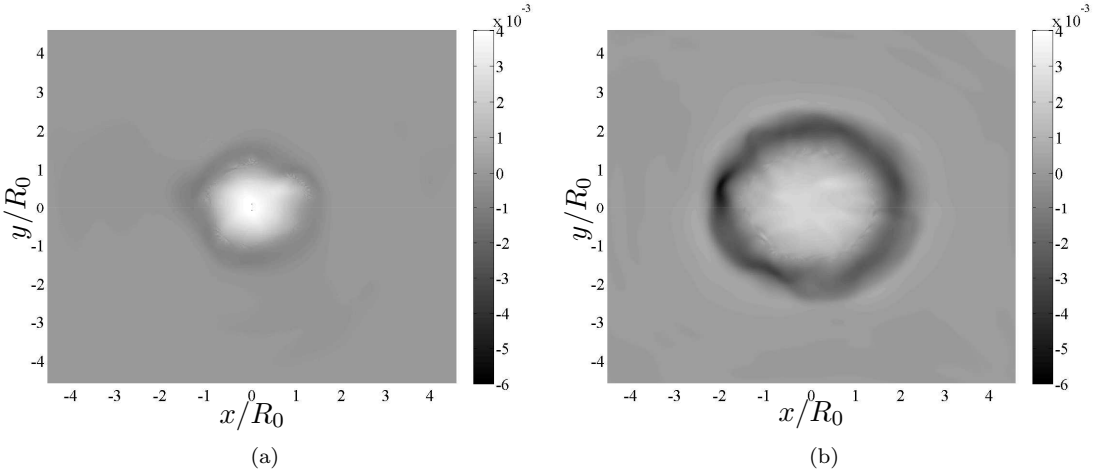

FIGURE 7.19: Surface elevations for turbulent Case D4 at times: (a) $(t - t_e)\Gamma_0/R_0^2 = 18.21$; (b) $(t - t_e)\Gamma_0/R_0^2 = 25.4$.

and the resulting onset of turbulence is not equal around the azimuth of the ring (see 6.5.3). For example, the turbulent core is more developed on the left-hand-side of figure 7.18(a) as the ring propagates toward the surface. The core develops as if unbounded until it reaches a depth of approximately one radius, where its dynamics are modified by its image above the surface. Its ascent induces a surface bulge, of smaller height than the laminar and transitional cases, as shown in figure 7.19. The bulge has no clear pattern reflecting the arrangement of the disorganised vorticity filaments below the surface.

The subsequent radial expansion below the surface has a profound effect on the structure of the turbulent core. As the core expands the swirling vorticity filaments that comprise the core region stretch and tilt into the radial plane. Figure 7.18(b) shows that the cores begin to find a greater degree of organisation or coherency. The swirling filaments then merge together to form a more defined core region and the opposite-signed vorticity, present on either side of the ring in figure 7.18(a), is either shed into the wake or canceled. The structure of the expanding ring resembles a turbulent thin-core ring (see figure 6.19(b) § 6.5.3) although with greater coherency in the core region. A similar phenomena was also seen in the numerical study of Teixeira & Belcher (2002) for a fully turbulent flow under a planar propagating wave field. The Stokes drift of particles below the waves tilted and stretched normal vorticity into the horizontal plane forming elongated streamwise vortices. We expect that future simulations of the ring to longer times than considered here could increase the core's coherency, such that it may become susceptible to the Crow instability, leading to reconnection to the surface in a series of

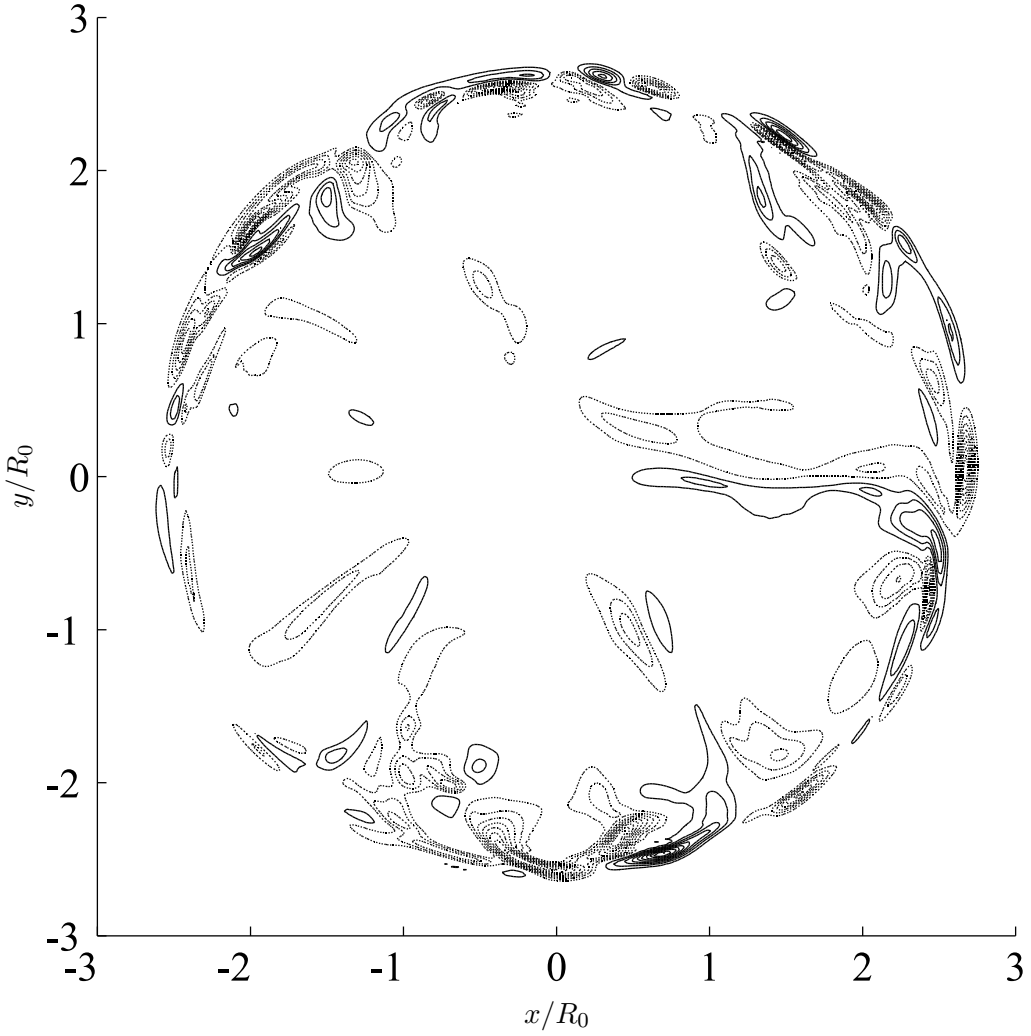

FIGURE 7.20: Contours of ω_z showing reconnection of vorticity filaments at the surface for turbulent Case D4 at time $(t-t_e)\Gamma_0/R_0^2 = 25.4$. Contour increments are $\omega_z^{max}/10$. Solid and broken lines represent positive and negative vorticity respectively.

turbulent U-shaped vorticity filaments. This requires further interpolation of the flow and must be left for future studies after the free-surface code is parallelised.

The turbulent core does not expand at a constant depth around the azimuth of the ring (see figure 7.18(b)). Consequentially the depth of the surface depression is not constant but deeper near regions of the ring where the core is closer to the surface, as shown in figure 7.19(b). The turbulent nature of the core means that its depth around the azimuth changes continually and the surface elevations change accordingly. Reconnection also occurs as the swirling core filaments come in close contact with the surface, as shown in figure 7.20. The pattern of the reconnection sites reflects the random nature of the core below and it is noted

that once reconnected with the surface, the filaments do not appear to detach during the simulation.

Chapter 8

Interaction of a laminar vortex ring with a surface wave field

In this chapter we document some aspects of the vortex ring interaction with a free surface that features a small amplitude gravity wave field. We start by formulating the mathematical description of the problem in § 8.1, followed by the numerical approach employed in § 8.2. In § 8.3 we describe the particular cases studied and their parameters. The results are given in § 8.4 along with a discussion of how the vortex modifies the waves (§ 8.4.1) and how the waves influence the evolution of the vortex (§ 8.4.2).

8.1 Mathematical background

We consider a single vortex ring of radius R and core radius δ, with circulation Γ and Reynolds number $\mathrm{Re} \equiv \Gamma/\nu$, with impulse $\mathbf{P}$ (defined in § 6.1). The ring propagates in the z-direction, with respect to Cartesian coordinates $\mathbf{x} = (x, y, z)$, toward a free surface, of Froude number $\mathrm{Fr} = \Gamma/\sqrt{gR^3}$, with corresponding velocity components $\mathbf{u} = (u, v, w)$; see figure 8.1. The vortex is embedded at depth d_0 such that it is centred about $\mathbf{x} = (0, 0, d_0)$ at time $t = 0$. The surface has a planar gravity wave field of amplitude a, wavelength λ, and celerity c, which propagates in the x-direction. In discussing the surface waves, we refer to waves that are yet to pass over the ring as being 'upstream' and waves that have passed over the ring as being 'downstream' (figure 8.1). We ignore the effects of surface tension and surfactants in our formulation, as we are principly interested in the interaction

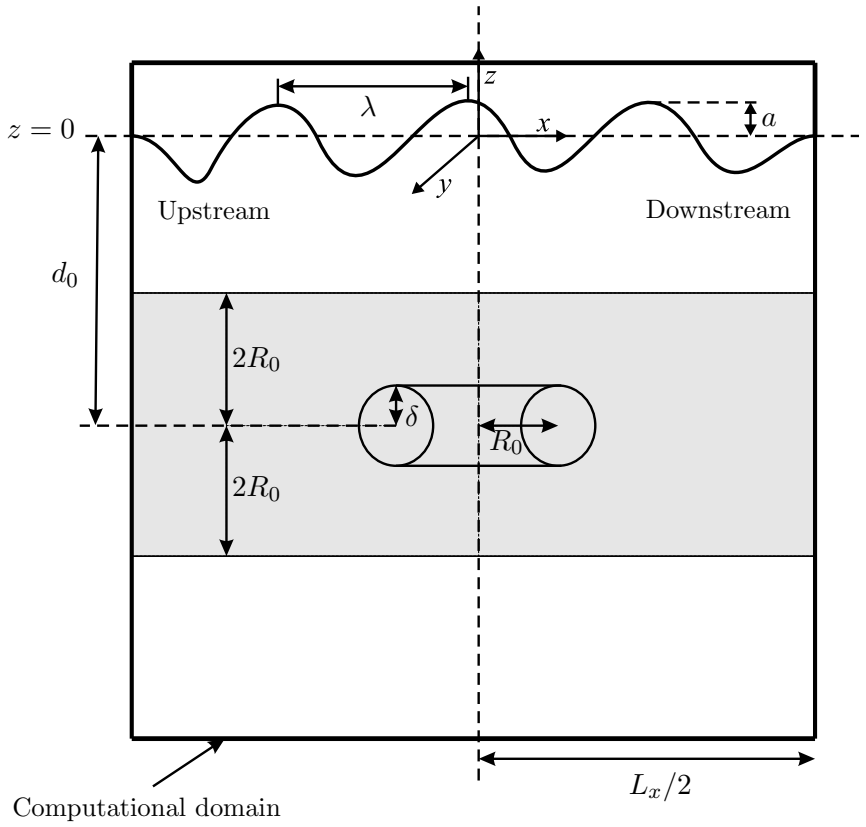

FIGURE 8.1: Schematic diagram of the vortex ring interaction with a surface wave field. The shaded region denotes the co-moving logging domain. Computational domain includes $0.22R_0$ of cells above the average surface position to capture surface movement.

of large vortex rings ($R \approx 10$m) produced by submersible vehicles. Therefore we exclude surface ripples and focus on the gravity waves.

8.2 Numerical Approach

The Cartesian computational domain assumes periodic boundary conditions in both the x and y-directions, so that we are, in effect, simulating an infinite array of rings. The presence of the gravity wave field requires that free-surface boundary conditions (see § 4.3.1) are imposed on the upper ($z = 0$) boundary. We therefore simulate the interaction using the free-surface code outlined in § 4.3. Impermeable free-slip boundary conditions are imposed in the horizontal plane at the lower extent of the z-axis. The initial ring velocity field was prescribed by embedding a vortex ring which has previously been evolved within the unbounded domain, following the method described in § 5.2.1. The initial field was completed by

Case	Fr	k/L_x	a/R_0	cR_0/Γ_0	$\Delta t\Gamma_0/R_0^2$
W1	0.3	2	0.04	1.9616	0.004779
W2	0.3	4	0.04	1.3871	0.006759
W3	0.3	8	0.04	0.9808	0.009558
W4	0.3	4	0.02	1.3871	0.006759
W5	0.3	4	0.08	1.3871	0.006759
W6	0.3	2	0.08	1.9616	0.004779
W7	0.6	2	0.04	0.9808	0.009558

TABLE 8.1: Table to show wave parameters: wavenumber k; amplitude a; celerity c. Also shown is the simulation time step Δt. All parameters nondimsionalised by ring lengths.

linearly superimposing the surface wave train and its associated velocity field (see § 5.2.2).

The ring circulation, impulse and radial measures (defined in § 6.1) are calculated in a co-moving cubic logging domain (see shaded region of figure 8.1) whose top and bottom is $2R_0$ from the ring centre. By employing a co-moving logging domain the ring wake trails behind and does not distort the integral ring measures. When the ring moves near to the surface, only the contribution of active cells (under the surface) with $\omega_\theta \geq 0.0$ enter the ring integrals, to avoid the contribution of vorticity generated due to surface curvature.

8.3 Simulation Parameters

We investigate the problem by examining the cases in table 8.1, which allow us to consider the effects of Froude number, wavenumber and wave amplitude on the ring interaction with a surface wave field. For all cases an identical thick-core laminar ring was embedded within the computational domain at an initial depth $d_0 = 3.49R_0$, where the zero subscript corresponds to an initial parameter at the time of embedding. The ring has been evolved for 40 non dimensional time units within the unbounded domain and has initial parameters: $R_0 = 1.147$; $\epsilon_0 = \delta_\theta/R_0 = 0.333$; and $\Gamma_0 = 0.907$. The computational domain had dimensions $L_x = L_y = 6.98R_0$ and $L_z = 7.2R_0$, with $N_x = N_y = 128$ and $N_z = 132$ grid cells respectively. Four grid cells are included above the average surface location to capture surface movement. Cases W1-3 feature a surface wave field with identical amplitude and

Froude number but varying wavenumber. The effect of wave amplitude can be assessed through comparison of Cases W2,W4 and W5 which feature the same wavenumber and Froude number. Case W6, with its large amplitude and low wavenumber, possesses the most energetic wavefield. Finally, Case W7 allows us to investigate the effect of Froude number through comparison with Case W1.

In presenting the results we nondimensionalise flow quantities by R_0 and Γ_0, given above. Since the aim of these simulations is an exploratory study, we have reduced the grid resolution and hence duration of the simulations, to allow us to make best use of available computational resources.

8.4 Results

8.4.1 Surface wave deformation

The degree to which the vortex ring distorts the surface wave train is dependent on the Froude number, wave amplitude and wavenumber. Let us consider the surface response from the view point of a wave approaching the vortex ring. As the wave nears the ring, the surface velocity field induced by the ring (figure 8.2(a)) opposes its motion. Consequentially the ring 'diffracts'[1] the waves, with the central region lagging behind the rest of the wave (figure 8.2(b)). As the wave passes over the ring centreline ($x = 0$) the ring velocity field changes direction and accelerates the centre of the wave. Gradually the wave moves back in phase with itself downstream of the ring. A similar type of wave diffraction was observed in the experiments of Vivanco & Melo (2004), which featured a vortex dipole aligned perpendicularly to a planar wave train. The degree to which the wave diffracts is dependent on the wavelength and amplitude of the wave. Short wavelength, small amplitude waves are distorted to the greatest degree by the vortex, whereas the larger amplitude cases are only diffracted by a small amount (compare figures 8.2(b) and 8.2(c)). The wave diffraction intensifies as the ring moves closer to the surface and expands parallel to it.

The investigation of a laminar vortex ring with an initially undisturbed free surface (§ 7.3.1) has shown that the radial expansion of the ring forms a surface depression (see figure 7.9). As the ring expands in the presence of a surface wave field, short wavelength waves radiate across the surface. The secondary waves are of small

[1] We use the term 'diffraction' to refer to the bending of the surface waves.

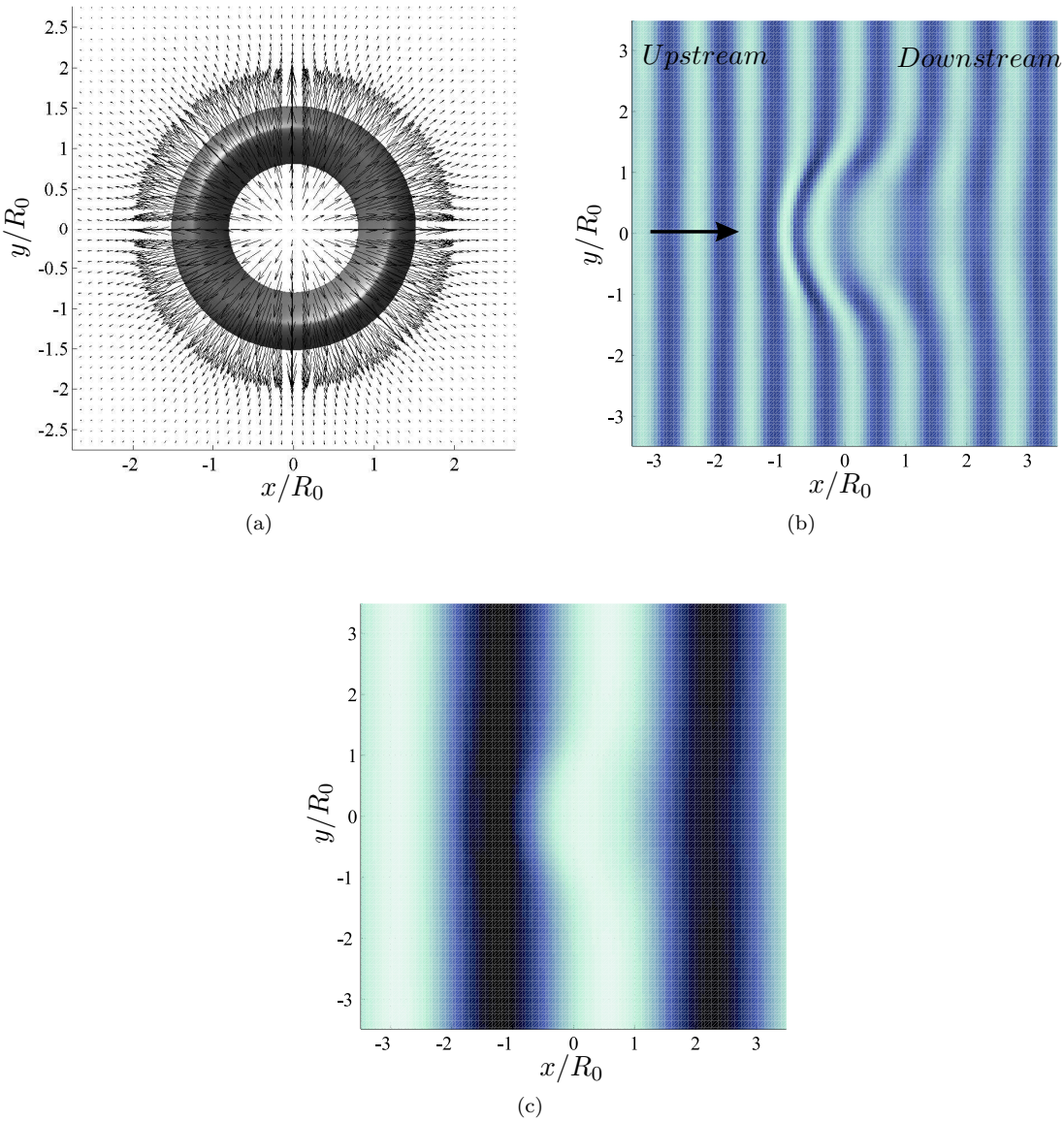

FIGURE 8.2: Wave diffraction. (a) A typical surface velocity vector field induced by a vortex ring on a surface without waves, Case S1, core region marked with isosurface of II, at $(t - t_e)\Gamma_0/R_0^2 = 15.15$. (b) Surface field for Case W3 at $(t - t_e)\Gamma_0/R_0^2 = 15.15$ showing large-scale wave diffraction. (c) Surface field for Case W6 at $(t - t_e)\Gamma_0/R_0^2 = 15.15$ showing small-scale wave diffraction. Direction of wave motion indicated by arrow, crests lightly shaded, troughs darkly shaded.

amplitude compared to the wave train and appear to originate from the surface depression. Initially the secondary waves radiate in the positive and negative x-directions (figure 8.3(a)), but as the ring expands further, the waves radiate from around the entire circumference of the ring 8.3(b). The secondary wave field is analogous to that caused by a droplet falling on an initially flat pool of fluid. In

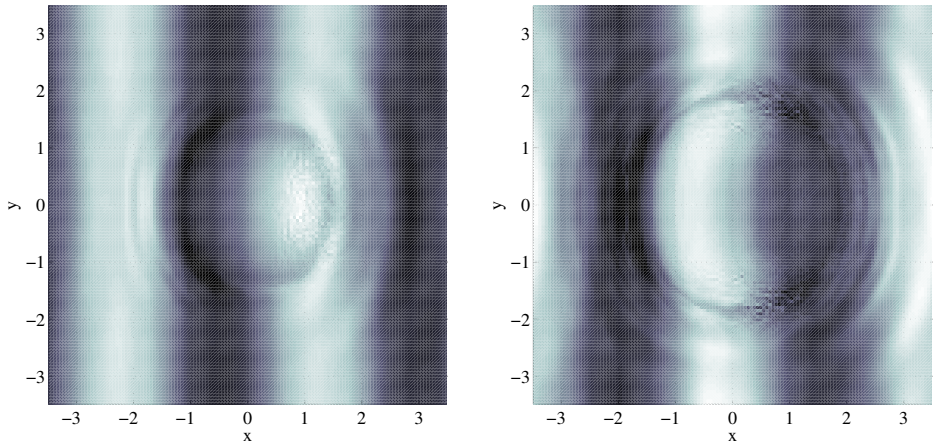

FIGURE 8.3: The generation of secondary waves for Case W1, the wave train propagates from left to right with crests lightly shaded and troughs darkly: (a) $(t - t_e)\Gamma_0/R_0^2 = 18.04$ (b) $(t - t_e)\Gamma_0/R_0^2 = 20.25$

the case of the droplet, the waves are radiated due to rapid surface oscillation caused by the collision. In this case the stimulus appears to be the interaction of the surface wave train with the surface depression induced by the ring.

It is noted that the secondary wave generation is more pronounced for cases with large wavelength and small amplitude, greatest for Case W1. Case W4, which features medium wavelength, small amplitude waves also radiates prominent secondary waves but with wavelength noticeably smaller than for Case W1. Measuring the distance between successive wave crests shows that the wavelength of the secondary waves is approximately one quarter of that of the wave train. Cases W3 and W5 show only small signs of secondary wave generation. Case W3 was terminated before the other cases due to violation of the surface maximum slope condition (4.8). However, at the time of termination it showed far less secondary wave generation than all of the other cases except Case W5.

The elevation history of two points located on the surface at the centre, $\mathbf{x} = (0, 0, h)$ and downstream of the ring at $(2.15R_0, 0, h)$ are shown in figure 8.4. Figures 8.4(a) and 8.4(c) show the entire history, while figures 8.4(b) and 8.4(d) focus on the elevation history after the secondary waves have been generated. Considering first the elevation at the centre of the domain, figure 8.4(a), a noticeable peak occurs at $14 \leq t\Gamma_0/R_0^2 \leq 19$ which corresponds to the ring inducing a surface bulge. The surface elevation at $\mathbf{x} = (2.15R_0, 0, h)$ follows an approximately constant sinusoidal motion until time $(t-t_e)\Gamma_0/R_0^2 = 16$, at which point the secondary

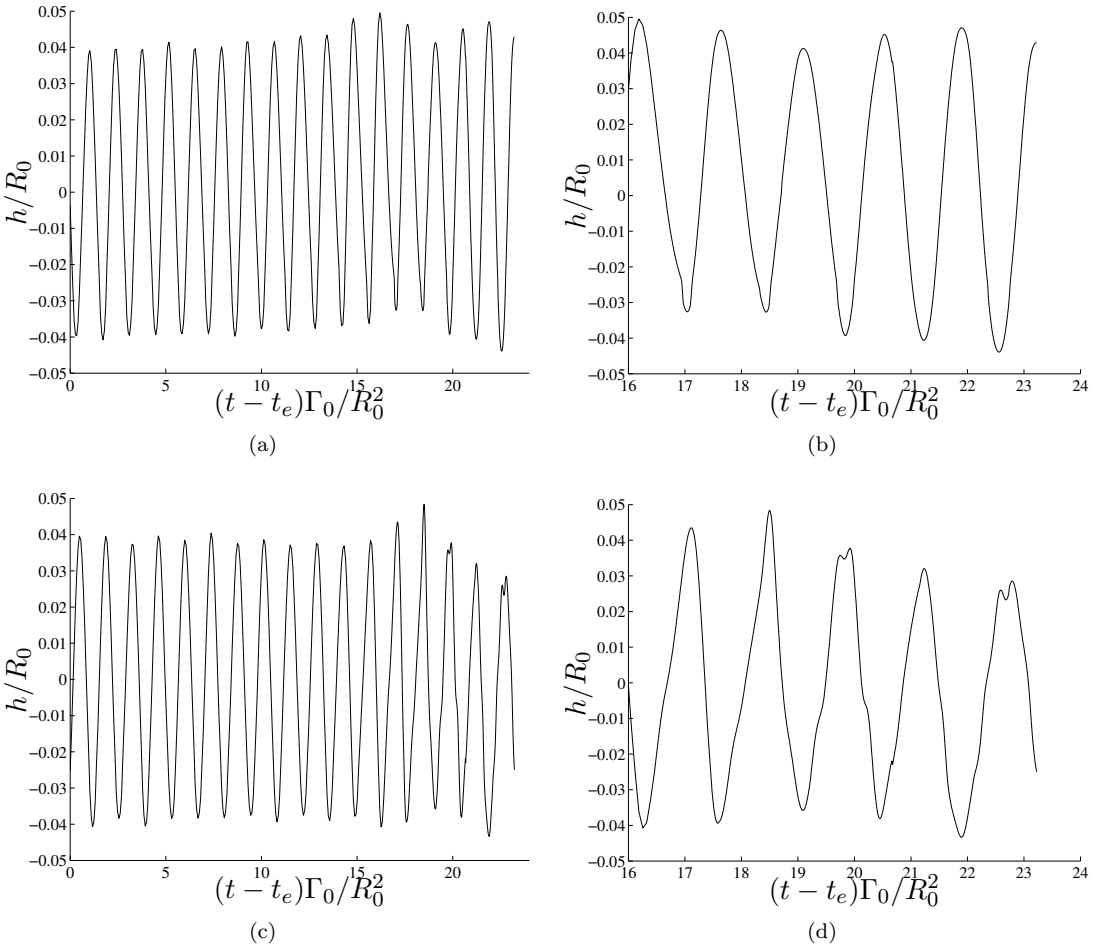

FIGURE 8.4: Plots of surface elevation for Case W1 at two points located at: (a)&(b) $\mathbf{x} = (0, 0, h)$; (c)&(d) $\mathbf{x} = (2.15R_0, 0, h)$.

waves are evident, superimposed on top of the planar wave train. The secondary waves radiate toward the domain boundaries and not toward the ring centreline as the elevation history in figure 8.4(b) continues to follow a sinusoidal path. The crests of the planar wave train at $(t - t_e)\Gamma_0/R_0^2 = 19.7$ and $(t - t_e)\Gamma_0/R_0^2 = 22.7$ in figure 8.4(d) correspond to depressions of the secondary wave field. The figure shows that the amplitude of the secondary waves increase slightly with time. It is likely that this occurs due to the stretching of the ring below the surface, which intensifies the local vorticity and associated velocity field, increasing the size of the surface depression with time. The amplitude of the secondary waves at $(t - t_e)\Gamma_0/R_0^2 = 19.7$ and $(t - t_e)\Gamma_0/R_0^2 = 22.7$ is approximately 5–10% of that of the wave train.

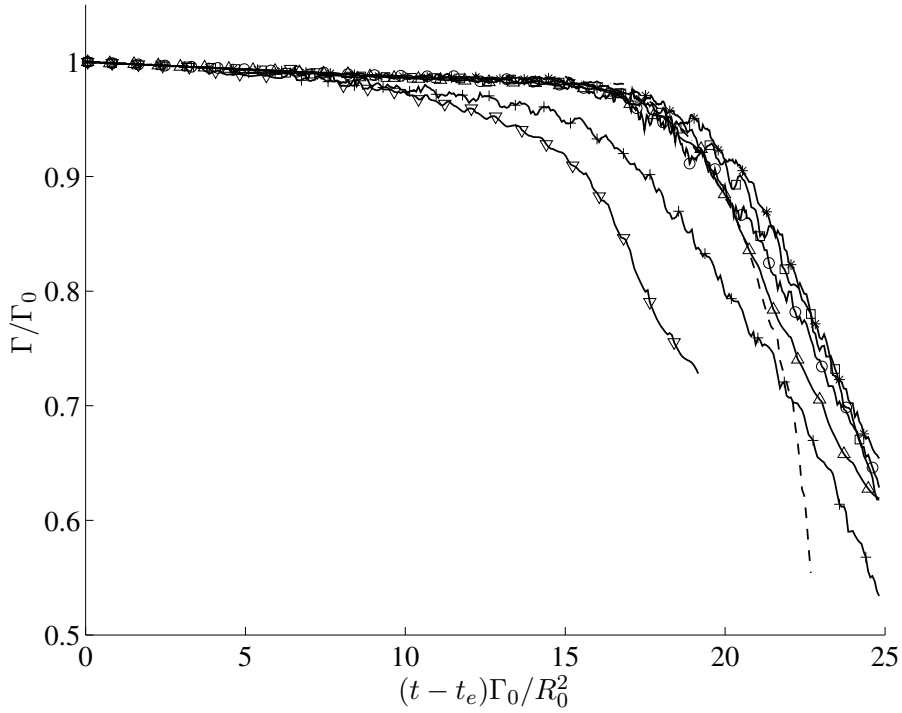

FIGURE 8.5: Evolution of total circulation for surface wave cases (solid lines highlighted with symbols): $*$, Case W1; $\square$, Case W2; ∇, Case W3; Δ, Case W4; $+$, Case W5; $\circ$, Case W6; $- - -$, Case W7.

8.4.2 Vortex dynamics

We now consider the effect of the wave train on the vortex ring. As the ring moves close to the surface the combination of the curvature of the surface wave field and the ring's velocity field creates opposite-signed vorticity, which reduces the total circulation (see figure 8.5). The magnitude of the surface vorticity depends on both the local surface curvature and the tangential flow velocity below (Longuet-Higgins, 1998). Cases with shorter wavelength and larger amplitude waves therefore generate the greater amount of surface vorticity by virtue of having higher surface curvature. For this reason the total circulation, which is the sum of the positive ring circulation and negative surface-curvature-induced circulation, decays fastest for cases W3 and W5 by virtue of their higher wave curvature. The higher Froude number Case W7 also features a sharp fall in circulation and will be addressed below.

We first consider the low Froude number cases. The magnitude of the opposite-signed vorticity varies from case to case dependent on the degree of curvature of the waves. For cases with high wave curvature, such as W2, W3, W4 and W5, the opposite-signed vorticity is strong enough to make the ring expand asymmetri-

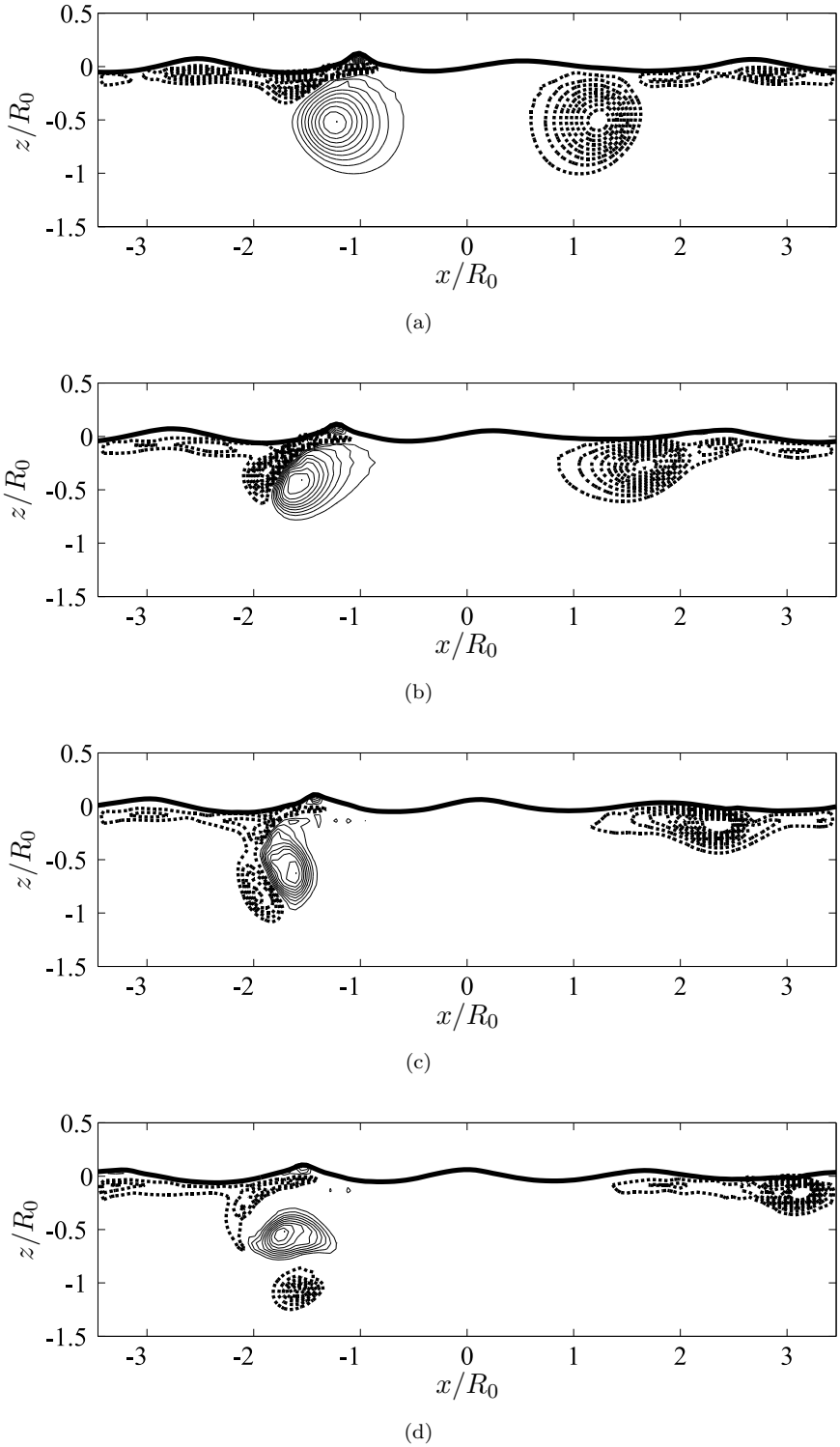

FIGURE 8.6: Vortex rebound for Case W5. ω_y contours plotted at increments of $\omega_y^{max}/10$ with solid and broken lines corresponding to positive and negative contours respectively. Surface elevation shown by thick solid line. Subplots at times: (a) $(t-t_e)\Gamma_0/R_0^2 = 16.53$; (b) $(t-t_e)\Gamma_0/R_0^2 = 19.28$; (c) $(t-t_e)\Gamma_0/R_0^2 = 22.04$; and (d) $(t-t_e)\Gamma_0/R_0^2 = 24.79$. Waves propagate from left to right.

cally. Figure 8.6 demonstrates a typical vortex ring interaction with high curvature surface waves. To help describe the interaction we label the left-side core as the 'upstream core' and the right-side core as the 'downstream core'. Initially the ring expands symmetrically in the radial direction. However as the ring moves close to the surface waves it begins to induce surface vorticity (figure 8.6(a)). Near the upstream core the surface vorticity is of opposite sign but near to the downstream core the surface vorticity is of the same sign as the ring (figure 8.6(b)). Consequentially, as the downstream core expands radially it merges with the surface vorticity, increasing the ring circulation locally. Since the surface curvature is far greater at the upstream core, the opposite-signed vorticity quickly becomes of comparable strength to the ring, and prevents it from expanding further in the upstream direction (figure 8.6(c)). Indeed, the opposite-signed vorticity becomes so strong that it wraps around the upstream core and locally the ring and surface vorticity begin to rebound from the surface under their induced motion (figure 8.6(d)). At the upstream extent, the ring behaviour is reminiscent of a ring rebounding during the interaction of a vortex ring with an initially flat free surface featuring surfactants (Chu *et al.*, 1993). The downstream section continues to expand radially, resulting in a distorted asymmetric ring that is bent away from the surface at the upstream section. Due to their higher wave curvature, Cases W3 and W5 feature significantly deeper rebounds than the rest of the cases.

The lower wavenumber cases, W1 and W6 show a different ring behaviour at the

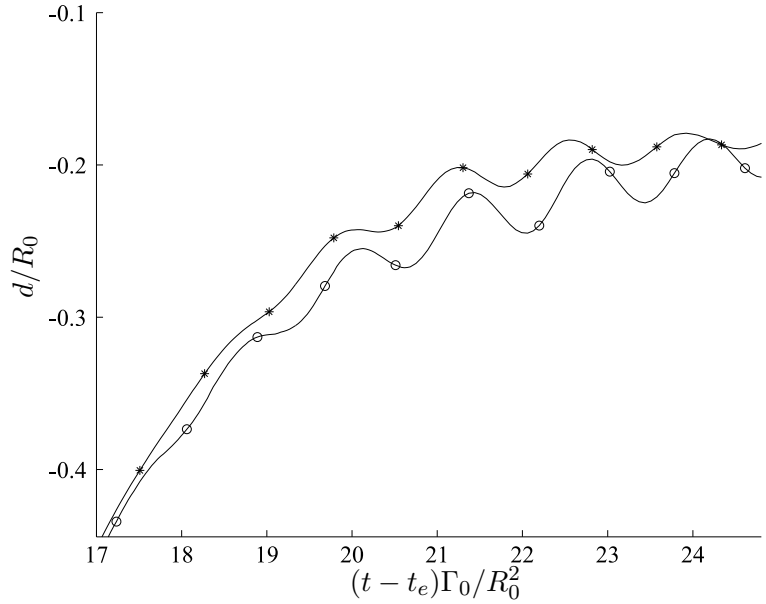

FIGURE 8.7: Sinusoidal variation in ring depth: $*$, Case W1; $\circ$, Case W6.

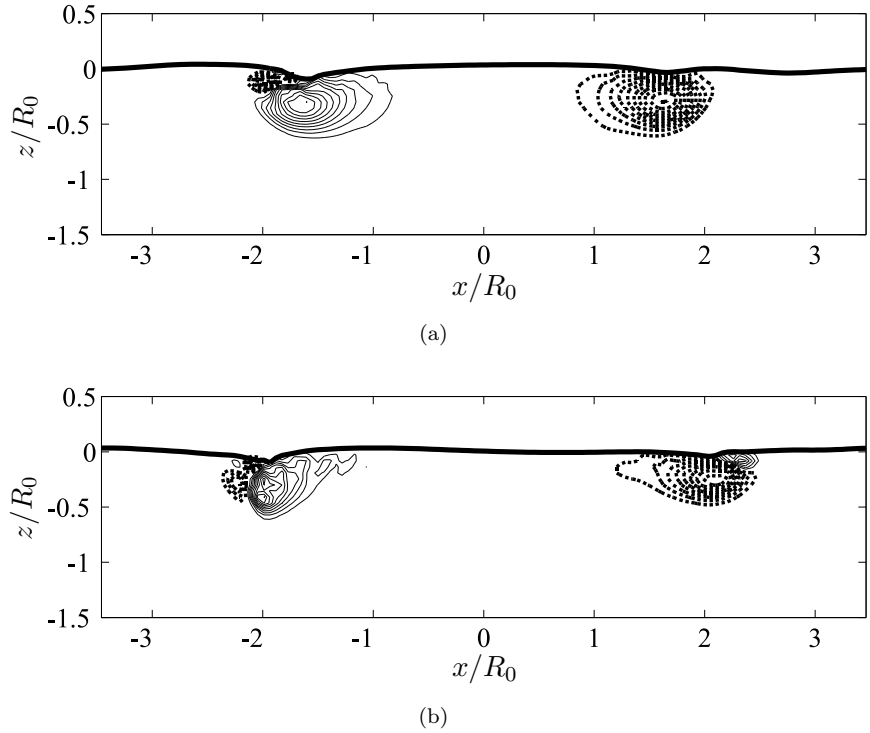

FIGURE 8.8: Evolution of surface vorticity for Case W7. ω_y contours plotted at increments of $\omega_y^{max}/10$ with solid and broken lines corresponding to positive and negative contours respectively. Surface elevation shown by thick solid line. Subplots at times: (a) $(t - t_e)\Gamma_0/R_0^2 = 16.53$; and (b) $(t - t_e)\Gamma_0/R_0^2 = 19.28$. Waves propagate from left to right.

surface. As the rings move closer to the surface their depth varies sinusoidally, with a period which matches that of the surface waves (see figure 8.7). For these cases the wavelength of the surface waves are larger than the ring diameter. As the surface waves pass over the expanding rings the wave crests induce an upwards motion and the wave troughs induce a downwards motion, keeping the distance to the surface approximately constant.

The total circulation decays fastest for the high Froude number case (W7) (figure 8.5). The ring behaves in a different way than the lower Froude number cases. Due to the higher Froude number, the surface is more 'malleable' to the ring. Thus the ring forms a larger surface depression as it expands under the surface. The surface curvature is higher near the upstream core, thus the ring initially generates opposite-signed vorticity at this location (figure 8.8(a)). This contrasts greatly with the free-surface interaction in the absence of waves, where the surface displacement and corresponding surface vorticity is constant around the circumference of the ring, resulting in a symmetric ring expansion. As the ring expands below the surface, the core vorticity intensifies through stretching, and the tangen-

tial velocity below the surface increases. This leads to opposite-signed vorticity developing outside the downstream core, but of lower circulation than the corresponding upstream vorticity (figure 8.8(b)). The generation of opposite-signed vorticity around the entire circumference of the ring leads to a higher decay rate of the total circulation than the lower Froude number cases. This is because the lower Froude number cases only produce opposite-signed vorticity upstream of the ring and instead produce co-rotating vorticity downstream of the ring.

Chapter 9

Summary

9.1 Investigation of vortex ring evolution from a laminar to a turbulent state

Our investigation of the evolution of a vortex ring from a laminar to a turbulent state has uncovered many previously unreported and interesting physics. One important finding is the difference in evolution of thin- and thick-core vortex rings. Analysis of integral measures of vortex ring geometry has shown that the slenderness ratio ($\epsilon = \delta/R$) has a strong influence on the evolution of the ring geometry and dynamics. The diffusion of thin-core rings is well described by Saffman's equation (2.3) (Saffman, 1970). However the core diffusion of thick-core rings ($\epsilon > 0.36$) is limited by the ring centreline and the presence of the entrainment bubble surface, which clips the outer edge of the vorticity distribution. It was found that as ϵ increases the vorticity distribution within the core becomes increasingly skewed with a steepening of the vorticity profile in the vicinity of the entrainment bubble surface and greater vorticity diffusion into a laminar wake. The skewing of the vorticity distribution also has a strong effect on the ring translational velocity, leading us to define an expression for the constant in the classical velocity equation as a series expansion of ϵ (6.9).

The simulations have shown that thick-core laminar rings produce a substantial wake, due to the initial adjustment to a non Gaussian vorticity distribution and as a result of vorticity detrainment. This has implications for periodic computational domains, used for example by Shariff *et al.* (1994) to establish a viscous correction to the inviscid growth rate of Widnall & Tsai (1977); we have shown

that the interaction between the ring and its recycled wake increases the growth rate of the linear Widnall instability. We have presented new revised growth rates from simulations using inflow and outflow boundary conditions in the axis of ring propagation. By modifying the viscous correction to use instantaneous values of the ring parameters we find close agreement for the growth rates of both thin- and thick-core rings.

Visualising the vortex ring transition to turbulence has highlighted the importance of secondary vortical structure, which develops when the inner core instability waves are of large enough amplitude. The secondary structure is formed through tilting and stretching of the outer or 'halo' core vorticity. It develops as counter-rotating neighbouring loops of vorticity that meet one another at saddle points to form an interwoven mesh around the inner core region. It was shown, by analysing Lagrangian pathlines of fluid particles entrained into the vortex ring bubble, that the secondary structure initiates localised detrainment zones prior to the onset of turbulence. The latter stages of transition are marked by the protrusion of the secondary structure outside the entrainment bubble, causing it to trail behind into the wake. The loops detach and reattach with their neighbour to form hairpin vortices that are deposited into the wake. The local equilibrium between the inner core and the halo vorticity is broken and the ring becomes locally turbulent where the hairpin vortices were ejected. Lagrangian particle analysis of the core region during the transitional phase has shown the generation of an inner region of axial flow which moves along the vortex core centreline toward the region of greatest core stretching. The outer region moves in the opposing direction consistent with the experimental observations of Naitoh *et al.* (2002) for naturally evolved rings. The dominance of the $n = 1$ mode during transition was found to influence the magnitude of the axial flow. The structure of the resultant turbulent ring was found to depend on ϵ, with thin-core rings maintaining a core region of organised vorticity. During the turbulent phase discrete vortical structure is shed from the ring in the form of hairpin vortices.

9.2 Interaction of a vortex ring with an undisturbed free surface

The orthogonal interaction of a vortex ring with an undisturbed free surface was found to differ dependent upon the condition of the ring: whether laminar; transitional; or turbulent. During the ascent of laminar rings the Widnall instability

develops until the ring approaches a depth of approximately one radius, giving the ring an azimuthal structure. The degree to which the structure and corresponding azimuthal modes are amplified depends on the duration of the ring approach to the surface, the Reynolds number and the ring slenderness ratio. The ring approach induces a circular surface bulge, but as the ring moves closer than one radius its dynamics begin to be strongly influenced by its virtual image above the surface and the bulge drops. The Widnall instability is suppressed as the ring expands and a depression forms on the surface above and outboard of the ring. The azimuthal modes, which define the structure of the unstable ring, decay until the ring expands to approximately twice its initial radius. At this point the ring and its virtual image locally resemble two line vortices and the ring becomes unstable to the Crow instability. The instability amplifies a broadband spectrum of azimuthal modes at a higher growth rate than the Widnall instability. The growth rates of the modes compare well with the stability analysis of Crow (1970). As all of the modes are amplified at similar growth rates, the dominant mode is preselected by the development of the Widnall instability as the ring approaches the surface. The experiments of Song *et al.* (1992) and Lim & Nickels (1992) suggest that the instability eventually leads to reconnection of the wavy core region with the surface, however the ring was not expanded far enough here for this to occur, due to constraints on the resolution and domain size.

Surface displacement scales with the square of the Froude number. The curvature, associated with the displacement of the surface into a depression, produces opposite-signed vorticity, which roles up to form a secondary ring outboard of the expanding primary ring. This leads to a decay in the total circulation approximately equal to the circulation of the secondary ring, larger for the higher Froude number cases. Another mechanism for circulation decay at the surface is brought about by the tail of the ring's vorticity profile touching the surface. This cancels with its virtual image above the surface, reducing the ring circulation, and occurs with or without surface curvature present. The secondary ring affects the depth of the ring during its expansion below the surface. If the secondary ring is significantly strong it induces a downwards component on the primary ring, causing it to expand below the surface at a greater depth.

Analysis of a transitional ring has given some explanations for the experimental observations of Song *et al.* (1992). The reorganisation of the transitional ring to a wavy inner core encapsulated by a series of counter-rotating loops of weaker vorticity modifies the ring/surface interaction. At first the initial surface bulge is modulated into a wavy pattern which reflects the shape of the ring's inner core

region. The wavy pattern is also present in the subsequent surface depression, which forms as the ring expands. The impact of the peripheral looping structure on the surface results in the splitting of neighbouring loops, which reconnect with the surface in the outer ring periphery. This is the likely source of the surface indentations reported by Song *et al.* (1992). Reconnection of the inner core region was also found, commencing toward its outer extent.

As the turbulent ring expands below the surface, the filaments that comprise its core region are stretched in the radial direction. This gives the initially thick-core a degree of coherency as it becomes thinner, reminiscent of a thin-core turbulent ring. Surface reconnection occurs as the swirling core filaments impact on the surface. The reconnection sites and surface displacements follow no clear pattern, reflecting the turbulent nature of the core below.

9.3 Interaction of a laminar vortex ring with a surface wave field

This exploratory study has highlighted a number of physical features of the interaction of a vortex ring with a surface wave field, which can be grouped into wave effects and ring effects. The ring approach to the surface causes diffraction to the gravity wave field. The degree to which the ring diffracts the waves is found to be a function of the wave amplitude and wavelength. Wave diffraction is larger for gravity waves with small wavelength and amplitude. As the ring expands radially, its velocity field forms a depression on the surface, from which small-amplitude waves radiate. These secondary waves are more pronounced for large wavelength and small amplitude gravity wave trains. Surface curvature, associated with the waves and surface displacement induced by the ring, produces surface vorticity which reduces the total circulation. For the low Froude number cases the surface vorticity is of opposite sign to that in the core upstream of the ring and co-rotating downstream of the ring. Cases with high wave curvature produce large amounts of surface vorticity, which restricts the ring from expanding in the upstream direction and results in a highly asymmetric expansion. If the curvature is sufficiently high, the opposite-signed vorticity wraps around the upstream core and the ring rebounds locally from the surface. For cases with low curvature and large amplitude waves, the ring depth is modified by the wave field. The ring moves sinusoidally up and down following the wave crests and troughs, remaining an approximately constant distance from the surface. The high Froude number case produces a surface

depression, which is sufficiently deep to generate opposite-signed vorticity around the entire ring azimuth. This results in a faster decay of the total circulation than the lower Froude number cases. The high Froude number case also expands with a slight asymmetry as the higher wave curvature near the upstream extent of the ring produces greater opposite-signed vorticity than the downstream extent.

Chapter 10

Future work

10.1 Investigation of vortex ring evolution from a laminar to a turbulent state

The area of greatest potential for further work is the turbulent vortex ring which has only been touched upon by this project due to time constraints. A database of velocity fields has been generated for both the thick- and thin-core vortex rings (Cases A1 and B3) and awaits analysis. The subject of future work could be the structure of the turbulence in the core region. Turbulent statistics for the ring could be compared to those of other turbulent flows such as wakes and jets. This may help us to distinguish between different types of turbulent motions in the ocean and determine their sources. It would also be feasible to investigate the entrainment and detrainment characteristics of the turbulent ring using a Lagrangian particle approach as conducted here for laminar and transitional rings. This may go some way to justifying the inferences of Glezer & Coles (1990) that vortex tubes of alternating sign are wrapped around the turbulent core influencing entrainment and detrainment of fluid. It is also of interest to determine the end point of the turbulent ring. Will the rings relaminarise, as in the experiments of Wiegand & Gharib (1994), or will they become increasingly diffuse through the influence of viscosity?

10.2 Interaction of a vortex ring with an undisturbed free surface

The investigation into the orthogonal interaction of a vortex ring with a free surface has answered a number of questions brought up by previous experimental work. However, the distance through which the ring has been able to expand below the surface has been limited by the resolution and domain size. Parallelisation of the free-surface code would alleviate this problem allowing larger domain sizes and greater grid resolution. This would allow both the laminar and transitional rings to develop to the point of surface reconnection. In this way the influence of surface curvature on the development of the Crow instability could be investigated. Further expansion of the turbulent ring is also of interest as the ring appears to be relaminarising in the present simulations. The combined influences of the Widnall and Crow instabilities have been shown by simulating a single ring in the fixed-boundary code. Repetition of this simulation with rings of differing slenderness ratio and Reynolds number will allow us to explore the Crow instability further.

10.3 Interaction of a laminar vortex ring with a surface wave field

A number of previously undocumented phenomena have been uncovered by our exploratory investigation. The main task of future work is thus to improve the current simulations to give greater confidence in the results. Firstly the simulations have been conducted at a relatively low grid resolution, which although adequate to expose the main flow features, does not capture the ring instability or fine-scale surface vorticity well. Larger, more refined, simulations need to be carried out to assess the grid dependency of the results.

As the domain is periodic in the lateral directions the surface waves are recycled through the domain. Any distortion to the wave field thus interacts with the ring on subsequent passes. This produces a feedback mechanism which may influence the results. It is also noted that secondary waves radiate across the surface as the ring expands. They too have the potential to pass through the periodic boundaries and interact with the ring. Two methods present themselves to alleviate the periodic-boundary problem. One option is to greatly increase the lateral boundary lengths and by doing so prevent distorted waves from interacting with the ring.

The success of this option depends on parallelisation of the free-surface code and the time period through which the ring is to be simulated. An alternative method might utilise the flowfields from the ring interaction with an undisturbed free surface. A gravity wave field could be linearly superimposed onto the initially undisturbed surface. The simulation could then be performed until the wavefield passed over the ring for a second time. At which point the simulation could be ceased and a new simulation started by superimposing a wave train on a flow field (from the initially undisturbed ring/surface interaction) at a later time. By simulating each flowfield for a relatively short time period the wave physics and ring behaviour could be deduced without the contamination of wave reflections. A possible drawback of this method is that a sinusoidal wavefield, as employed to currently initialise the gravity waves, is not a good approximation of the wave field when the ring becomes close to the surface.

Chapter 11

Appendix A

Included below is an outline of the split merge technique employed by the free surface code to update the surface elevations. A full description can be found in Thomas *et al.* (1995).

11.1 Outline of the split-merge technique

The technique uses a simple surface locater which allows the surface height to be related to the volume of cells directly below it. Note, as the code uses a staggered grid only the pressure points are located at the continuity cell centres, whose fluid volume are Fc_{ijk}. The staggered u_{ijk}, v_{ijk}, w_{ijk} cells have volumes Fx_{ijk}, Fy_{ijk}, Fz_{ijk} respectively. The surface elevations h_{ij} are defined for both pressure cells (hc_{ij}), and staggered cells (hx_{ij} and hy_{ij}) as equal to the height of the column of fluid cells below,

$$hq_{ij} = \sum_k Fq_{ij}/(\Delta x \Delta y) \quad \text{for all } q \in c, x, y. \tag{11.1}$$

The centred and staggered forms of F and indeed h must be mutually consistent, this is achieved by enforcing

$$hx_{ij} = \frac{1}{2}(hc_{i,j} + hc_{i-1,j}), \tag{11.2}$$

$$hy_{ij} = \frac{1}{2}(hc_{i,j} + hc_{i,j-1}). \tag{11.3}$$

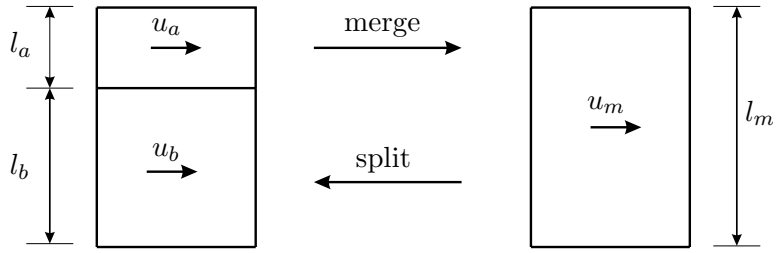

FIGURE 11.1: The splitting and merging of surface cells.

There is a possibility that the cells directly below the surface could possess a volume that approaches zero, forming a potential singularity in the Navier stokes equations. This problem is alleviated by allowing surface cells to grow, split or merge dependent upon the volume of fluid in the cell. If a surface cell becomes less than half empty it merges with the cell below forming one large surface cell, with the new velocity u_m and volume F_m updated to conserve momentum and mass:

$$l_m = l_a + l_b, \quad u_m = l_a u_a/(l_a + l_b)) + l_b u_b/(l_a + l_b). \tag{11.4}$$

If the height of a merged cell then becomes larger than $3/2\Delta z$ it will its split into two cells, a lower cell of dimensions $\Delta x \times \Delta y \times \Delta z$ and a partially filled surface cell, the process is shown in figure 11.1. Each surface cell has a complete base, a complete free surface and at least one neighbour in each horizontal direction, but not necessarily confined to the same vertical level. A complication arises when considering the surface level in relation to the centred (continuity) cells as shown in figure 11.2. If we consider cell A to be the surface cell, the surface can be present at any level between pressure points p_1 and p_2. However, dependent on the position of the surface, there may or may not be a w-cell between the pressure cell and the surface. For example, if the surface is above w_2 (e.g. h_2) the w-point w_2 will be present above the pressure surface cell, whereas if the surface is below w_2 (e.g. h_1) the surface w-cell will be w_1 and the pressure cell will not have a w-point between it and the surface. In the first case the pressure point is an internal cell and can be solved by the regular continuity equations, however if there is no w-cell between the surface and the uppermost pressure cell, such as for the second case, it is not possible to use the continuity equations and the pressure cell must be updated through interpolation of the surface boundary condition, see below.

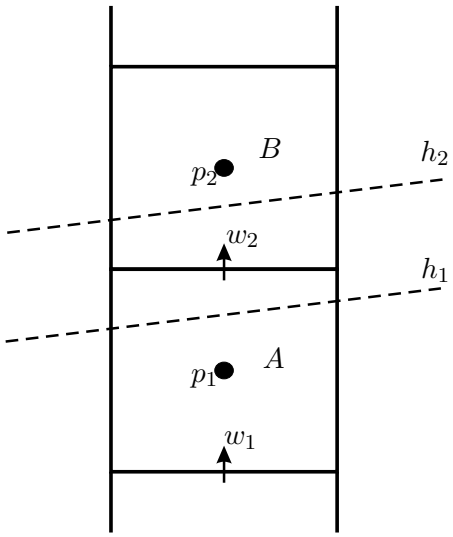

FIGURE 11.2: The splitting and merging of surface cells.

The two different types of surface pressure cell are referred to as *active* and *passive* respectively.

The reason for treating active and passive cells in different ways can shown when considering continuity. Consider in 2D, the flux into pressure cell p_c in figure 11.3, the kinematic free surface boundary condition (4.9) in finite difference form can be written as

$$\frac{\mathrm{d}F_c}{\Delta x \mathrm{d}t} = w_2 - u_b \left(\frac{l_c - l_a}{2\Delta x} \right) - u_d \left(\frac{l_e - l_c}{2\Delta x} \right). \tag{11.5}$$

where $-u(dh/dx)$ is approximated by a centre averaged value and the cell volume F_c has been substituted for h (11.1). The rate of change of volume is simply equal to the flux of fluid across the wet sides of the cell, thus

$$\frac{\partial F_c}{\partial t} = u_b l_b + w_1 \Delta x - u_d l_d. \tag{11.6}$$

By eliminating l_b and l_d, through insistence that the staggered and centred surface elevations are mutually consistent (11.3) and combining (11.5)& (11.6) we are left with

$$l_c(u_d - u_b) + \Delta x(w_2 - w_1) = 0, \tag{11.7}$$

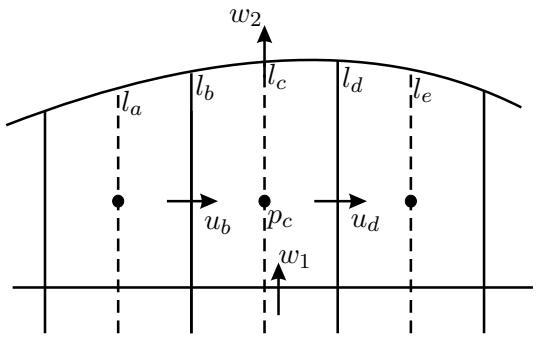

FIGURE 11.3: Conservation of mass in an active surface cell, – – – represents staggered cell control volume

for the continuity equation in an active surface cell, which is the same as for subsurface cells as l_c becomes Δz. However note that the equation does not hold for passive surface cells for which w_2 is absent.

11.1.1 Momentum terms for surface cells

When considering the momentum terms in (4.1) with respect to surface cells, we must consider the cases in which neighbouring cells have common borders, as shown in figure 11.4, but also neighbouring cells which have been split or merged leaving jumps in the surface cell geometry as shown in figure 11.5. We consider the 2D case to demonstrate the principles. The momentum flux across a surface separating two cells is approximated by the average of the velocity of each cell multiplied by the mass flux between the two cells. In the case of a surface cell without jumps (figure 11.4) the momentum equation as applied to a staggered cell (such as u_c) is then

$$\frac{\partial(l_c u_c)}{\partial t} = \frac{1}{2}(u_a + u_c)q_b + \frac{1}{2}(u_f + u_c)q_f - \frac{1}{2}(u_e + u_c)q_d, \tag{11.8}$$

where q denotes the mass flux. It is shown by Thomas *et al.* (1995) that this scheme conserves kinetic energy.

The more complicated case of a jump between surface cells is shown for u and w cells in figure 11.5. A jump occurs at a surface cell which has more than one neighbouring cell on one or more sides. The method used to ensure continuity of mass in such cases is, after enforcing continuity in the centred (Pressure) cells, to first calculate the horizontal mass fluxes and then calculate the vertical fluxes by explicitly enforcing continuity. Considering first the flux between u-cells (figure

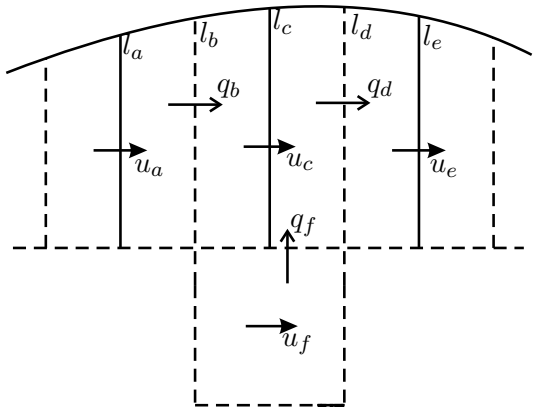

FIGURE 11.4: Momentum flux in a staggered cell (u_c).

11.5(a)), the fluxes q'_b and q''_b are found by calculating the average flux Q across the interface denoted by subscript b, using

$$2Q_b = l_a U_a + l'_c u'_c + l''_c u''_c \tag{11.9}$$

and then assuming constant flux we allot Q_b in portion to the lengths l'_b and l''_b which gives

$$q''_b = \frac{l''_b Q_b}{l''_b + l'_b}, \tag{11.10}$$

$$q'_b = \frac{l'_b Q_b}{l''_b + l'_b}. \tag{11.11}$$

Fluxes q'_d and q''_d are evaluated in the same way and q'_c is sufficiently far from the surface to be simply calculated by flux averaging w-velocities. To obtain the final vertical flux q''_c we then impose continuity, thus

$$q''_c = q'_c + q'_b - q'_d. \tag{11.12}$$

The horizontal fluxes between pairs of w-cells are shown in figure 11.5(b). By approximating u as constant across a w-cell interface and multiplying the velocity by the area of the interface yields

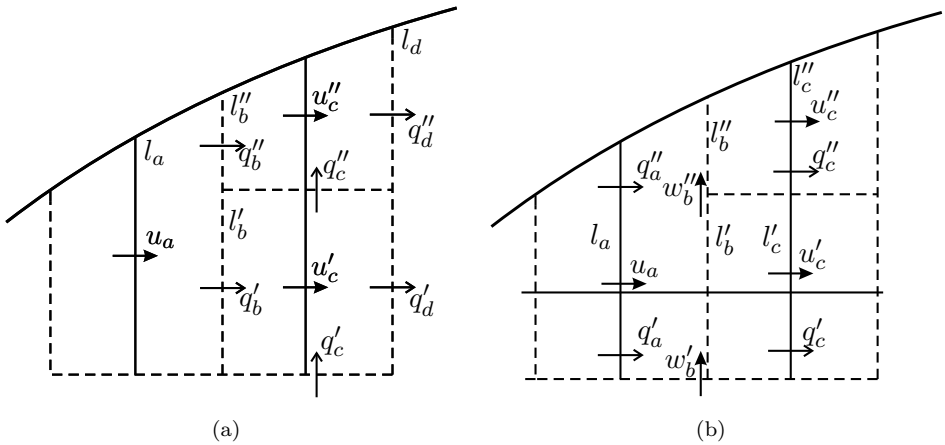

FIGURE 11.5: Flux interpolation at a jump between: (a) u-cells; (b) w-cells.

$$q''_a = (l_a - \frac{\Delta z}{2})u_a, \tag{11.13}$$

$$q''_c = u''_c l''_c + \frac{\Delta z}{2} u'_c. \tag{11.14}$$

11.1.2 Viscous terms for surface cells

We now consider the influence of the split-merge technique on the contribution of the viscous stress terms to (4.1). Considering again the 2D case, the viscous stresses corresponding to a surface cell with no surface jumps is shown in figure 11.6. Here τ_{xx} and τ_{xz} denote the viscous stress components on the axes and τ_{nn} and τ_{sn} denote the surface stress components, where the surface co-ordinates (s,n) are measured locally in the tangential and normal directions respectively. Applying (4.10) and (4.11) in 2D form gives the the unit normal vector $\mathbf{n}$ on the surface at c as

$$\mathbf{n} = (n_x, n_y) = S^{-1}(-(l_d - l_b), \Delta x), \tag{11.15}$$

$$S = \sqrt{(\Delta x^2 + (l_d - l_b)^2)}, \tag{11.16}$$

and the contribution of the viscous stresses to the u-cell momentum is found through summation of the stress contributions from each side, thus

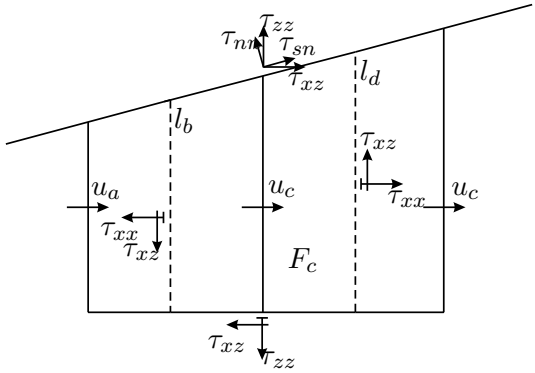

FIGURE 11.6: Viscous stresses in surface cell c.

$$F_c \frac{\mathrm{d}u_c}{\mathrm{d}t} = l_d(\tau_{xx})_d - l_b(\tau_{xx})_b - \Delta x(\tau_{xz})_c + (n_z S)(\tau_{sn}) + (n_x S)(\tau_{nn}) \tag{11.17}$$

where τ_{xx} and τ_{xz} are evaluated from the local velocity field. The surface boundary condition (4.12) requires that the tangential stress tends to zero at the surface removing the $\tau_{sn} = 0$ and τ_{nn} is evaluated from

$$(\tau_{nn})_{surface} = (n_x n_x \tau_{xx})_{surface} + (n_x n_z \tau_{xz})_{surface} + (n_z n_x \tau_{zx})_{surface} + (n_z n_z \tau_{zz})_{surface} \tag{11.18}$$

At a surface jump between cells (such as shown in figure 11.5(a)) the total stress at interface b is calculated from the stresses in the two adjoining split cells by

$$(l' + l'')\tau_{xx} = l'\tau'_x x + l''\tau''_x x, \tag{11.19}$$

where τ'_{xx} and $\tau''_x x$ are calculated from the local velocity field.

11.1.3 Pressure discretisation in surface cells

As mentioned previously, the presence of the free surface can create continuity cells without an upper bounding w cell, as demonstrated in figure 11.2. In such cases the cell pressure is assigned through linear interpolation, appealing to the surface pressure and the pressure cell below in the vertical direction only. In general the finite difference formulation equation (4.7) becomes

$$0 = \sum_{lmn} C_{i,j,k}^{lmn} p_{i+l,j+m,k+n} + s_{ijk} \quad \text{for } lmn \in \{-1, 0, +1\} \tag{11.20}$$

where s is the source term $(2/(3\Delta t)\partial u_i^*/\partial x_i)$, and $C_{i,j,k}^{lmn}$ represents the finite difference star coefficients for the ∇^2 operator. Although 27 coefficients are implied by $C_{i,j,k}^{lmn}$ only 15 are in fact non zero as interpolation is limited to the vertical direction. The assignment of $C_{i,j,k}^{lmn}$ is dependent upon the local surface configuration and the logic behind its structure can be found in Thomas *et al.* (1995).

11.2 Free surface advancement

Once the velocity field has been advanced to a new time step the surface height $h(x, y, t + \Delta t)$ must be updated. This is done by calculating the change in volume of a column of cells Δcol_{ij} as

$$\Delta\text{col}_{ij} = \Delta t.(\text{Flux into col}_{ij}). \tag{11.21}$$

The flux is based on the old elevation height h(t) and the new velocity u_i(x,y,z,t). The change in surface elevation follows from the surface locater rule (11.1)

$$h_{ij}(t + \Delta t) = h_{ij}(t) + \frac{1}{2\Delta x \Delta y}(\Delta\text{col}_{ij}(t) + \Delta\text{col}_{ij}(t + \Delta t)). \tag{11.22}$$

Since the flux into column col_{ij} is not known accurately at the new time step until column height is known equations (11.21) & (11.22) must be iterated a number of times.

Chapter 12

Appendix B

Reprint of Archer *et al.* (2008)

Bibliography

Archer, P., Thomas, T. & Coleman, G. 2008 Direct numerical simulation of vortex ring evolution from the laminar to the early turbulent regime. *Journal of Fluid Mechanics* **598**, 201–226.

Ashurst, W. & Meiron, D. 1987 Numerical study of vortex reconnection. *Physical Review Letters* **58**, 1632–1635.

Bayly, B. 1986 Three-dimensional instability of elliptical flow. *Physical Review Letters* **57**, 2160–2163.

Bergdorf, M., Koumoutsakos, P. & Leonard, A. 2007 Direct numerical simulation of vortex rings at $\mathrm{Re}_\gamma = 7500$. *Journal of Fluid Mechanics* **581**, 495–505.

Berry, M., Chambers, R., Large, M., Upstill, C. & Walmsley, J. 1980 Wavefront dislocations in the aharonov-bohm effect and its water wave analogue. *European Journal of Physics* **1**, 154–162.

Boyovintrev, V., Boyarintseva, T., Korotaev, D., Lednev, A. & Savin, A. 1997 Motion of vortex rings in media with homogeneous density along the normal to the surface. *Mekhanika Zhidkosi I Gaza* **32**, 125–129.

Cater, J., Soria, J. & Lim, T. 2004 The interaction of the piston vortex wit a piston-generated vortex ring. *Journal of Fluid Mechanics* **499**, 327–343.

Cerda, E. & Lund, F. 1993 Interaction of surface waves with vorticity in shallow water. *Physical Review Letters* **70**, 3896–3899.

Chu, C.-C., Wang, C.-T. & Hseih, C.-S. 1993 An experimental investigation of vortex motions near surfaces. *Physics of Fluids A* **5**, 662–676.

Coceal, O., Dobre, A., Thomas, T. & Belcher, S. 2007 Structure of turbulent flow over regular arrays of cubical roughness. *Journal of Fluid Mechanics* **589**, 375–409.

Coste, C. & Lund, F. 1999 Scattering of dislocated wave fronts by vertical vorticity and the aharonov-bohn effect. ii. dispersive waves. *Physical Review Letters E* **60**, 4917–4925.

Coste, C., Lund, F. & Umeki, M. 1999 Scattering of dislocated wave fronts by vertical vorticity and the aharonov-bohn effect. i. shallow water. *Physical Review Letters E* **60**, 4908–4916.

Crow, S. 1970 Stability theory for a pair of trailing vortices. *AAIA* **8**, 2172–2179.

Dabiri, J., Colin, S., Costello, J. & Gharib, M. 2005 Flow patterns generated by oblate medusan jellyfish: field measurements and laboratory analyses. *Journal of Experimental Biology* **208**, 1257–1265.

Dabiri, J. & Gharib, M. 2004 Fluid entrainment by isolated vortex rings. *Journal of Fluid Mechanics* **511**, 311–331.

Dazin, A., Dupont, P. & Stanislas, M. 2006*a* Experimental characterization of the instability of the vortex ring. part i: Linear phase. *Experiments in Fluids* **40**, 383 – 399.

Dazin, A., Dupont, P. & Stanislas, M. 2006*b* Experimental characterization of the instability of the vortex ring. part ii: Non-linear phase. *Experiments in Fluids* **41**, 401–413.

Dziedic, M. & Leutheusser, H. 1996 An experimental study of viscous vortex rings. *Experiments in Fluids* **21**, 315–324.

Fukumoto, Y. 2003 The three-dimensional instability of a strained vortex tube revisited. *Journal of Fluid Mechanics* **493**, 287–318.

Garten, J., Werne, J., Fritts, D. & Arendt, S. 2001 Direct numerical simulations of the crow instability and subsequent vortex reconnection in a stratified fluid. *Journal of Fluid Mechanics* **426**, 1–45.

Gharib, M. & Wiegand, A. 1996 Experimental study of vortex disconnection and connection at a free surface. *Journal of Fluid Mechanics* **321**, 59–86.

Glezer, A. & Coles, D. 1990 An experimental study of a turbulent vortex ring. *Journal of Fluid Mechanics* **211**, 243–283.

Gourlay, M., Arendt, S., Fritts, D. & Werne, J. 2001 Numerical modelling of initially turbulent wakes with net momentum. *Physics of Fluids* **13**, 3783–3802.

Hirsa, A. & Willmarth, W. 1994 Measurements of vortex pair interaction with a clean or contaminated free surface. *Journal of Fluid Mechanics* **259**, 25–45.

Kerswell, R. 2002 Elliptical instability. *Annu. Rev. Fluid Mech.* **34**, 83–113.

Krutzsch, C. 1939 Über eine experimentell beobachtete erscheining an werbelringen bei ehrer translatorischen beivegung in weklechin, flussigheiter. *Ann Phys.* **5**, 497–523.

Kumar, M., Arakeri, J. & Shankar, P. 1995 Translational velocity oscillations of piston generated vortex rings. *Physics of Fluids* **7**, 2751–2756.

Lamb, H. 1932 *Hydrodynamics*, 6th edn. Dover Publications.

Landman, M. & Saffman, P. 1987 The three-dimensional instability of strained vortices in a viscous fluid. *Physics of Fluids* **30**, 2339–2342.

Lighthill, J. 1978 *Waves in Fluid*, chap. Water waves, pp. 204–284. Cambridge University Press.

Lim, T. 1997 A note on the leapfrogging between two coaxial vortex rings at low reynolds numbers. *Physics of Fluids* **9**, 239–241.

Lim, T. & Nickels, T. 1992 Instability and reconnection in the head-on collision of two vortex rings. *Nature* **357**, 225–227.

Lloyd, A. & Hanson, P. 1985 Decay of trailing vortices. *Admiralty Research Establishment Paper* .

Longuet-Higgins, M. 1998 Vorticity and curvature at a free surface. *Journal of Fluid Mechanics* **356**, 149–153.

Lundgren, T. & Koumoutsakos, P. 1999 On the generation of vorticity at a free surface. *Journal of Fluid Mechanics* **382**, 351–366.

Maxworthy, T. 1972 The structure and stability of vortex rings. *Journal of Fluid Mechanics* **51**, 15–32.

Maxworthy, T. 1974 Turbulent vortex rings. *Journal of Fluid Mechanics* **64**, 227–239.

Maxworthy, T. 1977 Some experimental studies of vortex rings. *Journal of Fluid Mechanics* **81**, 465–495.

Naitoh, T., Fukuda, N., Gotoh, T., Yamada, H. & Nakajima, K. 2002 Experimental study of axial flow in a vortex ring. *Physics of Fluids* **14**, 143–149.

Nitsche, M. 2001 Self-similar shedding of vortex rings. *Journal of Fluid Mechanics* **435**, 397–407.

Ohring, S. & Lugt, H. 1996 Interaction of an obliquely rising vortex ring with a free surface in a viscous fluid. *Acta Mechanica Sinicia* **31**, 623–655.

Peck, B. & Sigurdson, L. 1994 The three-dimensional vortex structure of an impacting water drop. *Physics of Fluids* **6**, 564–576.

Peck, B. & Sigurdson, L. 1995 The vortex ring velocity resulting from an impacting water drop. *Experiments in Fluids* **18**, 351–357.

Pierrehumbert, R. 1986 Universal short-wave instability of two-dimensional eddies in an inviscid fluid. *Physical Review Letters* **57**, 2157–2159.

Press, W., Teukolsky, S., Vetterling, W. & Flannery, B. 2003 *Numerical recipes in Fortran 77*, chap. Partial differential equations, pp. 862–880. Cambridge University Press.

Rodriguez, F. & Mesler, R. 1988 The penetration of drop-formed vortex rings into pools of liquid. *Journal of colloid and interface science* **21**, 315–324.

Rusakov, Y. 2001 Dynamics of vertical motion of a turbulent vortex ring. *Izvestiya Atmospheric & Ocean Physics* **37**, 693–702.

Saffman, P. 1970 The velocity of viscous vortex rings. *Stud. Appl. Maths* **49**, 371–380.

Saffman, P. 1978 The number of waves on unstable vortex rings. *Journal of Fluid Mechanics* **84**, 625–639.

Sarpkaya, T. 1996 Vorticity, free surface, and surfactants. *Annual Review of Fluid Mechanics* **28**, 83–128.

Schneider, P. 1980 Sekundärwirbelbildung bei ringwirbeln und in freistrahlen. *Z. Flugwiss. Weltraumforsch* **4**, 307–318.

Shadden, S., Dabiri, J. & Marsden, J. 2006 Lagrangian analysis of fluid transport in empirical vortex ring flows. *Physics of Fluids* **18**, 047105.

Shariff, K., Leonard, A. & Ferziger, J. 2006 Dynamical systems analysis of fluid transport in time-periodic vortex ring flows. *Physics of Fluids* **18**, 047104.

Shariff, K., Verzicco, R. & Orlandi, P. 1994 A numerical study of three-dimensional vortex ring instabilities: viscous corrections and early nonlinear stage. *Journal of Fluid Mechanics* **279**, 351–375.

Smith, G., Volino, R., Handler, R. & Leighton, R. 2001 The thermal signature of a vortex pair impacting a free surface. *Journal of Fluid Mechanics* **444**, 49–78.

Song, M., Bernal, L. & Tryggvason, G. 1992 Head-on collision of a large vortex ring with a free surface. *Physics of Fluids A* **4**, 1457–1466.

Teixeira, M. & Belcher, S. 2002 On the distortion of turbulence by a progressive surface wave. *Journal of Fluid Mechanics* **458**, 229–267.

Thomas, T., Leslie, D. & Williams, J. 1995 Free surface simulations using a conservative 3d code. *Journal of Computational Physics* **116**, 52–68.

Thomas, T. & Williams, J. 1997 Development of a parallel code to simulate skewed flow over a bluff body. *Journal of Wind Enginnering and Industrial Aerodynamics* **67&68**, 155–167.

Thomas, T. & Williams, J. 1999 Simulation of skewed turbulent flow past a surface mounter cube. *Journal of Wind Enginnering and Industrial Aerodynamics* **81**, 347–360.

Umeki, M. & Lund, F. 1997 Spirals and dislocations in wave-vortex systems. *Fluid Dynamics Research* **21**, 201–210.

Vivanco, F. & Melo, F. 2004 Experimental study of surface waves scattering by a single vortex and a vortex dipole. *Physical Review Letters E* **69**, 06307.

Widnall, S. 1975 The structure and dynamics of vortex filaments. *Annu. Rev. Fluid Mech.* **7**, 141–165.

Widnall, S., Bliss, D. & Tsai, C.-Y. 1974 The instability of short waves on a vortex ring. *Journal of Fluid Mechanics* **66**, 35–47.

Widnall, S. & Sullivan, J. 1973 On the stability of vortex rings. *Proc. R. Soc. London. A* **332**, 335–353.

Widnall, S. & Tsai, C.-Y. 1977 The instability of the thin vortex ring of constant vorticity. *Phil. Trans. R. Soc. Lond.* **287**, 273–305.

Wiegand, A. 1996 Simultaneous mapping of the velocity and deformation field at a free surface. *Experiments in Fluids* **20**, 358–364.

Wiegand, A. & Gharib, M. 1994 On the decay of a turbulent vortex ring. *Physics of Fluids* **38**, 3806–3808.

Wiegand, A. & Gharib, M. 1995 Turbulent vortex ring/free surface interaction. *American Society of Mechanical Engineers* **117**, 374–381.

Willert, C. & Gharib, M. 1997 The interaction of spatially modulated vortex pairs with free surfaces. *Journal of Fluid Mechanics* **345**, 227–250.

Wu, C., Fu, Q. & Ma, H. 1995 Interactions of three-dimensional viscous axisymmetric vortex rings with a free surface. *Acta Mechanica Sinicia* **11**, 229–238.

Yao, Y., Thomas, T., Sandham, N. & Williams, J. 2001 Direct numerical simulation of turbulent flow over a rectangular trailing edge. *Theoretical and Computational Fluid Dynamics* **14**, 337–358.

Ye, Q. & Chu, C. 1997 The nonlinear interaction of vortex rings with a free surface. *Acta Mechanica Sinicia* **13**, 120–129.

Yoon, S. & Heister, S. 2004 Analytical formulas for the velocity field induced by an infinitely think vortex ring. *International Journal for Numerical Methods in Fluids* **44**, 665–672.

Zhang, C., Shen, L. & Yue, D. 1999 The mechanism of vortex connection at a free surface. *Journal of Fluid Mechanics* **384**, 207–241.